PHYSIK DEPARTMENT

Non-equilibrium Effects in Cytoskeletal Networks

Dissertation
von

Jona Kayser

TECHNISCHE UNIVERSITÄT MÜNCHEN

TECHNISCHE UNIVERSITÄT MÜNCHEN
Lehrstuhl für Zellbiophysik E27

Non-equilibrium Effects in Cytoskeletal Networks

Jona J. S. Kayser

Vollständiger Abdruck der von der Fakultät für Physik der Technischen Universität München zur Erlangung des akademischen Grades eines

Doktors der Naturwissenschaften (Dr. rer. nat.)

genehmigten Dissertation.

Vorsitzender: Univ.-Prof. Dr. M. Zacharias

Prüfer der Dissertation:
1. Univ.-Prof. Dr. A. Bausch
2. Univ.-Prof. Dr. M. Rief

Die Dissertation wurde am 14.11.2013 bei der Technischen Universität München eingereicht und durch die Fakultät für Physik am 09.12.2013 angenommen.

»Wir müssen versuchen unsere Grenzen in der
rechten Ordnung geduldig zu überwinden.
Einen Felsen zu durchfliegen, das ist noch zu früh,
das ist ein späterer Lehrstoff.«

Richard Bach - *Die Möwe Jonathan*

SUMMARY

The cells comprising living tissue constantly face a plethora of mechanical challenges. Not only do they have to support tissue integrity, they also have to exhibit an enormous degree of flexibility and the ability to undergo drastic morphological changes, for example, to enable cell locomotion. This broad bandwidth of demands is met by an equally astounding versatility of the cell's mechanical and morphological properties. These are based on the cytoskeleton, a complex network constituted from three different types of filamentous proteins: actin filaments, intermediate filaments and microtubules. Each component exhibits unique characteristics, yielding a highly involved composite system.

To unravel the intricacies of each individual system and to then combine these insights to better understand higher order networks and, eventually, the cytoskelton, *in vitro* model systems are an indispensable tool. Not only do they reduce the complexity to a level that allows for a detailed study of individual effects, they furthermore provide a well-controlled environment, essential for the investigation of the underlying physics. The present work introduces a novel model system of three dimensional networks of keratin 8/18 intermediate filaments. The incorporation of fluorescently labeled proteins furthermore facilitates the examination by confocal microscopy and other fluorescence based techniques. This, for the first time, provides the means to thoroughly investigate this major cytoskeletal component *in vitro* on a network level and under buffer conditions similar to those found in living cells.

In the first part of the thesis, the network's assembly dynamics are investigated. In contrast to other cytoskeletal components, keratin filaments exhibit an intrinsic ability to form bundles if assembled in the presence of physiological salt concentrations. This behavior results in a tendency to form clusters of bundles, rather than homogenous networks. Such clustering highlights the simultaneous progression of elongation and bundling during the assembly. With the help of time resolved transmission electron microscopy (TEM) the temporal hierarchy and high rapidity of keratin network assembly is revealed. Using this new insight, it is possible to develop a diffusion based assembly technique, yielding macroscopic homogenous networks of keratin bundles. The relation of the network's mesh size and the width of its comprising structures to the protein concentration suggests an impact of the assembly dynamics on the resulting network morphology. Indeed, close investigation of the early temporal evolution of the networks reveals kinetic trapping as the structure determining factor. Here, filament elongation and their lateral association to bundles are in competition. Bundling progresses until the network reaches a quasi-static, kinetically trapped state far from equilibrium where the percolating network architecture prevents any further motion, and therefore association, of bundles and filaments. How quickly this state is reached, and therefore the geometry of the network at the point of arrest, crucially depends on the balance between elongation and bundling. The hypothesis is confirmed by demonstrating that independently triggering filament elongation and bundling yields finer structures. Demonstrating that similar changes in network architecture can be achieved by altering the balance between filament elongation and bundling through variations in temperature or salt application underlines the generality of the observed effect.

While it is conceivable that the concept of kinetic trapping also plays a role in the cells organization of its keratin cytoskeleton, it is, however, much more likely that here the effect is triggered by associated proteins. We therefore assess the potential role of small heat shock proteins (sHsps) in this context. These molecular chaperons are primarily known for assisting protein folding and thereby preventing deleterious protein aggregation. However, one member of this family, the 27 kDa heat shock protein Hsp27, has also been reported to colocalize with keratin structures *in vivo*. Here, we show that the presence of Hsp27 during keratin network assembly *in vitro* results in much finer, more homogeneous networks. The strength of the effect depends on the Hsp27 concentration and is highly reminiscent of the kinetic trapping scenario described before. Directly examining the influence of Hsp27 on the network formation process confirms kinetic trapping to be at the heart of the effect. While in the absence of Hsp27 networks undergo a characteristic coarsening process in the later stages of the assembly, its presence leads to an earlier onset of kinetic trapping and the inhibition of continued coarsening. Electron microscopy reveals a close association of Hsp27 oligomers and keratin structures, leading to decreased bundling. Analytical ultracentrifugation furthermore confirms keratin-Hsp27 interaction in a pre-assembly state. Employing a series of mutants, the active site of the effect can furthermore be traced to the proximal region of keratin 8's C-terminal tail domain.

The importance of kinetic trapping during network assembly and the ensuing non-equilibrium nature is not unique to keratin. Similar mechanisms have been demonstrated for bundled actin networks. We therefore investigate the role of kinetic trapping in composite keratin/actin bundle networks. Here, the separation of the assembly time scales of both systems is of great avail, preventing complex interdependencies of the formation processes. While keratin networks form in the matter of seconds, actin bundle networks require several minutes to build up. Therefore, keratin can serve as a pre-formed scaffold for the emerging actin bundle network. In this work, we first investigated the impact of a keratin scaffold on actin/α-actinin bundle networks, which have been demonstrated to exhibit kinetic trapping during their formation. We show that changing the mesh size of the keratin scaffold by a variation of keratin concentration invokes a similar change in the mesh size of the actin network, even though the biochemical composition of the actin system is kept unchanged. This behavior can be rationalized in the kinetic trapping framework, where actin bundle formation is hampered by the presence of the keratin scaffold. In a second step, the same experiments are conducted with actin/fascin bundle networks. These bundles normally exhibit an intrinsically limited bundle size and therefore should be less susceptible to the effects of kinetic trapping. It therefore is surprising to observe an impact of the keratin scaffold on this system, similar to that demonstrated for actin/α-actinin bundles.

Having established keratin and keratin/actin composite networks as model systems, the following part of this thesis presents initial investigations of their response to mechanical load. To this end, a shear chamber is developed, enabling the direct imaging of network deformations induced by a shear strain. The setup features a novel diffusion chamber concept, allowing for the assembly of percolating networks. The networks are sheared in a step-wise manner and confocal z-stacks are recorded between steps. Local network displacement can then be acquired via digital image processing. While the general response of the networks suggests complex, nonlinear behavior on the scale of the entire sample, especially in the case of the composite system, the region accessible to microscopy displays perfectly linear behavior in both cases. These first results, though not yet providing conclusive evidence for emergent behavior in composite networks, proves the feasibility of the experimental approach and serve as a control for future investigations in this direction.

The last part of this thesis focuses on the impact of non-equilibrium aspects on network dynamics on long time scales. Reconstituted cytoskeletal net-

works do not only serve as a model system for the cytoskeleton, but also to understand the interplay between microscopic structure and macroscopic viscoelastic properties of network-forming soft materials, in general. These constitute a broad class of materials with countless applications in science and industry. Here, we show that fully polymerized actin/fascin bundle networks display surprising age-dependent changes in their viscoelastic properties and spontaneous dynamics, a feature strongly reminiscent of out-of-equilibrium, or glassy, soft materials. Using a combination of rheology, confocal microscopy and space-resolved dynamic light scattering, we demonstrate that actin networks build up stress during their formation and then slowly relax towards equilibrium due to the unbinding dynamics of the crosslinking molecules.

The present work provides novel insight into the non-equilibrium characteristics of cytoskeletal networks. Especially the introduced model system of reconstituted keratin intermediate filament networks represents an important step towards a more comprehensive understanding of the cytoskeleton as a complex composite material. In addition, the discussed concepts, systems and experimental techniques may be relevant in a more general material science context, providing new perspectives for future investigations.

CONTENTS

1 INTRODUCTION 1
2 MATERIALS AND METHODS 7
  2.1 Keratin Networks 7
    2.1.1 Recombinant Proteins 7
    2.1.2 Tail Truncation Mutants 7
    2.1.3 Fluorescent Labeling 8
    2.1.4 Network Assembly 8
    2.1.5 Electron Microscopy 10
    2.1.6 Fluorescence Microscopy 10
    2.1.7 Analytical Ultracentrifugation 10
    2.1.8 FRET 11
  2.2 Composite Networks 11
    2.2.1 Network Assembly 11
    2.2.2 Shear Chamber 11
  2.3 Slow Relaxation Dynamics 12
    2.3.1 Sample Preparation 12
    2.3.2 Rheology 13
    2.3.3 Dynamic Light Scattering and Displacement Maps 13
  2.4 Digital Image Analysis 14
    2.4.1 Determining the Characteristic Mesh Size 14
    2.4.2 Fast Fourier Transform Analysis 17
  2.5 Tracking of sheared networks 18
3 INTRODUCTION TO KERATIN INTERMEDIATE FILAMENTS 21
  3.1 Filament Structure and Assembly 22
  3.2 *In Vitro* Investigations 24
4 ASSEMBLY KINETICS DETERMINE STRUCTURE OF KERATIN NETWORKS 27
  4.1 Bundling and Clustering of Keratin Filaments *in vitro* 27
  4.2 Reconstituted Keratin Intermediate Filament Networks 29
  4.3 Interplay of Network Assembly Dynamics and Structure 31
  4.4 Conclusion 35
5 HSP27 AFFECTS THE ASSEMBLY DYNAMICS AND STRUCTURE OF KERATIN NETWORKS 37
  5.1 Small Heat Shock Proteins and Intermediate Filaments 37
  5.2 Influence of Hsp27 on Keratin Network Morphology 38
  5.3 Hsp27-induced Inhibition of Coarsening Dynamics 39

   - 5.4 Significance of the Keratin 8 Tail Domain 43
   - 5.5 Hsp27 and Kinetic Trapping 46
   - 5.6 Conclusion 47
- 6 COMPOSITE NETWORKS OF KERATIN AND ACTIN 49
   - 6.1 First Steps Towards a Composite System 49
   - 6.2 Impact of a Keratin Scaffold on Actin Bundle Networks 50
   - 6.3 Composite Networks Under Shear 54
   - 6.4 Conclusion 59
- 7 SLOW RELAXATION DYNAMICS 61
   - 7.1 Actin Networks as a Model System for Soft Glassy Materials 61
   - 7.2 Evolution of Mechanical Properties on Long Time Scales 62
   - 7.3 Internal Stress Relaxation 65
   - 7.4 Analysis of Microscopic Relaxation Dynamics via Dynamic Light Scattering 70
   - 7.5 Alteration of Internal Stress by Fascin Mutants 72
   - 7.6 Conclusion 73
- 8 OUTLOOK 75
- BIBLIOGRAPHY 90
- LIST OF FIGURES 92
- LIST OF PUBLICATIONS 93
- ACKNOWLEDGEMENTS 95

1

INTRODUCTION

Cells are the fundamental building block of life. Complex organisms, such as humans, comprise a plethora of different cell types, each tasked with specific functions. Only their astounding versatility and adaptability enables cells to overcome the challenges they are continuously facing. This holds especially true for their mechanical and structural properties which are essential for many critical biological processes, ranging from cell differentiation during embryogenesis to the metastatic behavior of tumor cells. Cells can change their shape, crawl and adapt to the attributes of their surrounding while also providing the tissue they are constituting with the necessary structural integrity. These mechanical properties are to a great extent attributed to the cytoskeleton, a complex composite network of protein fibers (Fig. 1.1). It's main constituents can be divided into three major families: actin filaments, intermediate filaments and microtubules. Each subsystem has unique qualities and is associated with a different range of functions. Actin filaments are, for example, essential for cell locomotion while also playing a major part in cytokinesis. Intermediate filaments, on the other hand, provide the cell with structural integrity and microtubules are responsible for chromosome arrangement and separation during cell division. However, it is the intricate interplay of all subsystems that results in the complex characteristics of the cytoskeleton as a whole.

To elucidate the processes governing this highly convoluted composite material a thorough understanding of the integral components is indispensable. However, the complexity of the cell impedes investigation of the underlying physical principles. Recent years have seen increasing success of cytoskeletal model systems of reconstituted networks to circumvent the convolution of a living cell. Especially for actin, this bottom-up approach yielded valuable insight of how single filament properties propagate to the mechanical behavior of the macroscopic system and how these can be altered by associated proteins via cross-linking, bundling and changing polymerization dynamics(1–4). Furthermore, much progress has been made in understanding the physics behind active cytoskeletal systems, where molecular motors interact with filaments, converting chemical to mechani-

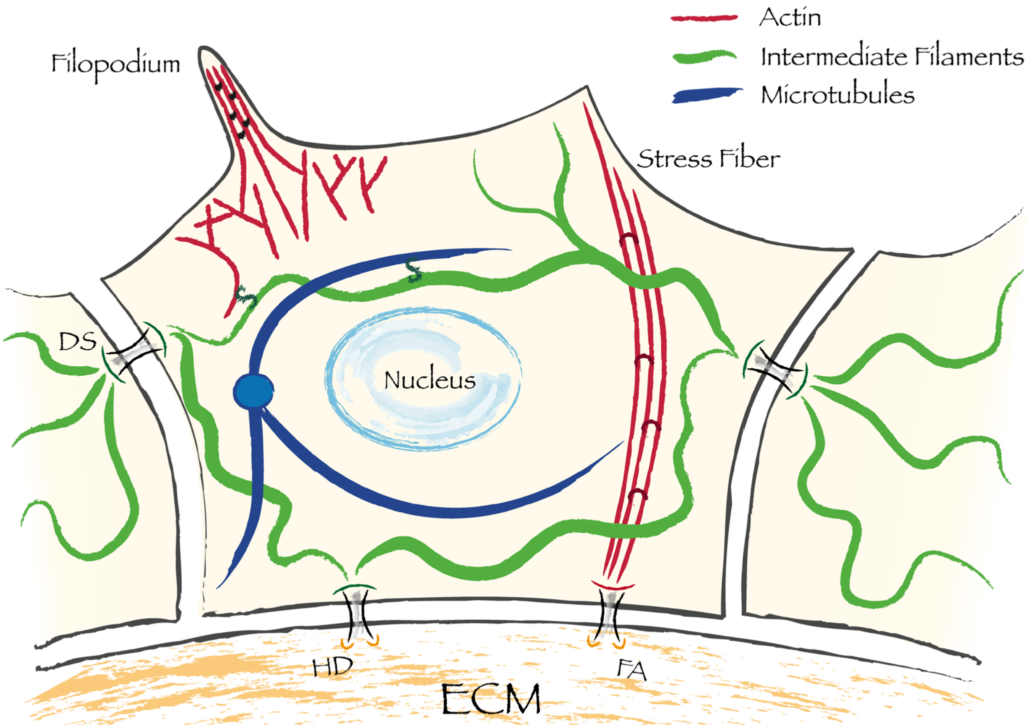

Figure 1.1: Cartoon of the cytoskeleton. The cytoskeleton is an intertwined composite network of three distinct classes of biopolymers: actin filaments (red), intermediate filaments (green) and microtubules (blue). Each subsystem exhibits characteristic features, comprising the complex properties of the constituted meshwork. Specific associated proteins and protein complexes can organize filaments into a wide array of different architectures, for example filopodial protrusions and stress fibres (actin) or the mitotic spindle (microtubules). Additionally, certain crosslinking proteins have the ability to interconnect different filament systems with each other. Membrane protein complexes - such as focal adheasions (FA), desmosomes (DS) and hemidesmosomes (HD) - link the cytoskeleton to neighboring cells or the extracellular matrix (ECM), providing the tissue with structural integrity.

cal energy(5–7). Maybe even more surprising is that extensive insight into phenomena of collective motion could be gained by analyzing the polar patterns of actin filaments driven by molecular motors(8, 9).

For intermediate filaments, *in vitro* investigations have been in most parts limited to the single filament level, collapsed networks and gels at salt concentrations far from physiological values(10–13). Especially the structural evaluation of three-dimensional networks by fluorescence microscopy has been hampered by the lacking availability of adequate model systems. This is partly due to severe experimental challenges associated with these highly insoluble proteins. Yet, mastering these difficulties promises a completely new cytoskeletal model system, orthogonal to its established actin and microtubule counterparts. This does not only promise new insight into the inner workings of the intermediate filament component but will help to identify features that have a more general relevance for the entire cytoskeleton. It has, for example, for a long time been generally presumed that actin and intermediate filaments assemble into thermally equilibrated networks. This is partially due to the fact that it is the simplest of all possible scenarios. Recent studies have shown, however, that this assumption does not necessarily hold true for bundled actin networks which can get trapped in a state far from equilibrium during network assembly(14, 15). Now, a thorough investigation of intermediate network assembly processes has to assess whether such non-equilibrium effects are a more general feature of cytoskeletal systems. As a further step, it will be necessary to increase the complexity of cytoskeletal model systems to a multi-component network in order to investigate the interplay of different components on network behavior in this context.

The main goals of this thesis are as follows:

- The first step is to **establish a well controlled model system** for intermediate filaments. This will include a robust protocol for the expression and purification of keratin 8 and 18 intermediate filament proteins, including the necessary procedures and quality controls. Furthermore, labeling proteins with a fluorescent dye will be essential to enable the structural investigation of keratin networks via fluorescence microscopy (chapter 2). Using the acquired proteins, different methods of assembly will be explored to yield homogeneous, reproducible networks accessible by fluorescence microscopy.

- Once this is accomplished, a thorough **characterization of the system** will follow. This will include the installation of necessary experimental procedures and the initial investigation of primary parameters, such as buffer composition, protein concentration and temperature in order to identify a suitable parameter space for following experiments. Physiological values, as they are found *in vivo*, will serve as a guide. Here, conditions similar to those routinely used for actin assembly, will be of special interest as they facilitate the direct comparison of both systems and the introduction of keratin/actin composite systems later in this project.

- Subsequently, a qualitative and quantitative study of the network's **structure**, it's **formation dynamics** and the interplay between both will follow (chapter 4). To this end, the design of tailored experimental setups as well as the programming and implementation of suitable image analysis software will be required. The acquired data will be evaluated and interpreted to unravel the underlying physics and assess the importance of non-equilibrium effects for the assembly of keratin networks.

- The chemical and physical phase space accessible to living cells is limited to a narrow region. Hence, employing regulatory proteins is the cells primary mean of controlling the cytoskeletal architecture. Therefore, the potential of keratin associated proteins to influence the network's assembly dynamics and structure will be investigated (chapter 5). Here, the focus will be on the **impact of small heat shock proteins** (sHsps), as they have been reported to colocalize with keratin structures *in vivo*. Additionally, details of keratin-sHsp interaction will be explored.

- A further step of this project will be to construct a two component **composite system**, comprised of keratin and actin bundle networks (chapter 6). Not only does the increased complexity of such a system emulate the inherently complex nature of the cytoskeleton but also promises further insight into the intricate interplay between both subsystems. The impact of such interdependencies on network formation processes are of special interest. Moreover, the possibility of probing these systems via confocal microscopy while simultaneously applying a mechanical load will be explored.

- In addition to the role of non-equilibrium effects in the structural evolution of forming networks, their impact on the system's mechanical properties on very long time scales is of great interest, especially in the context of soft glassy materials. We will investigate the impact of **slow relaxation dynamics** in actin/fascin bundle networks on the age-dependend changes of the network's rheological properties (chapter 7). This model system allows excellent accessibility via a broad range

> of experimental techniques, such as macrorheology, fluorescence microscopy and space-resolved dynamic light scattering, not feasible for the investigation of conventional network-forming soft materials.

While the results presented in this work provide new insight into the inner workings of cytoskeletal networks, especially considering keratin and keratin/actin composite system, they are only a first step towards a more comprehensive understanding of these complex material. At the end of this thesis, an outlook will be given on future projects that will continue to extend our knowledge on the cytoskeleton and related materials (chapter 8).

2

MATERIALS AND METHODS

The networks investigated in this work are assembled from reconstituted proteins. This chapter aims to give description of the material and methods used in this process. All experimental setups and procedures are explained in detail. As digital image analysis has greatly contributed to the evaluation of the recorded data, a comprehensive account of the applied procedures is given at the end of this chapter.

2.1 KERATIN NETWORKS

2.1.1 *Recombinant Proteins*

Recombinant human keratins K8 and K18 were expressed, purified and prepared as described (16). In short, proteins where expressed in *E. coli*, purified and stored in 8M urea. Before use, basic and acidic keratins where mixed in an equimolar ratio and refolded by a stepwise dialysis to 6M, 4M and 2M urea in low-tris-buffer (2mM Tris, pH 9.0, 1mM DTT). Dialysis was continued over night into urea free buffer. Hsp27 was purified as described elsewhere and dialyzed against the same low-tris-buffer to prevent any buffer related artifacts (17). Hsp27 activity at these conditions was confirmed by investigating the suppression of the thermal aggregation of citrate synthase (CS) as model substrate where Hsp27 showed a half maximal suppression at a ratio of 1:1 (CS:Hsp27), identical to reported values (18).

2.1.2 *Tail Truncation Mutants*

Mutant keratins with partial or complete truncation of the C-terminal tail domain were produced by modifying the nucleotide sequence to a stop codon at the desired position. For this, a QuikChange Lightning Site-Directed Mutagenesis Kit (Agilent Technologies, Santa Clara, USA) was used, following the manufacturers instructions. The keratin 8 tail was assumed to begin after residue 402 and that of keratin 18 after residue 388 (residue numbering inclusive of the starting methionine) (19). Additional mutants for keratin 8 were truncated after residues 426 and 466.

2.1.3 *Fluorescent Labeling*

The wild type amino acid sequence of keratin 8 does not contain any cysteines. This allows for site specific attachment of a fluorescent marker via an introduced cysteine. For this purpose we performed a point mutation in keratin 8, changing the native serine 243 (located in the non-helical L1-2 linker segment) to a cysteine using a QuikChange site directed mutagenesis kit (Agilent Technologies, Santa Clara, USA). Additionaly, serine 478 in the carboxy-terminal tail domain of keratin 8 was chosen as an alternative site of mutation (Chapter 4 and FRET measurements). The site of the mutation was chosen such that interference of the label with protein folding is minimized. Subsequently, a fluorescent dye (ATTO647N or ATTO488; ATTO-TEC GmbH, Siegen, Germany; 5-TAMRA; life technologies, Carlsbad, USA) was covalently bound to the introduced cysteine following the manufactures instructions. Proper filament assembly was verified via electron microscopy. The total percentage of labeled keratin was 10% for all experiments involving fluorescent proteins (except FRET assays). Hsp27 was labeled with 5-Carboxyfluorescein succinimidyl ester (5-FAM) or 5-Carboxytetramethylrhodamine succinimidyl ester (5-TAMRA; life technologies, Carlsbad, USA) according to the manufacturer's protocol for 2 h at room temperature in PBS. Unbound label molecules were removed using a HiPrep 26/10 Desalting Column (GE-Healthcare, Little Chalfont, UK).

2.1.4 *Network Assembly*

Network assembly was initiated by the addition of 10 times concentrated assembly buffer (20mM Tris, pH 7.5, 10mM $MgCl_2$, 2mM $CaCl_2$, 2mM DTT, 5mM ATP, 1M KCl) to 9 parts of protein solution, resulting in a sample of pH 7.8 at 37°C (chapter 4). In chapter 5, the Tris concentration was increased to 200mM, resulting in a final pH of 7.3. No effect of pH on the network structure was observed between pH 7.3 and 8.0. For the formation of networks, the speed of formation at higher protein concentrations ($c_K >$ 1 µM = 0.5 g/l) prohibits the application of conventional mixing techniques with a pipette. Networks will already form in the pipette tip followed by destruction caused by subsequent pipetting. These difficulties can be circumvented by a "droplet-fusion" technique where a small droplet (4.5 µl) of protein solution is applied to a cover slip (Fig. 4.3c). A second 0.5 µl droplet of concentrated assembly buffer is applied to a second cover slip.

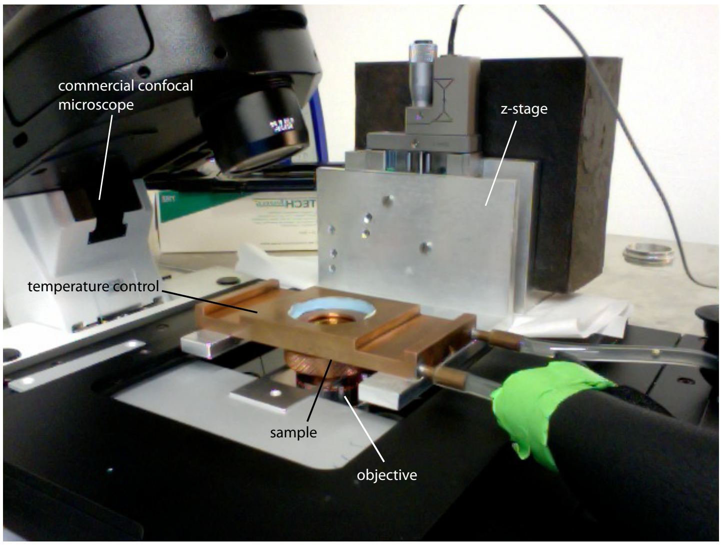

Figure 2.1: Temperature control setup for real time measurements of network assembly. The composite image shows a photo of the setup overlaid with a schematic detailing the setup's interior. The top cover slip, where the protein solution rests prior to assembly, is fixed on a temperature controlled metal block supported by movable *z*-stage. This stage can be lowered by a micrometer screw to initiate droplet fusion. The entire setup can be placed on a confocal microscope for imaging.

Both droplets are then carefully merged by bringing the two cover slips in close proximity, resulting in a disc shaped sample of 5 µl volume with an approximate diameter of 2 mm and a hight of $\sim$ 1.6 mm (Fig. 4.3d). The small size of the sample ensures fast dispersion of ions and a minimum of shear flow. A short initial salt concentration gradient is inherent to this technique. Therefore the side of the sample that initiates contact with the assembly buffer is exposed to a short peak in salt concentration and is therefore termed "high salt" side. The concentration at the adjacent side of the sample, the "low salt" side, increases gradually. However, the networks on the respective sides of the samples are homogeneous on the length scales investigated in this work and can therefore be regarded as two separate samples with different assembly pathways. All solutions were incubated at 37°C before assembly unless otherwise specified. The temperature of the cover slips was held constant at the same value throughout the assembly process. In chapter 5, Hsp27 and keratin were mixed before incubation at $T = 37°\text{C}$ for approximately 10 minutes. For the real time assessment of keratin assembly, a custom made setup was designed to ensure the precise temperature control of the sample before and during assembly (Fig. 2.1). The ATP present in the buffer purely serves to maintain conditions that are compatible with actin polymerization and does not influence Hsp27 activity (20, 21).

2.1.5 *Electron Microscopy*

Electron microscopy was carried out on a Phillips CM100 transmission electron microscope (Philips/FEI Corporation, Eindhoven, The Netherlands). For electron microscopy assays in chapter 4, assembly was initiated by the addition of 2x assembly buffer to the same volume of protein solution. Where necessary, assembly is terminated after the indicated time t by the addition of an equal volume of stop buffer (0.4% glutaraldehyde freshly prepared in a buffer identical to that of the sample). Samples where applied to a glow discharged carbon-coated copper grid (Electron Microscopy Sciences, Hatfield, PA, USA). In chapter 5 assembly was conducted similar to samples for fluorescence imaging directly on the carbon-coated copper grid. Buffer salt concentrations were adjusted as described in the main text. Samples where then negatively stained for visualization. The final protein concentration was 1-2 µM for all samples.

2.1.6 *Fluorescence Microscopy*

Confocal fluorescence microscopy was conducted on a Leica SP5 confocal microscope (Leica Microsystems, Wetzlar, Germany). All images are confocal slices taken at the sample side of assembly buffer introduction at comparable distances from the surface (160-230 µm). The network structure was verified to be homogeneous within the network volume accessible by the 63x glycerol immersion objective used in this study. Stimulated emission depletion (STED) fluorescence microscopy was employed for subdiffraction resolution imaging. STED-images where taken on a custom build in-house setup with a supercontinuum laser source as described(22). The setup was optimized for the use of ATTO647N dyes.

2.1.7 *Analytical Ultracentrifugation*

To determine the sedimentation coefficient of keratin and keratin-Hsp27 complexes by sedimentation velocity experiments, we used an Optima XL-A centrifuge equipped with absorbance and interference optics (Beckman Coulter, Krefeld, Germany). All samples contained 0.77 µM of ATTO-647N labeled keratin wild type and 77 µM of Hsp27 in 2 mM Tris pH 9.0, 1 mM DTT buffer. 420 µL of each sample were filled in sapphire-capped double sector centerpieces with a path length of 12 mm and analyzed at 42,000 rpm in an eight-hole Ti-50 Beckman-Coulter rotor. Detection was performed with interference optic and absorbance optic at 647 nm to distinguish between keratin and the total protein amount. Absorbance scans were taken in the continuous scanning mode with a radial resolution of 0.003 cm and one replicate per scan. Data analysis was conducted with Sedfit (23), using a non-model based continuous Svedberg distribution method ($c(s)$), with time (TI) and radial (RI) invariant noise enabled. Solvent density and viscosity were calculated with SEDNTERP (24).

2.1.8 *FRET*

Interaction between Hsp27 and K8/18 was monitored by fluorescence resonance energy transfer (FRET) as described elsewhere (18, 25). Keratin 8 was labeled with ATTO488 at the end of the tail region and Hsp27 was labeled with 5-TAMRA, as described above. FRET was measured by adding rising amounts of Hsp27-TAMRA to a constant concentration of 280 nm Keratin-ATTO488. For equilibration, the mixtures were incubated at $T = 37°\mathrm{C}$ for 5 min (until the emission intensity stabilized) prior to spectra accumulation, using a SPEX Fluoromax-3 fluorescence spectrometer (Jobin Yvon, Munich, Germany). The Excitation wavelength was 480 nm and spectra were recorded from 500 to 650 nm. To eliminate cross-excitation contributions, emission intensities where corrected by subtracting the intensities recorded from an acceptor-only sample. Observed FRET-independent quenching of the donor was corrected with reference to a donor-only sample.

2.2 COMPOSITE NETWORKS

2.2.1 *Network Assembly*

Initial composite networks where created by droplet fusion, similar to pure keratin networks. All proteins where mixed prior to assembly at room temperature. Actin and fascin where prepared as described in section 2.3.1. For confocal imaging, actin was labelled with ATTO 488 phalloidin (life technologies, Carlsbad, USA). α-actinin was expressed in *E. coli* and purified as described(26). The low amount of salt in the actin G-buffer did not initiate keratin assembly. Imaging and mesh size analysis were conducted as described for pure keratin networks.

2.2.2 *Shear Chamber*

For the investigation of networks under mechanical load, a shearable diffusion chamber was developed (see also section 6.3 and Fig. 6.4). For each experiment, the membrane is cut anew to the required proportions from a fresh cellulose filter membrane of 47 mm diameter and with a pore size of 0.1 µm (Millipore, Billerica, USA). All pre-assembly steps are carried out analogous to the droplet fusion. The protein droplet is placed on the lower cover slip and assembly buffer of $\sim$ 1x concentration (corrected for dilution by the sample) is filled into the reservoir, saturating the membrane. Additional drops of water are placed around the solvent trap which is then covered with an additional cover slip. If the covering of the solvent trap is omitted, the ensuing evaporation can induce flow into the reservoir which in turn couples to the sample, inhibiting proper network formation. The part of the z-stage containing reservoir and membrane can be easily disconnected from the structure for preparation. It has been demonstrated to be advantageous to place the z-stage at a predetermined position without the reservoir and then click the later into its position to initiate assembly. Since shear-experiments take several hours, special care has to be taken to prevent sample evaporation by placing a ring of vacuum grease around the protein droplet. After proper network assembly, the sample can be sheared by manipulating the computer controlled actuator (Physik Instrumente (PI), Karlsruhe, Germany) using the PIMikroMove software. For automated recording, timing of the confocal software and the actuator has to be coordinated. Here, 2 min cycles have been used for all experiments. The obtained data can then be evaluated by digital image analysis (see section 2.4).

2.3 SLOW RELAXATION DYNAMICS

2.3.1 *Sample Preparation*

G-actin is obtained from rabbit skeletal muscle and stored in lyophilized form at $-20°$C(27). For measurements, the lyophilized actin is dissolved in deionized water and dialyzed against G-buffer (2 mM Tris, 0.2 mM ATP, 0.2 mM $CaCl_2$, 0.2 mM DTT, and 0.005% NaN_3, pH 8) at 4°C. The G-actin solutions are kept at 4°C and used within seven days of preparation. Polymerization is initiated by adding 10 % volume 10x F-buffer (20 mM Tris, 5 mM ATP, 20 mM $MgCl_2$, 2 mM $CaCl_2$, 1 M KCl, 2 mM DTT, pH 7.5). The average length of the actin filaments is controlled to 21 µm using gelsolin obtained from bovine plasma serum(28). Recombinant human fascin (55 kD) is prepared by expression in *E. coli*(29, 30). Fascin-S39A mutants are created as outlined in(29). For confocal microscopy (TCS SP5 confocal microscope; Leica, Wetzlar, Germany), filaments are labeled with 3 µM TRITC-phalloidin. The sample age was defined as $t_w = 0$ for a fully polymerized network, i.e. typically 60 min after polymerization was initiated.

2.3.2 *Rheology*

The viscoelastic response of actin/fascin networks is determined by measuring the frequency-dependent viscoelastic moduli $G'(f)$ and $G''(f)$ with a stress-controlled rheometer (Physica MCR 301; Anton Paar, Graz, Austria) over a frequency range of three decades. Approximately 500 µl sample volume is loaded within 1 min into the rheometer. Measurements are conducted at 21°C using a 50-mm plate-plate geometry with 160-µm plate separation. To ensure linear response, small torques (≈ 0.5 µNm) are applied. Actin polymerization is carried out *in situ*. A solvent trap is placed around the sample to prevent drying artifacts. As a control, the application of a thin oil film (DMS-T05 polydimethylsiloxane; ABCR, Karlsruhe, Germany) to the liquid-air interface is employed as an alternative measure to prevent sample evaporation. Both solvent trap and oil film efficiently avert sample drying and result in similar experimental outcomes. For crosslinker fixation experiments, F-buffer containing 0.1 % (v/v) glutaraldehyde is carefully applied to the liquid-air interface after completion of polymerization.

2.3.3 *Dynamic Light Scattering and Displacement Maps*

Actin networks are polymerized *in situ* in a Hellma optics quartz cell with an inner diameter of 8 mm, sealed with parafilm. Experiments are performed at room temperature. Data shown in Fig. 7.6c are obtained using four CCDs to simultaneously detect light scattered at $\theta = 22.5°, 45°, 90°$ and $120°$, corresponding to $q = 6.1, 12.0, 22.2$ and $27.2\ \mu\text{m}^{-1}$, with $q = 4\pi n\lambda^{-1}\sin(\theta/2)$ the scattering wave vector, $n = 1.33$ the solvent refractive index and $\lambda = 0.532\ \mu$m the in-vacuo wavelength of the incident laser beam. The laser beam is mildly focussed to a $1/e^2$ diameter ~ 0.06 mm and the CCDs are close to far field conditions. All other DLS data and the displacement maps are obtained using the Photon Correlation Imaging geometry described in Ref.(31). In brief, light scattered in a small angular interval $\Delta\theta \sim 5°$ centered around a well defined angle θ is used to form an image of the sample onto a CCD detector, with a low magnification $M \sim 3$. We here report data for $\theta = 45°$, which we have checked to be consistent with those collected at $\theta = 22.5°, 90°$ and $120°$. The laser beam is collimated to a $1/e^2$ diameter ~ 0.8 mm. The images have a speckled appearance, as shown in Fig. 7.3a. We acquire time series of images at a rate of 0.5 Hz for up to 1 day and process them in order to measure mesoscopic displacement maps (in the imaging configuration) and the microscopic dynamics (for both imaging and far field configurations). Displacement maps are obtained by applying a custom Image Correlation Velocimetry algorithm(32), which is run on squares of 40 pixel side length (169 µm in the sample). The algorithm uses standard space correlation methods to measure the displacement of each square between times t_{w} and $t_{\mathrm{w}} + \tau$. The average displacement is defined as $< \delta >= N^{-1} \sum_{i=1}^{N} \sqrt{\delta_{x,i}^2 + \delta_{y,i}^2}$, with $\delta_{x,i}$, $\delta_{y,i}$ the x and$y$ components of the displacement of the i-th square and N the number of squares. Since space correlation functions are averaged over the square size, i.e. over as many as 1600 pixels, displacements can be accurately measured down to subpixel resolution. By analyzing images where the sample is displaced in a controlled manner using a stepper motor, we estimate the typical accuracy to be about $1/50$ of the pixel size, corresponding to ~ 0.08 µm. The microscopic dynamics is quantified by a two-time intensity correlation function:

$$g_2(t_{\mathrm{w}}, \tau, q) - 1 = \left\langle \frac{< I_p(t_{\mathrm{w}} + \tau) I_p(t_{\mathrm{w}}) >_p}{< I_p(t_{\mathrm{w}} + \tau) >_p < I_p(t_{\mathrm{w}}) >_p} - 1 \right\rangle_{t_{\mathrm{w}}}, \qquad (1)$$

where $I_p(t)$ is the intensity measured at time t by the $p-$th pixel, $< \cdots >_p$ is an average over all pixels associated to the CCD placed at a scattering vector q, and $< \cdots >_{t_{\mathrm{w}}}$ is an average over a 400 seconds time interval beginning at t_{w}. Local displacements in the sample are corrected by applying a similar procedure as for the acquisition of displacement maps (see above). With the normalization of Eq. (1), $g_2(t_{\mathrm{w}}, \tau) - 1$ decays from ≈ 1 to ≈ 0 as filaments move with respect to each other over a distance on the order of $2\pi/q$; since $2\pi/q \sim 0.2 - 1$ μm, $g_2 - 1$ probes the dynamics on a microscopic length scale. $g_2 - 1$ was renormalized to the degree of correlation after 2 seconds.

2.4 DIGITAL IMAGE ANALYSIS

For the evaluation of keratin and keratin/actin composite networks, digital image analysis was employed to assess structural and dynamic properties of these systems. The used algorithms where designed, written and implemented in the MATLAB environment (MathWorks, Natick, USA).

2.4.1 *Determining the Characteristic Mesh Size*

One of the key parameters used to quantify the network structure is it's mesh size. The cytoskeletal network investigated in this work, however, always exhibit a wide distribution of mesh sizes within one network. Hence, a mesh size, represented by just one figure, is not easily defined. One has

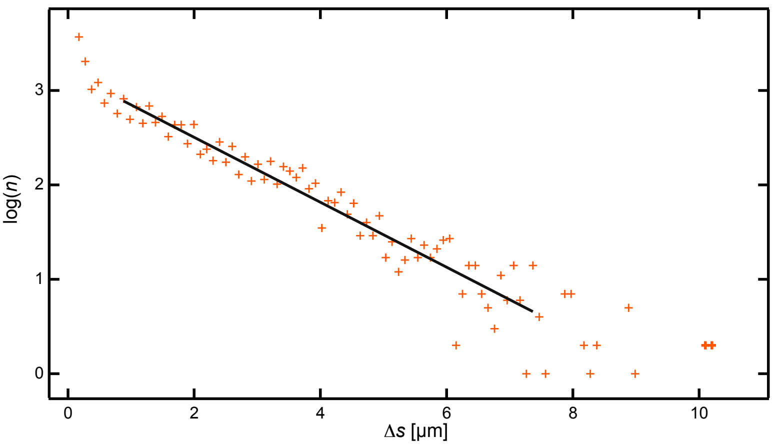

Figure 2.2: The network morphology is quantified by evaluating the distribution of distances between neighboring structures. As shown in the depicted example, the histograms of distances Δs exhibit an exponential decay (orange crosses: data, black line: linear fit to the logarithmized data). The negative inverse slop of the fit gives the characteristic mesh size ξ.

to define a characteristic measure describing the distribution of mesh sizes. Also, the images recorded via confocal microscopy are two-dimensional sections of the three-dimensional network. While, in principle, a three-dimensional reconstruction of the network from confocal stacks is possible, this would not yield additional information in the case of isotropic networks. It is more feasible to quantify the distribution of distances between neighboring structures in one image, yielding the same principal information. Especially if the primary purpose of this parameter is to compare different networks in a quantitative manner. To this end, the edges of the structures have to be defined by applying an intensity threshold to the image. Then, the distances between neighboring structures Δs can be obtained for each line and column of the image. In the case of keratin networks, the resulting distribution of distances can be fitted with an exponential decay with a characteristic decay length, or mesh size, ξ, as shown in Fig. 2.2 (33, 34). The fineness σ can now be defined as the inverse of the characteristic mesh size $\sigma = \xi^{-1}$ and can be thought of as a linear density. While both, σ and ξ can be used to quantify the mesoscopic architecture of a network and compare it to those of others, in many cases σ is the more intuitive measure and will be used in most parts of this work. For extremely small distances the distribution deviates from the exponential form, mainly due to image noise and thresholding artifacts. Very large distances are inherently associated with low statistics. To prevent these artifacts from influencing the outcome, the smallest and largest 10% of the

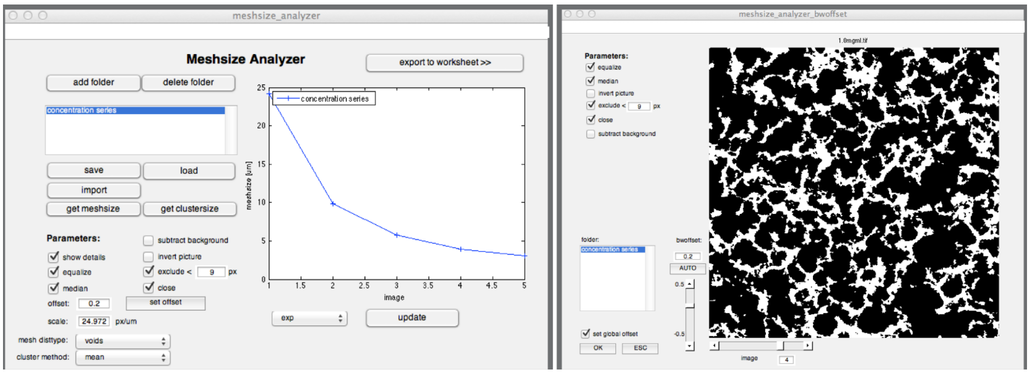

Parameters:
☐ subtract background
☑ show details
☐ invert picture
☑ equalize
☑ exclude < 9 px
☑ median
☑ close
offset: 0.2
scale: 24.972 px/um
mesh disttype: voids
cluster method: mean

Parameters:
☑ equalize
☑ median
☐ invert picture
☑ exclude < 9 px
☑ close
☐ subtract background
folder: concentration series
bwoffset: 0.2
☑ set global offset
image 4

meshsize_analyzer
Meshsize Analyzer
export to worksheet >>
add folder
delete folder
concentration series
save
load
import
get meshsize
get clustersize
set offset
exp
update
concentration series
meshsize [um]
image
0
5
10
15
20
25
1
1.5
2
2.5
3
3.5
4
4.5
5
meshsize_analyzer_bwoffset
1.0mgml.tif
AUTO
0.5
-0.5
OK
ESC

Figure 2.3: The images above show screenshots of the mesh size analyzer software. The left image depicts the main user interface, providing the opportunity to load several image folders for batch processing, to define program parameters and initialize the algorithm. As proper thresholding of each image is essential for a robust mesh size detection, an additional graphical user interface is provided for this purpose (right image).

distance distribution are omitted for the fit. To quantify the morphology of the bundled and clustered structures comprising the network, a similar approach can be applied: Instead of the distances between neighboring structures, the distribution of structure width is obtained. Here, the decay length of the distribution yields the characteristic structure width d. In all cases, the validity of the exponential fit has to be verified. For assessment of the structural diversity within one sample, multiple images where taken at randomly chosen lateral positions throughout the sample. To grant easy access to large data sets and a reliable way to visually verify thresholding, the described algorithm was implemented as a graphical user interface (GUI) based on a MATLAB-routine (Fig. 2.3). This software tool includes options to automatically equilibrate the intensity histogram of the images, apply a median filter for noise reduction, exclude structures below a given size and smooth structure edges. Furthermore, a background subtraction feature is provided which is essential for image series with varying contrast as, for example, in network assembly time series in chapter 4. Here, the average intensity was subtracted for each image of the recorded video followed by a gaussian filter for better dynamic range. Then the threshold was optimized for sensible structure detection above the noise level and held constant throughout the entire video. The onset of assembly ($t = 0$) is equivalent with the appearance of the first structures.

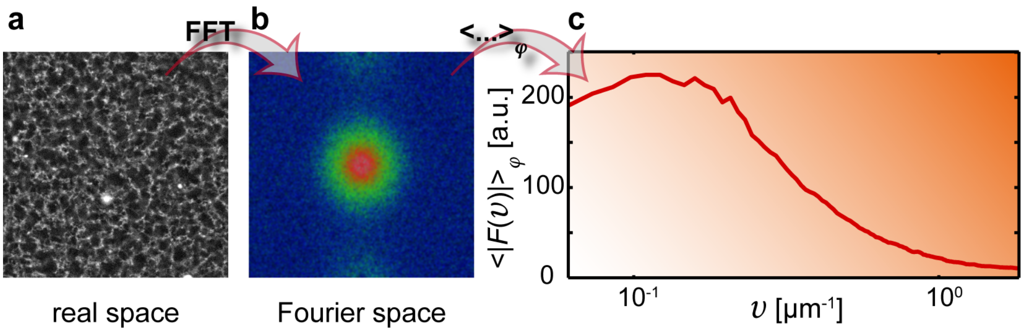

Figure 2.4: Fourier analysis of network images. A confocal slice of an image (a) is subjected to a two-dimensional fast Fourier transform algorithm. The real part of the Fourier transform (b) yields information about the distribution of spacial frequencies. The isotropic nature of the network structure is reflected in the radially symmetry in its Fourier space representation. Therefore, an angular average can be applied to yield the direction independent structure factor $< |F(\nu)| >_{\phi}$, with ν beeing the spacial frequency and ϕ the angle (c).

2.4.2 *Fast Fourier Transform Analysis*

The speed of data acquisition for the investigation of the network assembly has to be adapted to the rapidity of the process, resulting in rather poor signal/noise ratios. Especially in the early phase of assembly, where the fluorescent background is still high and forming keratin structures are relatively dim, image evaluation can be troublesome. The image thresholding, essential for the mesh size determination process described above, is difficult. To make the analysis of network formation dynamics more robust, a Fourier transform approach was developed for the work in chapter 5. The motivation for this approach is the independence of the real part of the Fourier transform from the actual image composition while still yielding the general structural information of interest. This supersedes elaborate drift corrections (which are often even impossible for drift perpendicular to the imaging plane), necessary for the analysis of dynamics via an image correlation algorithm. While it does not give an intuitive measure of the network structure, like for example the mesh size, basing the analysis on such a Fourier transform approach yields a more robust assessment of the formation process. To this extend, each movie frame, associated with the time t, is subjected to a two-dimensional fast Fourier transformation (FFT; Fig. 2.4 a). The isotropic nature of the networks results in a radially symmetric representation in the Fourier space (Fig. 2.4 b). Therefore, an angular average routine is applied, yielding the orientation-independent contribution of each spacial frequency, the structure factor $< |F(\nu)| >_{\phi}$ (Fig. 2.4 c). The form of the structure factor then provides information on the general architecture of the network. A peak, for example, indicates the dominance of a certain spacial frequency and therefore distance in the image. However, it should be noted that many other factors, such as higher harmonics or image brightness and contrast, also influence the structure factor. For better visualization, data is smoothed with a 3 data points rolling average. To compare the evolution of different samples, it can be of avail to regard the change of the structure factor at a fixed spacial frequency as a function of time (see inset in Fig. 5.2 j).

2.5 TRACKING OF SHEARED NETWORKS

For the evaluation of networks under mechanical load, tracking their local displacement while shearing can yield valuable information. To this end, a tracking software based on a correlation algorithm was developed. Here, one challenge is the large amount of recorded data (commonly 5-10 GB per sample). To facilitate tracking, z-stacks are preprocessed to yield a y-projection of a specified region (Fig. 2.5a). The resulting side-view cross-section can then be used to track local network displacement. Since the z-position of the sample may drift slightly throughout the course of the experiment, it is necessary to first track the lower boundary of the sample to establish a frame of reference. Then each image is divided into several regions of interest, or bands, each at a different distance to the sample surface and spanning the width of the image (Fig. 2.5 a). The displacement of each region is then tracked using a FFT-based correlation algorithm, yielding the horizontal frame-to-frame displacement Δx of the network corresponding to a displacement of the upper surface d and as a function of distance to the lower surface (Fig. 2.5 b). To prevent artifacts due to drift/sliding of the lower surface, the displacement of the lowest region of interest can be defined as stationary. Attaining this data for multiple deformation steps then allows to construct a deformation profile of the investigated network (Fig. 2.5 c). Additional consideration on how to better interpret the data are made in chapter 6.

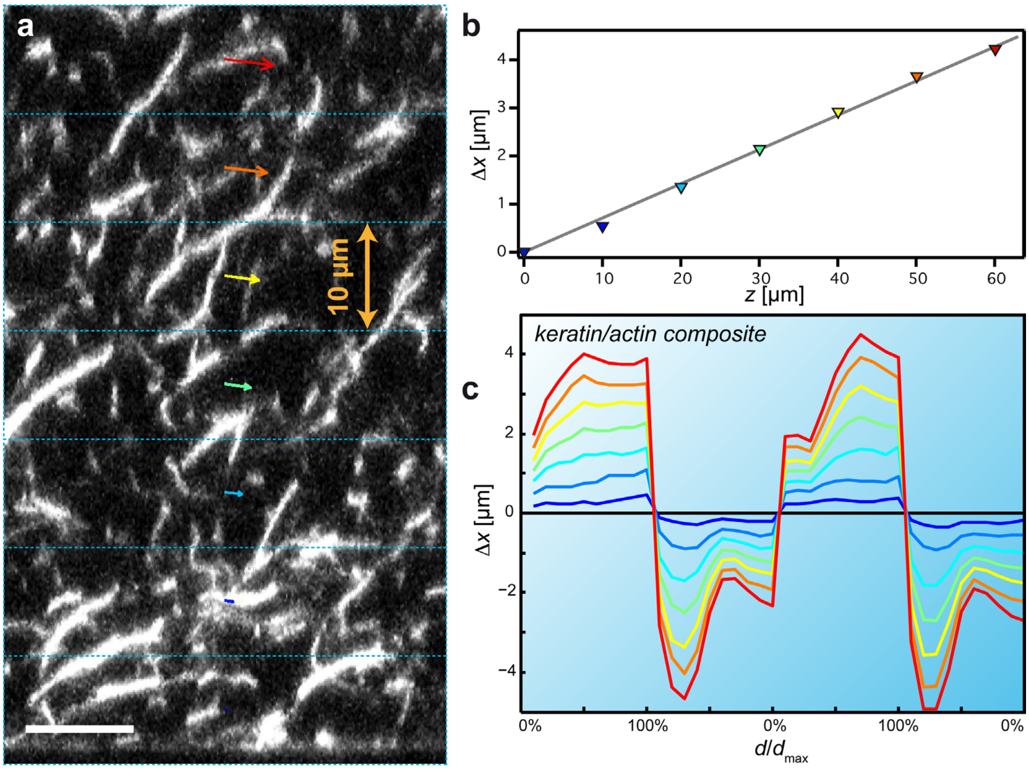

Figure 2.5: Displacement analysis of sheared networks. (a) Projection of confocal stack into x-z plane overlaid with regions of interest. The arrows indicate the relative displacement of each region with respect to the previous position. (b) Displacement Δx per shear step of each region as a function of distance to the lower surface, z. The gray line is a linear fit to the data. The marker colors relate to the arrows in (a). (c) Displacement Δx as a function of the absolute displacement of the upper surface d relative to the maximum displacement $d_{\text{max}} = 200$ µm. The scale bar denotes 10µm.

3

INTRODUCTION TO KERATIN INTERMEDIATE FILAMENTS

The primary focus of this thesis is on intermediate filaments formed from keratin 8 and keratin 18 proteins. The following chapter will therefore provide a short introduction to this field. While reconstituted actin networks also contribute to the present work, they have been described in great detail before(35–37).

Most metazoan cells express intermediate filaments as a major constituent of their cytoskeleton. In contrast to their highly conserved actin and tubulin counter parts, intermediate filament proteins comprise a large and diverse family. By genome analysis, at least 70 genes have been found to encode intermediate filament proteins in humans with expression highly specific to cell type and differentiation(38). According to sequence identity and tissue distribution they have been divided into six groups(39–41): Group I and II are comprised of cyto-keratins, while group III contains vimentin-like intermediate filaments, including vimentin, desmin and glial fibrillary acidic protein (GFAB). The neurofilament triplet NF-L, NF-M and NF-H are found in group IV and the nuclear lamins make up group V. Finally, the eye lens proteins phakinin and filensin can be defined as group VI(41). One of the primary functions of cytosolic intermediate filaments is to provide structural integrity. In conjunction with desmosomal cell-cell- and cell-matrix-junctions, they form an intra- and inter-cellular network of high resilience and flexibility(42). Furthermore, recent studies provide evidence for a cytoprotective function under metabolic stress(43). Nuclear lamins are important for chromatin organization, gene regulation and signal transduction. Associated pathologies, often called laminopathies, range from Emery–Dreifuss muscular dystrophy to the accelerated ageing in Hutchinson–Gilford progeria syndrome(44). Neurofilaments can form liquid crystal like phases in neurons and play an important role in the mechanical stability of neuronal processes(45, 46).

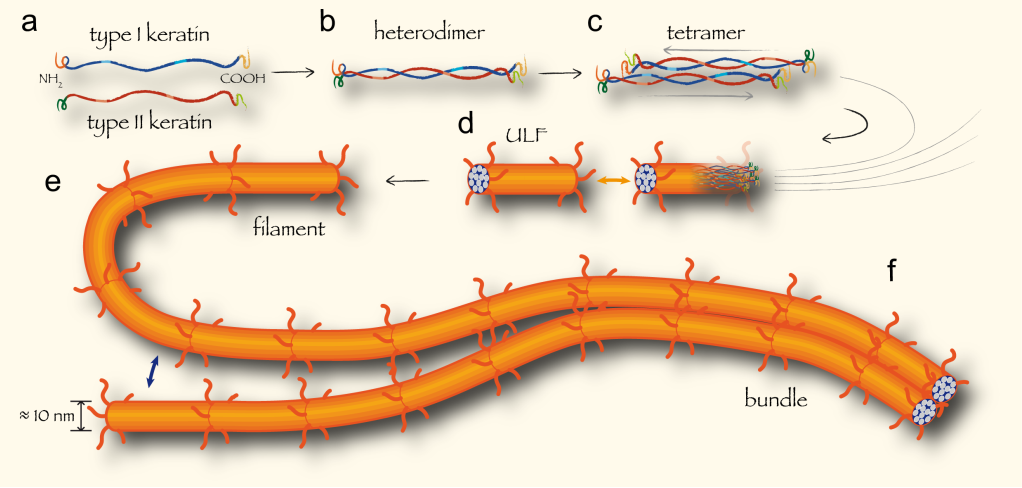

Figure 3.1: Keratin intermediate filament assembly. (a) An α-helical central domain (dark red and blue), interleaved with non-α-helical "linkers" (light red and blue), is flanked by unstructured N-terminal (head) and C-terminal (tail) domains (green and yellow). (b) One basic (for example K8) and one acidic (for example K18) keratin can form a heterodimer. (c) Such heterodimers then associate in an anti-parallel and half staggered manner to tetramers. (d) Several tetramers combine to form short, full-width complexes (unit-length filaments; ULF). (e) They longitudinally associate to form the characteristic, $\sim$ 10 nm wide filaments. (f) These filaments then have the potential to further associated to bundles.

3.1 FILAMENT STRUCTURE AND ASSEMBLY

Despite their diversity in sequence and cell context, all cytoplasmic intermediate filament proteins share a common structural layout: A central α-helical domain (rod), interleaved with non-α-helical linkers, is flanked by unstructured N-terminal (head) and C-terminal (tail) domains (Fig. 3.1a). The largest subgroup of the intermediate filament protein family comprises keratins, with 28 type I (acidic) and 26 type II (basic) keratins. Keratins are particularly abundant in cells forming epithelial layers. Their principal assembly subunit is a heterodimeric coiled-coil complex of one acidic and one basic keratin(47) (Fig. 3.1b). These dimers then further associate to staggered tetramers in an antiparallel fashion, yielding an apolar building block (Fig. 3.1c). This symmetry is propagated to the filament level and renders all intermediate filaments as non-polar objects. During filament assembly, several tetramers combine to form short, full-width assembly intermediates, termed "unit-length filaments" (ULF), with 16-20 molecules per cross-section (16) (Fig. 3.1d). Such ULF then longitudinally connect to form the characteristic $\sim$ 10 nm wide filaments (Fig. 3.1e and Fig. 3.2). These processes are, in contrast to the polymerization of filamentous actin and microtubules, independent of the hydrolysis of nucleotides. While the

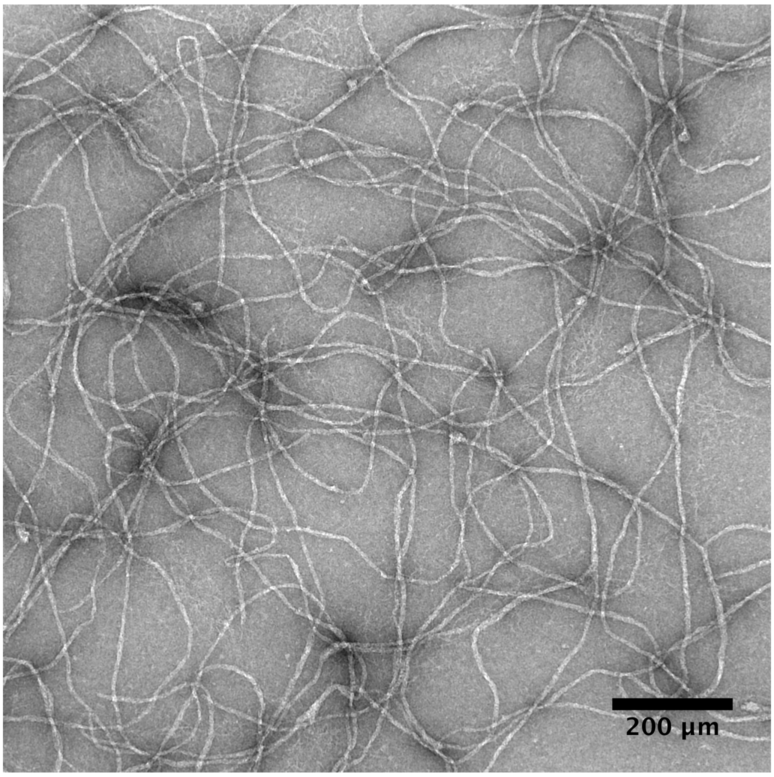

Figure 3.2: TEM image of keratin filaments. Transmission electron microscopy (TEM) reveals an array of single keratin filaments. While the average diameter of such bundles is ~ 10 nm, it can vary substantially along the filament contour. Here, due to the absence of salt, filaments do not form bundles. Please note the low persistence length of individual filaments.

N-terminal head seems to be essential for the elongation process, deleting the tail still allows for filament formation (19). It is believed that the unstructured tail domains protrude from the filament surface and it has been demonstrated that they play an important part in the intrinsic potential for lateral association of certain keratin filaments to bundles(48) (Fig. 3.1f). This intrinsic bundling capability is especially interesting since several proteins have been identified to tether intermediate filaments to other cytoskeletal systems, but only few have been found to directly crosslink intermediate filaments with each other(49, 50).

In living cells, keratin filaments assemble into dense networks of filaments and bundles (Fig. 3.3). Nascent filaments emerge in the cell periphery and are then continuously transported towards the nucleus in an actin dependent manner while being incorporated into the existing network(51). Here, they associate to thick bundles, characteristic for the perinuclear region. They are then disassembled again into soluble subunits which can

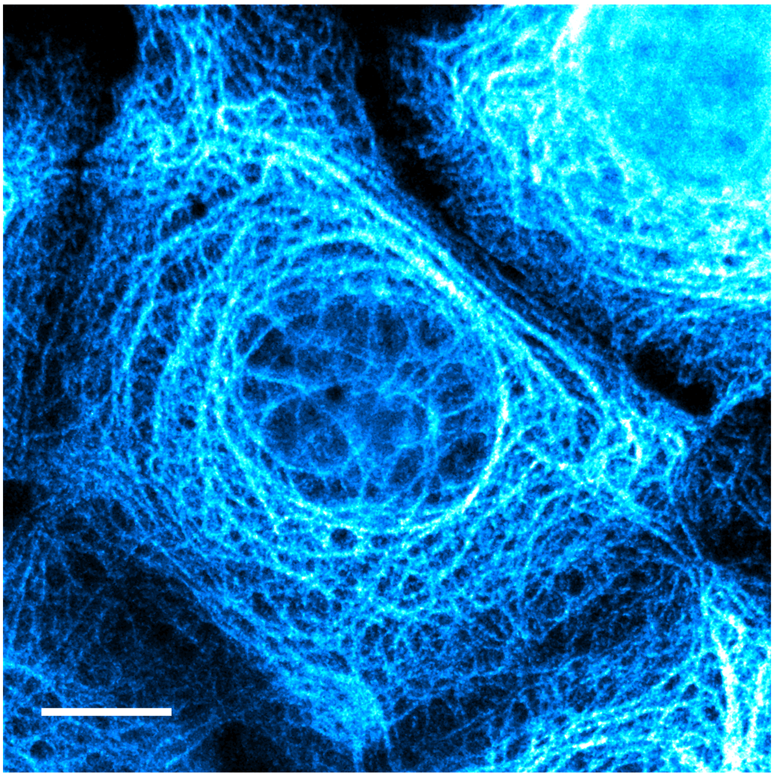

Figure 3.3: STED image of a MCF7 epithelial cell. The keratin cytoskeletal is visualized via immunostaining of keratin 8. While structures near the periphery are fine and filamentous, they become increasingly bundled towards the perinuclear region. Also, the connections to neighboring cells are clearly visible. The scale bar represents 10 µm.

diffuse to the cell periphery where they can be incorporated into yet another cycle(52). This process is independent of protein synthesis and allows for continued remodeling of the keratin cytoskeleton(53). Due to their apolar nature, intermediate filaments cannot serve as tracks for molecular motors. However, they have been shown to be associated with motor protein complexes, and therefore exhibit a surprising degree of dynamics and restructuring within cells(51, 52, 54). In addition, they can be very quickly mobilized by the action of kinases(55). Recently, keratin network reorganization triggered by sphingosylphosphorylcholine (SPC) has been demonstrated to act via kinase induced keratin phosphorylation(56, 57).

3.2 *in vitro* INVESTIGATIONS

The assembly kinetics in the early stages of filament assembly have been addressed *in vitro*(10, 11, 16, 48). Here, primarily transmission electron microscopy was used to investigate the different stages of assembly and the general properties of keratin intermediate filaments. One important difference to other intermediate filaments is the rapidity of filament formation, which, in the case of keratin 8/18, was determined to be $\sim$ 80 times faster than that measured for vimentin(11). The persistence length of $l_\mathrm{p} \approx 300$ nm is relatively small compared to that of other cytoskeletal filaments (actin filaments: l_p $\approx$17 µm; microtubules: l_p $\approx$5 mm)(11, 58). Studies probing the properties of single filaments via atomic force microscopy revealed an astonishing extensibility of more than 200%(59). Furthermore, the functional role of several protein subunits, such as the head domain, could be elucidated(19). Bundling of keratins *in vitro* has been observed to be induced predominantly by salt and to be, in part, mediated by keratin tail domains(48). Only in some rare cases also bundling induced by specific keratin associated proteins has been observed *in vivo*(49, 60–62). For other types of intermediate filaments, such as vimentin and neurofilaments, an effect of divalent salts on the macrorheological properties of these system has been reported(13, 63).

Recent years have seen substantial progress in our understanding of the assembly of single intermediate filaments, and intracellular networks with a convoluted composition of single and bundled filaments have been observed for a long time. Still, insight into the link between these two areas, the formation of higher order assembly structures and networks, remains elusive. The predominant expectation and assumption is that the assembly process results in thermally equilibrated network structures(64). This is partly due to the fact that this it is the simplest assumption which can be made. However, this postulation is essentially based on the lack of experimental evidence on the structure formation process due to the inherent complexity of such networks and the absence of an adequate model system. Yet, a thorough understanding of the assembly kinetics on all length and times scales is essential to facilitate any progress in our understanding of the observed intracellular structures. Hence, a well-controlled model system of three dimensional keratin networks in near physiological conditions is urgently needed.

4

ASSEMBLY KINETICS DETERMINE STRUCTURE OF KERATIN NETWORKS

In this chapter, a novel *in vitro* model system of the keratin cytoskeleton is introduced, based on reconstituted keratin 8/18 (K8/K18) intermediate filaments. Using this setup, it is shown that such keratin networks assemble into kinetically trapped structures far from equilibrium. It is the competition between two processes, filament elongation and their lateral association to bundles and clusters, which defines the resulting network morphology. Thus, controlling the rates of these two processes directs the micro- and mesoscopic network morphology(65).

4.1 BUNDLING AND CLUSTERING OF KERATIN FILAMENTS *in vitro*

While most *in vitro* work on keratin intermediate filaments has so far been carried out under low ionic concentrations(10, 48, 60, 66), the experiments presented here aim to assemble keratin networks at much higher salt concentrations comparable to those in living cells. However, initial experiments produced mesoscopic clusters of concentrated protein, as shown in Fig. 4.1a. To resolve the substructure of the clusters we performed transmission electron microscopy (TEM) of fixed and negatively stained samples. The electron micrographs reveal an assembly of tightly bundled filaments (Fig. 4.1b). While bundles exhibit diameters of 100 nm and more, their filamentous substructure remains clearly discernible. Interspersed in this network of bundles are single filaments, merging in and out of larger bundle arrays. Not only do these findings verify the existence of intact filaments, they furthermore reveal specific filament-filament interactions resulting in bundling. The unstructured carboxy-terminal tail domains of intermediate filament proteins are a probable candidate for mediating such bundling interactions as they have been observed to protrude from the filament body in the case of neuronal intermediate filaments(45, 67). For other types of keratin, such as keratins 5 and 14, the tail of at least one species has been

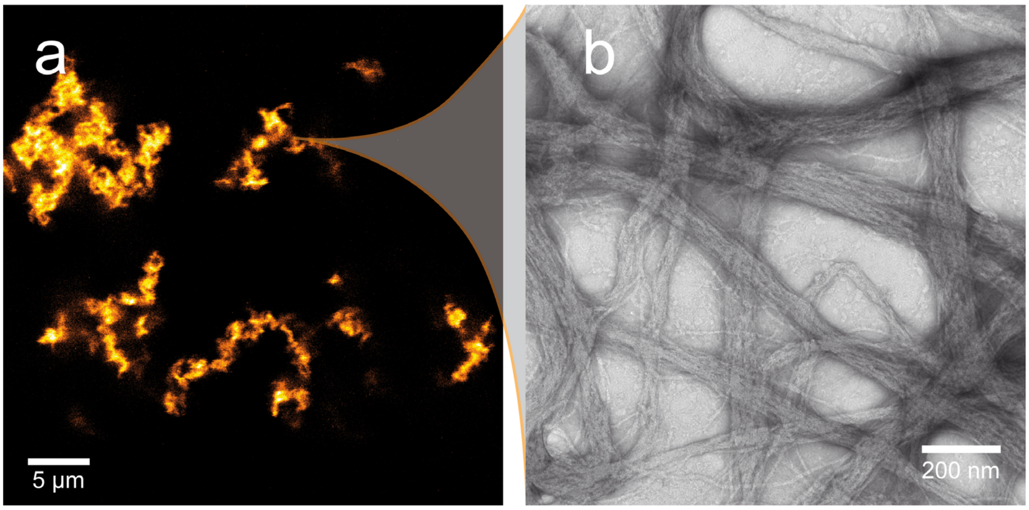

Figure 4.1: Keratin forms clustered structures at low protein concentrations. (a) Confocal image of assembled keratin at a concentration of $c_K = 1$ μM. Rather than a homogeneous network of filaments these conditions result in heterogeneous clusters. (b) Electron micrograph of the substructure of a cluster similar to those shown in (a). Single filaments with a diameter of ≈ 10 nm associate to thick bundles with a wide distribution of bundle diameters

reported to be significant for bundle formation(48). For K8/K18, however, the site of interaction remains to be identified.

In the context of network formation these observations of bundling indicate two different kinds of association processes to play an important role in the course of network assembly: Filament elongation and their lateral aggregation into bundles. If the time scales of these processes are not clearly separated, the interplay of both will govern the assembly dynamics. Therefore, comprehension of the temporal hierarchy of elongation and bundling processes is important for a controlled formation of networks. Directly after initiation of assembly ($t < 0.5$ s), subfilamentous aggregates of proteins are observed in electron microscopy (Fig. 4.2a). At $t = 1$ s, these aggregates have already evolved into properly assembled filaments. Moreover, the filaments are associated to loose bundles (Fig. 4.2b). The bundling process continues to yield massive bundles after $t = 30$ s (Fig. 4.2c). The results highlight the great speed of keratin assembly under the given conditions. Observations revealing K8/K18 filaments to assemble at least 80 times faster than vimentin intermediate filaments corroborate these findings(11). They furthermore demonstrate that filament bundling and elongation advance on comparable time scales. However, bundling is still proceeding after filament polymerization seems to be completed. The wide distribution of bundle sizes (see Fig. 4.1b) is strong evidence for a sce-

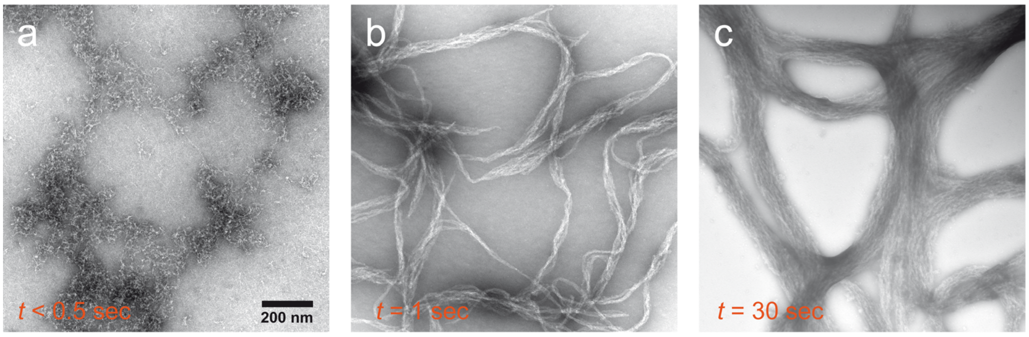

Figure 4.2: Temporal hierarchy of keratin bundle formation. Electron micrographs show the network morphology obtained at different times t, as denoted in the figure. (a) Right after initiation of polymerization the keratin proteins are still in a pre-filamentous state. (b) At $t = 1$ s long filaments are loosely associated to thin bundles. (c) After 30 s the vast majority of filaments have aggregated to thick bundles.

nario where bundle growth is limited by kinetic trapping of the system(14): Neighboring bundles and filaments are locked into position and can not further associate to thicker bundles. Therefore, an enhancement of filament elongation should facilitate kinetic trapping, reaching a quasistatic state before filaments are aggregated into clustered bundles. A very direct way to enhance filament elongation and favor kinetic trapping is the increase of protein concentration.

4.2 RECONSTITUTED KERATIN INTERMEDIATE FILAMENT NETWORKS

Due to the high speed of polymerization under these conditions conventional sample preparation techniques fail. Substantial network formation occurs in less than a second. This behavior prohibits pipette mixing for the initiation of assembly as the associated shear forces would destroy the nascent network. We therefore employ a "droplet-fusion" technique as described in chapter 2 (Fig. 4.3c and d). Using this approach we can assemble even samples with protein concentrations of $c_K > 20$ µM in a controlled manner. The result is a dense network with a homogeneous and isotropic morphology over the length scale of millimeters (Fig. 4.3a). In addition, high resolution STED-microscopy is employed to evaluate the networks microscopic anatomy revealing a substructure of clustered bundles (Fig. 4.3b). Thus, the lateral interaction of filaments appears to remain a significant factor even at higher protein concentrations leading to a divergence of morphology on different length scales: While the network is homogeneous on a mesoscopic scale (> 5 µm), it exhibits a pronounced degree of heterogeneity on a microscopic level.

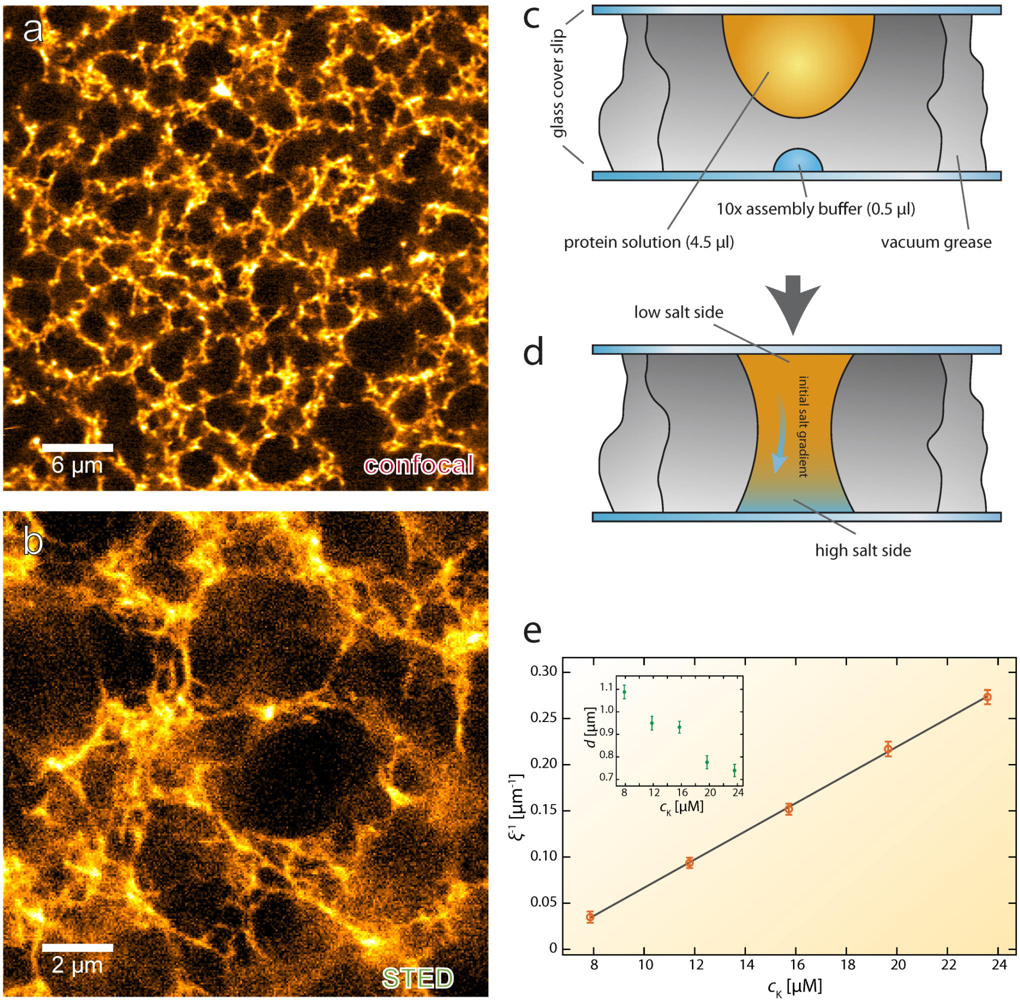

Figure 4.3: At high protein concentrations keratin forms homogeneous networks with a heterogeneous substructure. (a) Confocal image of a keratin network assembled at a protein concentration of $c_K = 20$ µM. The network exhibits a homogeneous morphology on mesoscopic length scales (< 5 µm). (b) STED-microscopy was employed to acquire sub-diffraction resolution, allowing for an assessment of the networks' microscopic anatomy. The image reveals a heterogeneous substructure of clustered keratin bundles. (c) Samples are prepared by the fusion of two small droplets as described in chapter 2. (d) An initial salt gradient is inherent to this technique. Therefore the side where the assembly buffer was applied, termed high salt side, experiences a short peak in salt concentration while the adjacent side, the low salt side, encounters a slower, gradual increase in ionic strenght. Both (a) and (b) depict a network on the low salt side. (e) The characteristic mesh size ξ is inversely proportional to the protein concentration c_K. The width of the structure decreases with increasing c_K (inset).

To better characterize the networks it is necessary to adequately quantify its architecture. This can be achieved by evaluating the distribution of distances between structures via image analysis. For the investigated keratin networks we find an exponential distribution of inter-structure-distances, yielding a characteristic distance, or mesh size, ξ (see chapter 2 for details). Another measure is the apparent width d of the structures, obtained in a similar fashion. We find that ξ is inversely proportional to the protein concentration c_K, as shown in Fig. 4.3e. While a decrease in mesh size is expected as the protein concentration increases, the width of the structures should either increase or remain unaffected in an equilibrated system. Here, however, the structure width d decreases with increasing c_K (inset in Fig. 4.3e). Such a relationship suggests a dependence on the assembly dynamics. In the kinetic trapping scenario described above, for example, an increase in elongation speed would result in a quicker arrest of the assembly process and impede further growth of bundles and clusters.

4.3 INTERPLAY OF NETWORK ASSEMBLY DYNAMICS AND STRUCTURE

To further investigate how the evolution of elongation and bundling dictates the resulting network structure we have imaged the process of network formation in real time. Fig. 4.4a is a composition of multiple confocal images recording the assembly of a keratin network at intermediate concentrations ($c_K = 6$ µM). Due to the scanning nature of the technique each line of an image corresponds to a certain time point t in the assembly process. Repetitive scanning of an entire region additionally allows for evaluation of the structural evolution, assuming that the general structure is the same everywhere in the scanned region. The recorded data shows that the network formation process can be divided into two distinct phases. In the initial phase, immediately after initiation of polymerization, small clusters form within 2-3 seconds (green arrow in figure). In the second phase these objects diffuse and continuously associate to larger structures (blue arrow), reminiscent of the incorporation of keratin precursor structures into the cytoskeletal network *in vivo*(52). The process continues over several seconds until a static network structure is reached. These observations show that the initial formation phase is the process determining the substructure. The subsequent coarsening to larger structures gives rise to a percolating network. However, it does not influence the microstructure, which is trapped in its initial configuration. At higher concentrations, the assembly process is significantly sped up, as shown in Fig. 4.4b. The observed behavior is yet another indication for the kinetically trapped nature of the system.

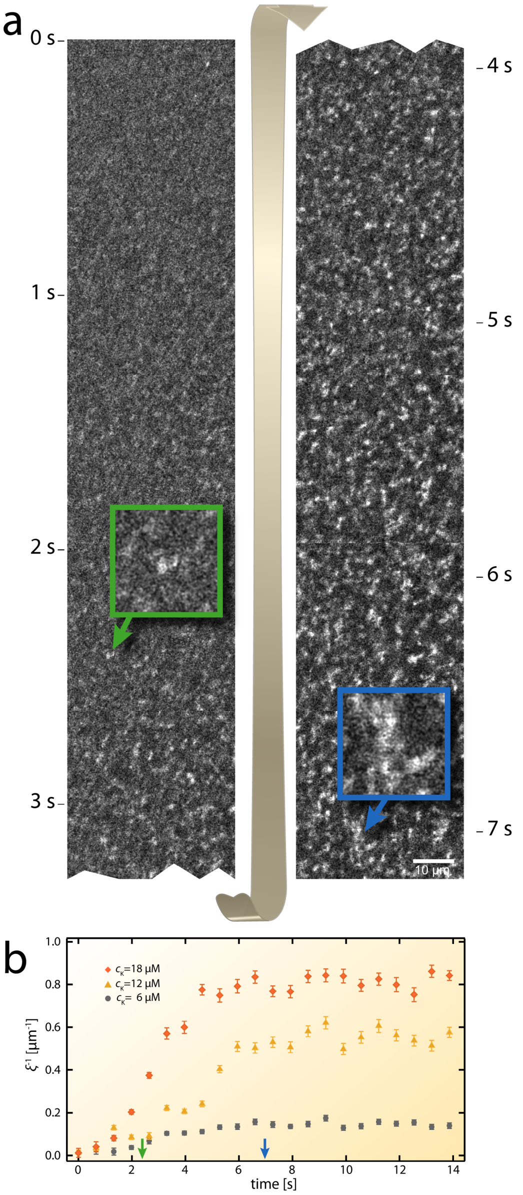

Figure 4.4: Structural evolution of a keratin network. (a) Depicted is a composition of several confocal micrographs. Due to the scanning nature of this technique, each line of an image can be associated with a certain time t after initiation of polymerization. Repetitive scanning of an entire region additionally allows for the evaluation of the 2-dimensional structure. Images are acquired at the high salt side (see Fig. 4.3e) with 0.66 s per image (1.3 ms per line). Small clusters appear within the first seconds (green arrow). These then continuously associate to larger structures (blue arrow). Protein concentration was $c_K = 6$ µM. (b) The speed of the assembly, as quantified by the evolution of the inverse mesh size ξ^{-1}, depends on the protein concentration (see legend in figure).

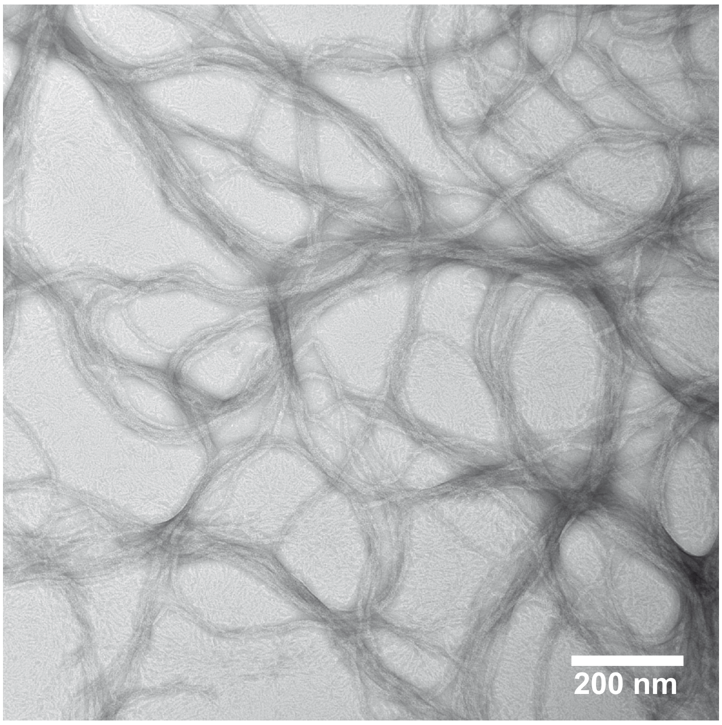

Figure 4.5: Network structure depends on the course of assembly. Electron micrograph of negatively stained bundle network after stepwise assembly: First filament elongation was triggered by a change in pH. Then bundling was induced by addition of salt. Loose bundles, much smaller than those obtained by simultaneous elongation and bundling (compare Fig. 4.1b), are observed.

The keratin system allows for a key experiment to test this hypothesis. If the network is in equilibrium, its morphology should not depend on the path of formation. If, however, such a dependence exists, the network is indeed in a kinetically trapped out-of-equilibrium state. Since bundling is only induced in the presence of salt while filament elongation can also be initiated by a change in pH, we can separate both processes: First, elongation is initiated by dropping the pH to 7.8 in the absence of salt. Then bundling is induced by the addition of salt while the pH is held constant. Thus, the final conditions are identical to those of experiments with simultaneous elongation and bundling while the path of formation is completely different. A dependence on the formation path is confirmed by the electron micrograph shown in Fig. 4.5. Here, the observed bundles are much thinner than those observed for a preparation with simultaneous elongation and bundling (compare Fig. 4.5 and Fig. 4.1b). The reduced mobility of entangled filaments impedes lateral diffusion and therefore bundling. A kinetically trapped state is reached before pronounced bundling can occur. The results discussed so far lead to one underlying mechanism: tuning the

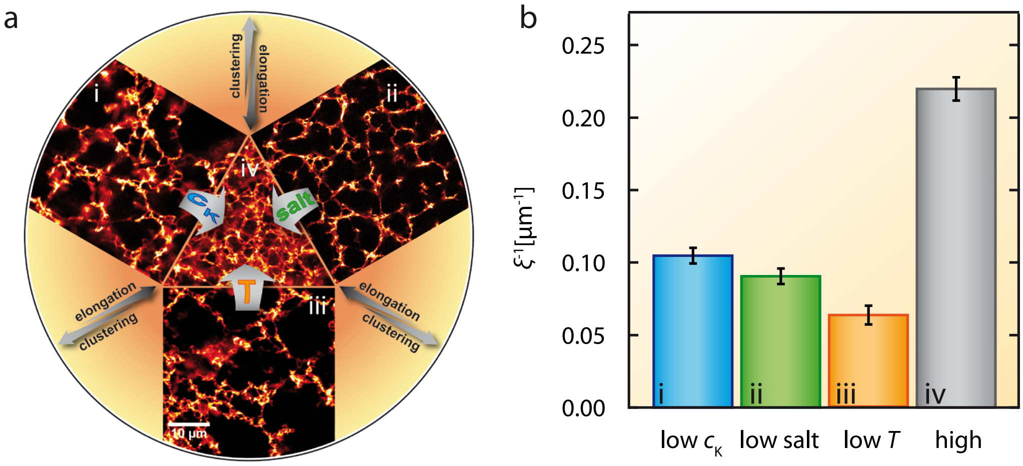

Figure 4.6: Fast elongation results in less clustering. (a) The fine network in the center triangle (iv) was formed at elongation favoring conditions: high keratin concentration ($c_K = 12$ µM), high temperature ($T = 37$°C), and higher salt concentration during the initial phase of assembly, as described in the main text and Fig. 4.3. For the network in (i) the concentration was reduced to $c_K = 6$ µM while all other parameters remained constant. Similarly, (ii) depicts a network where the salt concentration was low in the initial assembly phase and increased gradually during formation. For the network in (iii) the temperature during assembly was reduced to $T = 10$°C. Increasing any of these parameters, as indicated by the wide arrows between images, leads to a finer network substructure. The balance between elongation and clustering is shifted as indicated by the thin arrows. (b) The dependence of the network structure on these parameters is reflected in the inverse mesh size ξ^{-1}. The individual bars are associated with the images in (a) as indicated by the roman numbers.

relative time scales of bundling and elongation modifies the resulting network morphology. So far we have confirmed this for an enhancement of elongation by increasing the keratin concentration (see also Fig. 4.6 i and vi). Similar effects should be achievable through alteration of the relative time scales by other means.

If the ratio of the time scales was temperature dependent, this would allow for an alternative way of tuning: For an Arrhenius like behavior of the interactions, for example, an increase in temperature should shift the ratio in the direction of the process with the lower activation energy. Indeed, assembly of proteins at $T = 37$°C yields less clustered networks than assembly at $T = 10$°C (Fig. 4.6 iii and iv). Thus, the increase in temperature shifts the balance towards filament elongation and consequently to a finer network substructure.

A third method to influence the time scales is via different ways of introducing assembly conditions. Since the addition of salt triggers both elongation and bundling, their temporal relationship will be reflected in the salt dependence of the formation process. Screening the electrostatic repulsion of the proteins with a short peak in salt concentration during the initial phase of assembly should enhance the interaction compared to a case where the salt concentration is increased gradually. Both settings are present in a sample prepared by "droplet-fusion", due to the initial salt gradient inherent to this technique (see Fig. 4.3c and d). Similar to an increase in temperature, the faster elongation process would be favored by an initially high salt concentration. The images in Fig. 4.6 (ii: slow increase of salt concentration, iv: high initial salt concentration) confirm this hypothesis.

4.4 CONCLUSION

Combining results from fluorescence and electron microscopy allows for comprehensive insight into the structure of reconstituted keratin networks on mesoscopic and microscopic length scales. In concert with experiments investigating the assembly dynamics of such networks these results reveal an intricate interplay of filament elongation and bundle formation. We can therefore conclude that the ratio of elongation and bundling rates is indeed the principal parameter governing the structure of kinetically trapped keratin networks. The formation process of keratin networks described here in conjunction with their out-of-equilibrium nature is a remarkable example of how a relatively simple *in vitro* system may exhibit a plethora of structural features reminiscent of those observed in living cells. The complex environment of the cell has so far defied insight in the regulation mechanisms that control the keratin cytoskeleton configuration. The well-defined model system described here is ideally suited to identify the contributing processes. The mechanism of tuning the balance between elongation and bundling may indeed represent an important regulatory mechanism *in vivo* during the constant remodeling of the cytoskeleton and the incorporation of *de novo* keratin filaments. It is likely, however, that the cell relies on different means of influencing elongation and bundling kinetics, such as keratin-associated proteins.

5

HSP27 AFFECTS THE ASSEMBLY DYNAMICS AND STRUCTURE OF KERATIN NETWORKS

In the following chapter, the influence of the keratin-associated small heat shock protein Hsp27 on the complex interplay between filament elongation and bundling will be discussed. Again, the controlled environment of the *in vitro* setup is crucial for unraveling the physics governing the influence of Hsp27 on keratin network assembly dynamics. Notably, the non-equilibrium aspects of this system, discussed in chapter 4, are key for the observed effect, confirming the influence of keratin-associated proteins on kinetic trapping.

5.1 SMALL HEAT SHOCK PROTEINS AND INTERMEDIATE FILAMENTS

Heat shock proteins are essential for the cell's response to stress. They protect the cell by facilitating correct protein folding and preventing deleterious protein aggregation (68). Small heat shock proteins (sHsps), with a monomeric size ranging from 9-47 kDa, have been associated to processes ranging from RNA stabilization to apoptosis (20, 21, 69–72). Their activity can be regulated by modulating their oligomeric structure (70, 73, 74). There also is growing evidence of sHsps interacting with the cytoskeleton(75–81). This is especially interesting in light of the many fundamental functions and critical processes associated with the cytoskeleton, ranging from tissue differentiation during embryogenesis to the metastatic behavior of tumor cells (82–84). Hence, precise control of the cytoskeletal architecture is of paramount importance. Although intermediate filaments are one of the primary contributors to the cell's structural integrity, relatively little is known about how the cell governs the organization of its intermediate filament cytoskeleton(85, 86). *In vivo*, the network morphology and substructure depends on the location within the cell: Peripheral networks are generally much finer compared to the heavily bundled keratin structures in the perinuclear region (52, 56). At the same time, only few keratin bundling proteins - as they are abundant for other cytoskeletal filaments, such as actin filaments - have so far been identified (49, 50). Chapter 4 demonstrated that keratin filaments have intrinsic bundling capabilities and that the assembly dynamics have a severe impact on the resulting network structure. Interestingly, the small heat shock protein Hsp27 has been reported to colocalize with keratin 8/18 intermediate filaments *in vivo* and to have an impact on the material properties of reconstituted intermediate filament gels (78). However, the underlying mechanisms of Hsp27-controlled keratin network assembly have so far not been thoroughly explored. Here, we show that Hsp27 affects the architecture of kinetically trapped keratin networks by altering their assembly dynamics. Our data demonstrates the relevance of the C-terminal keratin 8 tail domain for the effect and elucidates the underlying physics.

5.2 INFLUENCE OF HSP27 ON KERATIN NETWORK MORPHOLOGY

We investigate the impact of Hsp27 on the basis of the model system of reconstituted keratin 8 and keratin 18 intermediate filaments, introduced in chapter 4. This does not only enable the precise control of all relevant environmental parameters, it moreover allows for a direct assessment of the effect without potential secondary elements, such as protein phosphorylation, variations in gene expression or redundancy effects of related sHsps. While the investigated networks are homogeneous on mesoscopic length scales (> 10 μm) a substantial degree of bundling and clustering dominates the networks microscopic morphology (Fig. 5.1a). These microscopic architectural features define the mechanical properties of the macroscopic network. It therefore is interesting to observe a pronounced alteration of the network's morphology when it is assembled in the presence of Hsp27 (Fig. 5.1b-d). The perceived fineness of the network increases significantly. Moreover, the microscopic substructure appears less clustered and more regular. The strength of the effect depends on the molar ratio R of monomeric Hsp27 concentration c_{27} to monomeric keratin concentration c_K. Assuming a native form of Hsp27 composed of ~ 16 subunits and $\sim 16 - 20$ molecules per keratin filament cross-section, R also roughly represents the ratio of Hsp27 oligomers per longitudinal filament subunit repetition (16, 70). To evaluate this effect in a more quantitative fashion we determine the fineness σ of the network, with $\sigma = \xi^{-1}$ where ξ is the characteristic distance in the network, as introduced in chapter 4. The gathered data reveals a monotonic increase of σ as a function of R over the range of examined Hsp27 concentrations, as shown in Fig. 5.1e. Interestingly, even relatively small amounts of Hsp27 ($R = 0.5$) are sufficient to have a measurable effect on the network structure. In addition to the Hsp27-induced

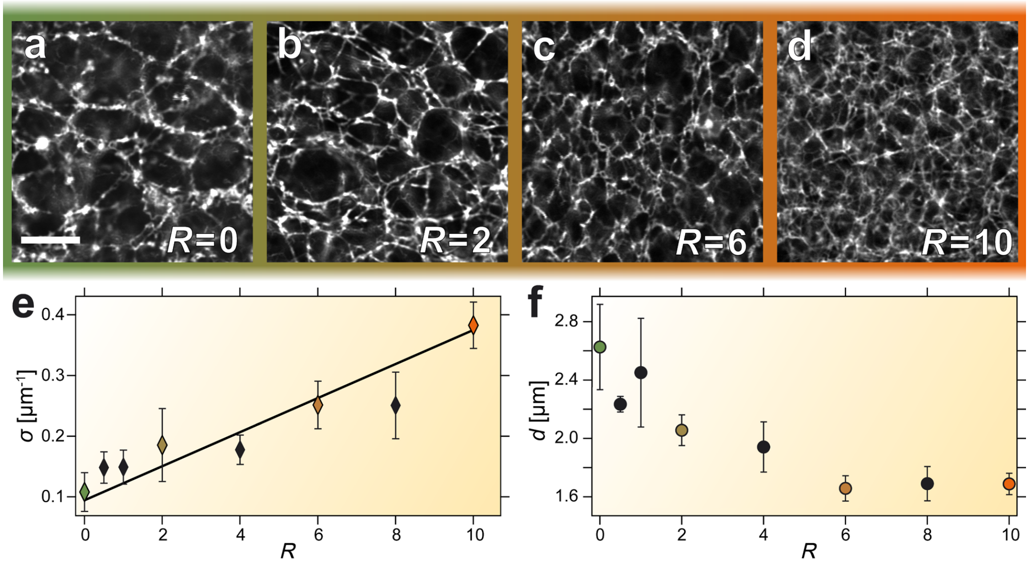

Figure 5.1: Hsp27 causes an alteration of keratin network structure. (a) In the absence of Hsp27, keratin intermediate filaments assemble into heterogeneous networks of clusters and bundles. (b-d) The presence of Hsp27 during assembly leads to a finer, more homogeneous network morphology. The strength of the effect depends on the molar ratio R of Hsp27 to keratin, as denoted in the figure and illustrated by the color gradient from green ($R = 0$) to orange ($R = 10$). (e) The network fineness σ (see chapter 2 for details) monotonically increases with growing R. The linear fit to the data (*black line*) is associated with a correlation coefficient of $r = 0.86$. (f) The characteristic structure width d decreases with increasing R. All error bars are the standard deviation of data from multiple images acquired at different locations in the sample. The keratin concentration was $c_K = 8$ µM for all samples. All images are confocal slices. The scale is the same for all images. The scale bar denotes 10 µm.

increase in fineness, we observe less clustering and a more homogeneous network structure throughout the sample. This observation is underlined by a reduction of the characteristic structure width d, suggesting a lesser degree of bundling and clustering in the network's substructure with increasing R (Fig. 5.1f).

5.3 HSP27-INDUCED INHIBITION OF COARSENING DYNAMICS

As described in chapter 4, there are regions of faster and slower network assembly in one sample due to the method of sample preparation. Interestingly the observed Hsp27-effect is more pronounced where network formation is fast. The key to the Hsp27-induced differences in network structure might therefore be found in the details of the network's assembly dynamics. To investigate this in more detail, we assess the network formation process in real time. Within the first second after initiation of assembly, a dense arrangement of small structures emerges from the fluorescent background (Fig. 5.2a). These structures then continuously grow and get more defined to result in a network like array (Fig. 5.2b and c). On a longer timescale, these structures then undergo a coarsening process of continued cluster association until finally reaching a quasi-static state (Fig. 5.2d). While the first phase of assembly of a sample with $R = 10$ is very similar to that of an Hsp27-free sample, the coarsening dynamics in the second phase is significantly suppressed resulting in a much finer final network (compare Fig. 5.2 a-d to e-h). Here, a direct extraction of the fineness, as employed earlier, is unfeasible due to the very low signal to noise ratio in the early stage of assembly.

However, to assess the evolution of the system's spatial configuration the 2-dimensional Fourier transformation yields valuable information as represented by the structure factor $< |F(\nu)| >_{\phi}$ (see chapter 2 for details). $< |F(\nu)| >_{\phi}$ is a measure of the contribution of periodic structures with a wavelength $\lambda = \nu^{-1}$. Fig. 5.2i and j show $< |F(\nu)| >_{\phi}$ for images taken at different times during the assembly for $R = 0$ and $R = 10$, respectively. The emergence of the network structure is reflected by a peak at $\nu \approx 0.2$ μm^{-1}. The peak then continually becomes increasingly pronounced as the network gets more defined. The successive increase of $< |F(\nu)| >_{\phi}$ at smaller ν is a finger print of the observed coarsening. This coarsening is much less pronounced in the presence of Hsp27 (Fig. 5.2j). The time course of the assembly can be visualized by plotting the temporal evolution of the structure factor for a fixed spacial frequency. The inset in Fig. 5.2 j shows $< |F(t)| >_{\phi}$ for $\nu = 0.11$ μm^{-1}, corresponding to the fineness of a fully assembled network (see Fig. 5.1e, $R = 0$). For the reference sample ($R = 0$), $< |F(t)| >_{\phi}$ increases continuously until saturating for $t > 13$ s, indicating a halt of assembly dynamics. For $R = 10$, however, this halt is already observed at $t \approx 5$ s, after which no significant change in the structure factor - and hence the network morphology - is observed.

To make the effect more prominent, it might be of avail to reduce the bundling tendencies by lowering the ionic strength. However, fluorescence microscopy is not suited for observations on the sub-bundle length scales necessary to properly investigate the resulting loosely bundled networks. Here, transmission electron microscopy (TEM) allows access to the relevant length scales. In the absence of Hsp27, keratin filaments associate to bundles in a buffer with 3 mM $MgCl_2$ as the only salt (Fig. 5.3a). If, however, assembly is conducted in the presence of Hsp27 ($R = 10$), bundles are no longer observed. Instead, we find single filaments, heavily decorated with characteristic ~ 10 nm wide Hsp27 oligomers (Fig. 5.3b) (87). This is rem-

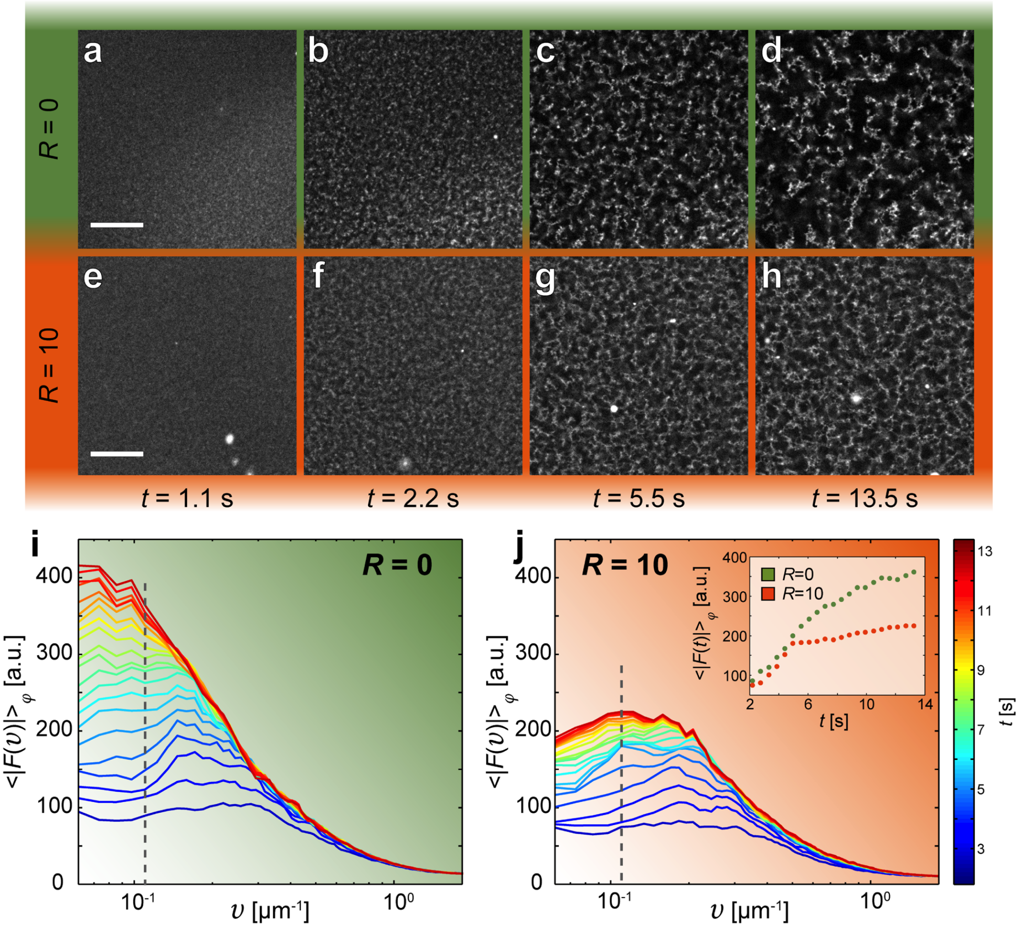

Figure 5.2: Hsp27 inhibits cluster association and network coarsening. (a-d) During network assembly, small nascent structures can associate to larger clusters, leading to a coarsening of the network structure. The presence of Hsp27 inhibits this process, resulting in a finer network (e-h). This difference is reflected in the time evolution of the structure factor $< |F(\nu)| >_{\phi}$, where ν is the spacial frequency. (i) For $R = 0$, a characteristic shift to lower spacial frequencies (i.e. lower fineness) with time is observed (blue $\approx$ 1 s, red $\approx$ 13 s). This shift is less pronounced for a sample with $R = 10$ (j). Here, the coarsening comes to a halt much earlier than for the sample with $R = 0$. This is also emphasized by evaluating the temporal evolution of the structure factor for a fixed ν (inset in j). Here, $< |F(t)| >_{\phi}$ is shown for $\nu = 0.11\ \mu\text{m}^{-1}$ (indicated by dashed lines in i and j). $t = 0$ is defined by the onset of visible network formation. The keratin concentration was $c_K = 8\ \mu\text{M}$ for all samples. All images are confocal slices. The scale bars denote 20 µm.

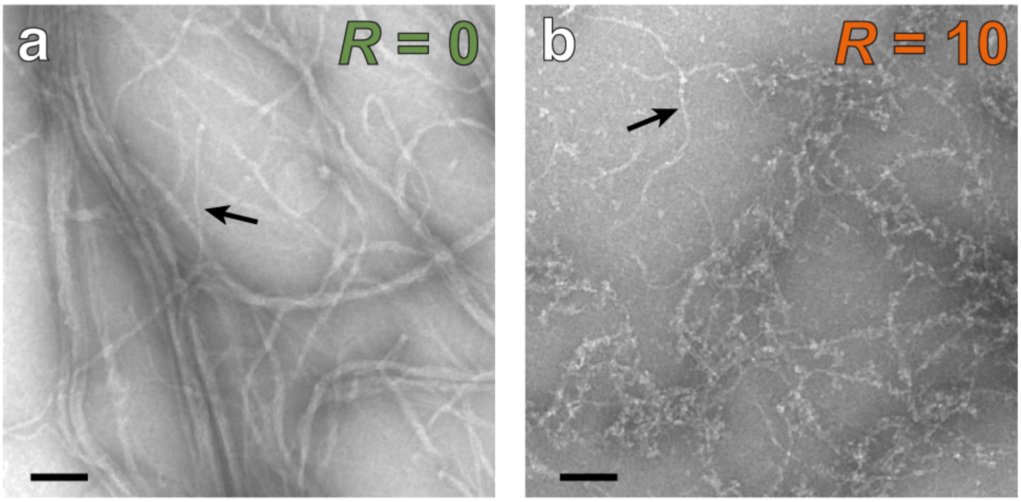

Figure 5.3: Hsp27 inhibits bundling. (a) In a buffer of low ionic strength (3 mM $MgCl_2$) keratin filament interaction is partially hampered and relatively thin bundles are observed via TEM. If Hsp27 ($R = 10$) is present during the assembly, bundles are no longer observed (b). Instead, single filaments, decorated by Hsp27 oligomers, are detected. The black arrows indicate single $\sim$ 10 nm wide filaments. In the absence of salt, no bundles are formed and exclusively single filaments are observed (see Fig. 3.2). The scale bars denote 100 nm.

iniscent of the reported association of αB-crystallin and desmin filaments, critical in the context of desmin-related myopathies (75, 80).

The fast formation of keratin network raises the question of whether Hsp27 already binds to the soluble tetrameric keratin complexes before assembly initiation or if it exclusively interacts with assembled keratin filaments. Analytical ultracentrifugation reveals a pre-assembly association of Hsp27 with soluble K8/K18 tetramers (Fig. 5.4). In this sedimentation velocity assay, only keratin is fluorescently labeled. In the absence of Hsp27 a characteristic tetrameric peak at a sedimentation coefficent of $s \approx 4.6$ S is observed, corroborating reported values (11). The small peaks at approximately 2.5 S and 8 S in the keratin only sample are most likely monomers and octamers, respectively. Upon addition of Hsp27 a drastic decrease of the tetrameric peak can be observes, while a broad substrate peak, indicating a multitude of interaction species, appears at higher s-values (10 S - 30 S). These findings indicate an interaction of keratin and Hsp27 in the pre-assembly phase. This is also supported by FRET measurements (inset in Fig. 5.4). Here, TAMRA-labeled Hsp27 (emission wavelength $\lambda_{\text{em}} = 579$ nm) is showing a FRET signal in the presence of ATTO488-labeled keratin (excitation at $\lambda_{\text{ex}} = 480$ nm, $\lambda_{\text{em}} = 523$). The label is attached to the end

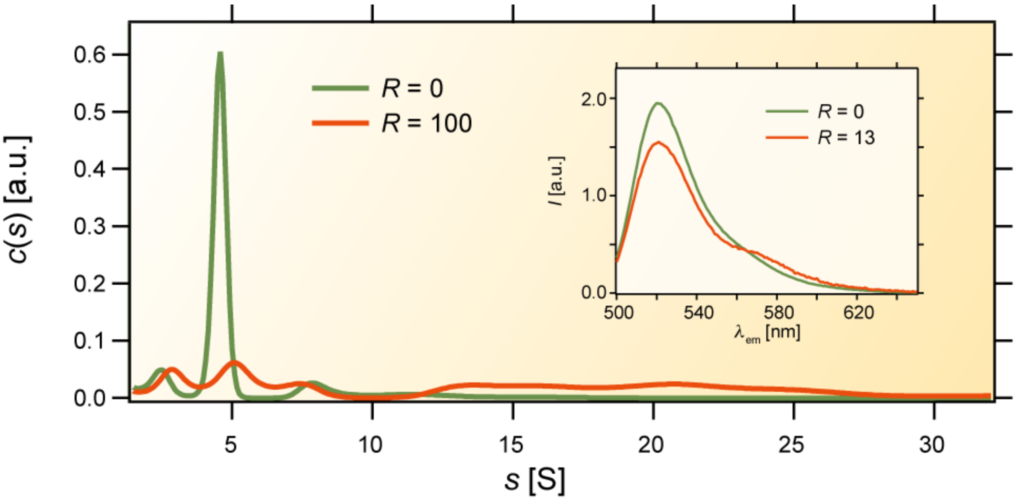

Figure 5.4: Hsp27 interacts with soluble keratin tetramers. Sedimentation velocity analytical ultracentrifugation was carried out for a sample of keratin only (*green*) and a sample containing keratin and Hsp27 (*orange*, $R = 100$). The fluorescence signal of keratin at 647 nm was detected. The strong peak at $s \approx 4.6$ S for the Hsp27 free sample is characteristic for tetrameric complexes. The peaks at s-values of 2.5 S and 8 S most likely correspond to monomeric and octameric forms of keratin. The peak at 5 S diminishes in the presence of Hsp27 and is replaced by a broad substrate peak ranging from 10 S - 30 S indicating multiple interaction species. The inset shows the FRET spectra of ATTO488-labeled keratin (donor, $\lambda_{\text{em}} = 523$ nm) in the absence and presence of TAMRA-labeled Hsp27 (acceptor, $\lambda_{\text{em}} = 579$ nm).

of K8's tail domain, suggesting this to be the location of keratin-Hsp27 interaction.

5.4 SIGNIFICANCE OF THE KERATIN 8 TAIL DOMAIN

To unravel the physical basis for the impact of Hsp27 on keratin network assembly, it is crucial to better understand how both players interact. The bundling capabilities of keratin intermediate filaments have been tentatively attributed to an interaction via their C-terminal tail domains. These unstructured domains protrude from the filament surface and have for certain keratin types been demonstrated to be essential for bundling (48). Therefore, the tail domain of K8, K18 or both might well be of significance for the Hsp27-induced alteration in the keratin network architecture. To investigate the role of the tail domains for the Hsp27-effect we examine mutants of K8 and K18 where the C-terminal domain has been deleted. Here, it should be kept in mind that with a length of 81 amino acids the tail of K8 is almost twice as long as the K18 tail (42 amino acids). Comparing the effect of Hsp27 on the network architecture of tailless mutants

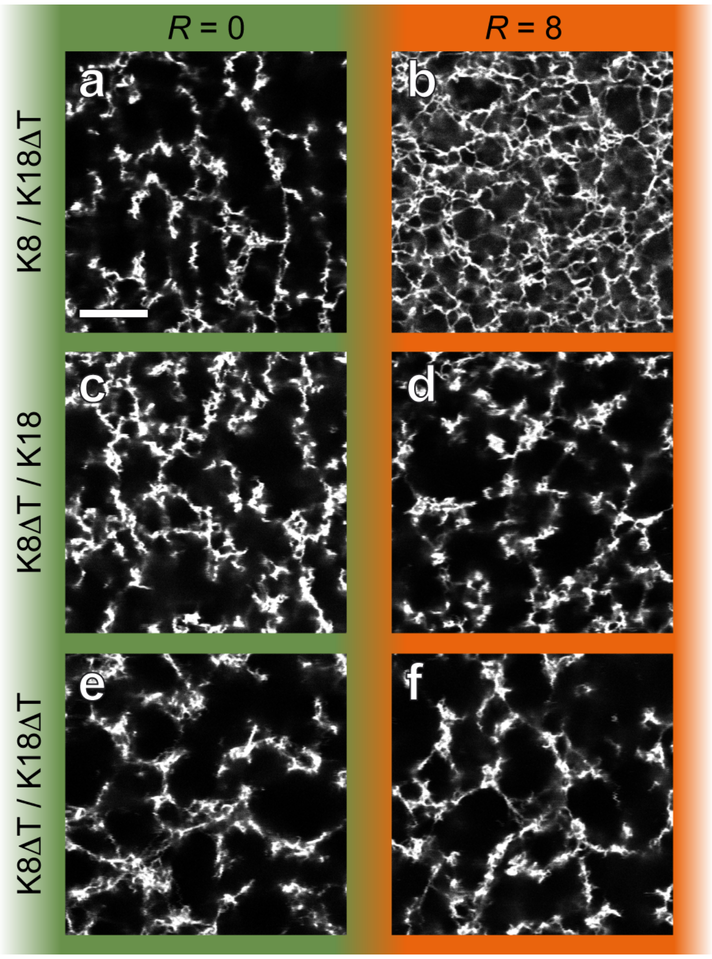

Figure 5.5: The K8 tail is crucial for the Hsp27-effect. Different combinations of wild type proteins and tailless mutants are assessed. The combination of K8/K18ΔT shows the same characteristic increase in fineness as observed for the wild type (a and b). K8ΔT/K18, however, shows no susceptibility to Hsp27 at all (c and d). This also holds true for K8ΔT/K18ΔT (e and f). The keratin concentration was $c_K = 6$ µM for all samples. All images are confocal slices. The scale is the same for all images. The scale bar denotes 10 µm.

(K8ΔT and K18ΔT) with that observed for the wild type confirms the hypothesized relevance of the tail region: While the K18ΔT mutant exhibits an increase in fineness comparable to that of the wild type (Fig. 5.5a and b), the truncation of the K8 tail virtually eliminates the Hsp27-effect (Fig. 5.5c and d). Combining both mutants, so neither K8 nor K18 features a tail domain, also renders the sample insensitive to Hsp27 (Fig. 5.5e and f). Notably, deleting the tails has also an influence on the general network structure in the absence of Hsp27. This observation underlines the notion of the tail domains mediating filament bundling interactions. However, as

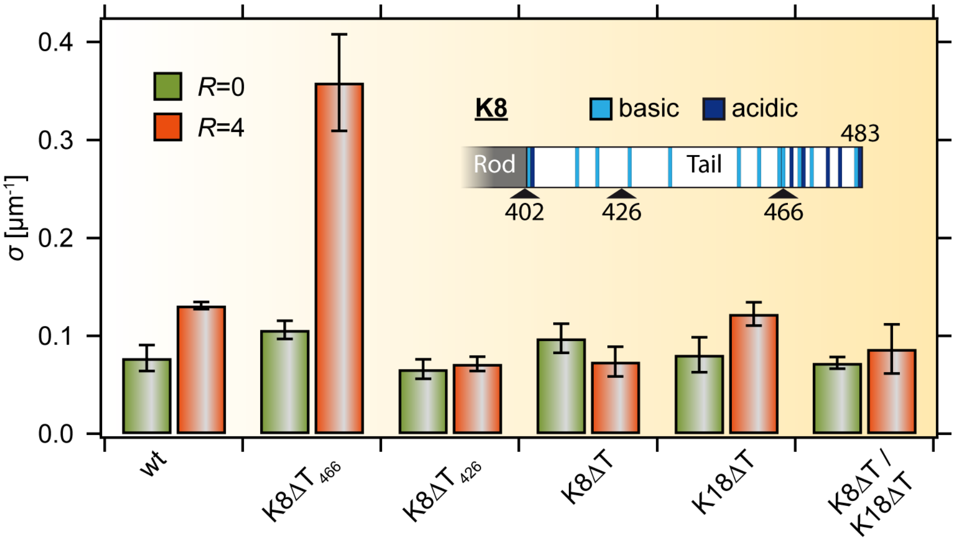

Figure 5.6: Comparison of the Hsp27-effect for different K8 tail configurations. For various tail truncation mutants, as explained in the main text, the fineness σ for $R = 0$ (*green*) and $R = 4$ (*orange*) is shown. Error bars are the standard deviation of data from multiple images acquired at different locations in the sample. The keratin concentration was $c_K = 6$ µM for all samples. For networks of K8ΔT$_{466}$, samples with $R > 4$ exhibit a fineness that exceeds the limits of the evaluation methods, therefore limiting the comparison to low R. The inset depicts the charge distribution of the K8 tail as calculated from the amino acid sequence for pH 7.5. The truncation sites are indicated by black triangles.

bundling is still observed for networks of K8ΔT/K18ΔT, keratins bundling propensity appears more convoluted than tail-mediated attraction alone.

Having established the necessity of K8's tail for Hsp27 to unveil its full impact, we now aim to dissect the tail in a more controlled fashion. Since bundling only occurs in buffers of significant ionic strength, the tails charge distribution might well be an important factor for bundling and keratin-Hsp27 interaction. Especially considering the characteristic charge distribution of K8's tail domain: The C-terminal quarter of the tail features both, acidic and basic amino acids, with an overall negative charge at physiological pH. The rest of the tail is exclusively positively charged (inset Fig. 5.6). Using a series of K8 mutants with partial tail truncations we study the influence of different regions in the K8 tail domain on the effect of Hsp27. With reference to the charge distribution, we truncate the tail after residue 466, eradicating the negatively charged part (K8ΔT$_{466}$, length of the tail reduced to 79% with respect to the wild type). A second mutant (K8ΔT$_{426}$) even reduces the tail to 30% of its original length. Both mutants alter the Hsp27-effect. Surprisingly, the K8ΔT$_{466}$ variant exhibits an even stronger susceptibility to Hsp27 than the wild type. The fineness at $R = 4$ is increased by more than a factor of 3 as opposed to a factor of ≈ 1.7 in case of

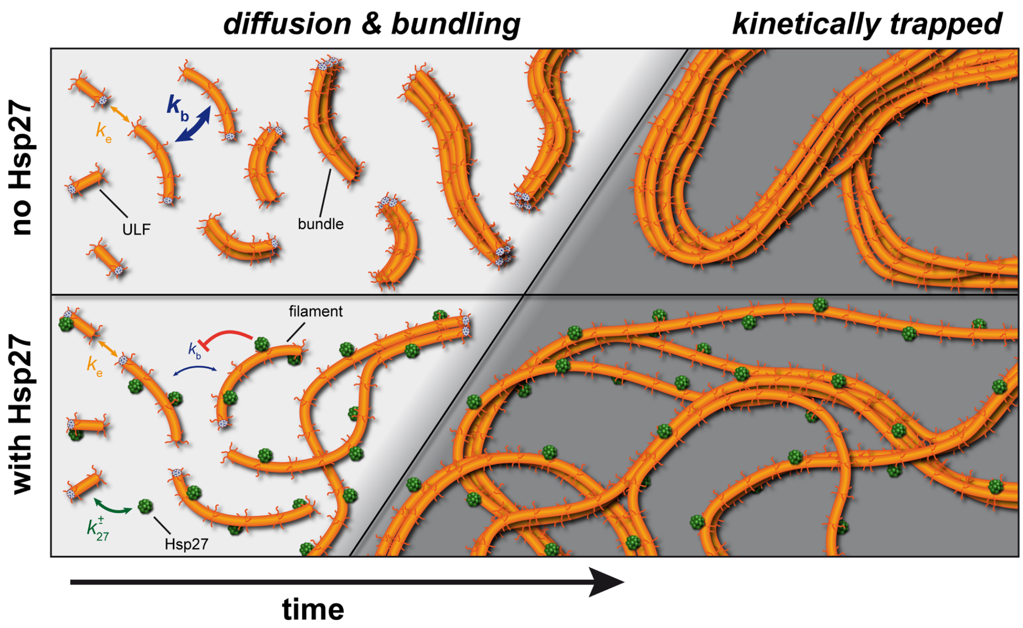

Figure 5.7: Kinetic trapping and Hsp27 influence on keratin network formation. Filaments elongate via the longitudinal annealing of unit length filaments (ULF) with an elongation rate k_e. At the same time, short filaments can diffuse and laterally associate with a bundling rate k_b (*light gray region*). Here, k_e and k_b describe the general kinetics of the associated process and should not be confused with constant interaction rates of the subunits. It is the competition of these two processes, i.e. the ratio of the rates, that determines the onset of kinetic trapping (*dark gray region*) and therefore the final network structure. Binding of Hsp27, dependent on its concentration and the affinity to keratin $k_{27}^{\pm}$, hinders filament bundling (indicated by a red suppression arrow) and results in a finer network, due to an earlier onset of kinetic trapping.

the wild type (Fig. 5.6). K8ΔT426, on the other hand, shows no significant change in fineness, similar to the complete tail truncation.

5.5 HSP27 AND KINETIC TRAPPING

As discussed in chapter 4, a key aspect for the architecture of these network is the competition between filament elongation and lateral association during their formation (Fig. 5.7, *no Hsp27*): In the early stages of assembly, short filaments can diffuse and laterally associate to bundles and clusters of bundles. However, longitudinal growth of filaments and bundles eventually leads to a percolating, quasi-static state of the network where lateral diffusion is suppressed and hence further lateral growth is inhibited. Shifting the balance from lateral to longitudinal growth therefore leads to an earlier onset of this kinetic trapping and consequently a finer network structure. We argue, that this concept is the basis for the impact of Hsp27 on the keratin network structure and that the results presented here, assuming only one mode of lateral filament and bundle interaction on all length scales, converge towards one scenario (Fig. 5.7, *with Hsp27*): Hsp27 associates with keratin in a pre-filamentous state, as verified by analytical ultracentrifugation (Fig. 5.4). This leads to an inhibition of lateral association of nascent filaments in the early phase of assembly, hampering bundle formation and thereby amplifying the dominance of longitudinal elongation as the favored mode of growth. As a result, a kinetically trapped state is reached much earlier and further coarsening is inhibited (Fig. 5.2). The decrease of the bundling rate, and with it the strength of the effect, directly depends on the amount of Hsp27 bound and hence on R (Fig. 5.1). Our data furthermore shows the tail of keratin 8 to be essential for the observed increase in network fineness (Fig. 5.5). Deleting the negatively charged C-terminal part of the tail drastically enhances the effect, suggesting that electrostatics play an important role in keratin-Hsp27 interaction (Fig. 5.6). Considering the overall negative charge of Hsp27 at the given buffer conditions, we speculate that electrostatic repulsion of the negatively charged distal part, in conjunction with steric hinderance, partially diminishes the attraction towards the positively charged proximal region of the tail.

5.6 CONCLUSION

This study presents evidence for a potential regulatory role of Hsp27 for the keratin cytoskeleton. Interestingly, it is not only the influence of the associated protein but the non-equilibrium nature of the network itself that is at the heart of this effect. Kinetic trapping has also been reported for reconstituted actin bundle networks, underlining the significance of such mechanisms for the formation of cytoskeletal networks (14, 15, 88). Thus, the next steps will be towards a combination of reconstituted actin and keratin networks to investigate the role of kinetic trapping in such cytoskeletal composite systems.

6

COMPOSITE NETWORKS OF KERATIN AND ACTIN

While recent years have proven *in vitro* model systems to be an essential tool to deepen our understanding of the cytoskeleton, most work has focused on only one cytoskeletal subsystem. Having established a well controlled keratin model system, we can now take the next step towards increased complexity: composite networks of keratin and actin bundles. While this will not nearly mimic the full intricacy exhibited by the cytoskeleton of a living cell, it can serve to assess potential emergent behavior and understand the underlying physical principles. This chapter will discuss initial investigations in this direction.

6.1 FIRST STEPS TOWARDS A COMPOSITE SYSTEM

To establish a two-component network, one first has to find buffer conditions that are equally suitable for both subsystems. During the development of the keratin model system, the eventual incorporation into a composite network has always been considered. Therefore, buffer conditions where chosen such that they are compatible with those necessary for actin. The salt concentrations used for keratin assembly are identical with those conventionally used for actin based assays. Also the pH of ~ 7.5 at room temperature is in a range typically used in such experiments. Thus, the keratin system presented in the previous chapters is ideally suited to be supplemented by an actin bundle system to investigate the interplay of both networks.

Another factor are the buffer conditions the proteins experience prior to assembly initiation. Since keratin will undergo filament formation in standard actin G-buffer, due to the low pH and the presence of salt, low-tris buffer - routinely used for keratin assembly - was employed for protein dilution during sample preparation. The traces of introduced G-Buffer in the sample were sufficiently small to prevent premature keratin assembly. Equally important, actin network formation did not seem to be significantly influenced by temporarily subjecting the actin monomers to low-tris buffer conditions prior to assembly. Thus, actin could be included in the droplet-fusion technique, formerly introduced for keratin network formation.

Having established a robust protocol for the co-formation of keratin and actin networks we can now aim to unravel the intricacies of this composite system. Here, the influence on the formation dynamics of both networks are of great interest, especially in the light of kinetic trapping. In general, such interdependencies are directly connected with a high degree of dynamic complexity, as the impact of one system on the other can feed back on itself. Fortunately, in the keratin/actin system, the assembly time scales of the two networks differ significantly. While keratin networks form in the matter of seconds (see chapter 4), actin bundle networks need several minutes to one hour to fully assemble(15). This temporal separation yields an important experimental advantage: On the one hand, the building of the keratin network is not impacted by the presence of, yet mostly non-filamentous, actin. When, on the other hand, actin polymerization and bundling enters the scene, it is confronted with a ready formed keratin scaffold. This reduction in dynamic complexity allows for a carefully controlled study of the impact of a keratin scaffold on the formation of actin bundle networks (89).

There are several crosslinking molecules that bundle actin. The formation dynamics and morphology of such networks directly depends on the present crosslinker. α-actinin, for example, produces large arrays of curved bundles of varying diameter that merge in and out of each other(14). Similar to keratin, the structure of actin/α-actinin networks is a direct result of their assembly dynamics and kinetic trapping(15). Fascin, another actin bundling protein, organizes actin filaments into rather straight filaments of a defined diameter of ~ 30 nm(90). The self-limited growth of actin/fascin bundles renders them less susceptible to the effects of kinetic trapping under single network conditions. In this chapter we will investigate the impact of a keratin scaffold on actin bundle networks, crosslinked by either α-actinin or fascin.

6.2 IMPACT OF A KERATIN SCAFFOLD ON ACTIN BUNDLE NETWORKS

First, we turn towards a composite system of keratin and actin/α-actinin networks, where we expect an impact of the keratin network due to the kinetically trapped nature of the actin component. At a relatively high keratin concentration ($c_K = 15$ µM) a dense and homogeneous network is produced (Fig. 6.1a). The ensuing actin/α-actinin bundle network, with an actin concentration of $c_A = 3$ µM and a molar ratio of α-actinin to actin of $R = 1$, exhibits a similar degree of homogeneity (Fig. 6.1b and c). As

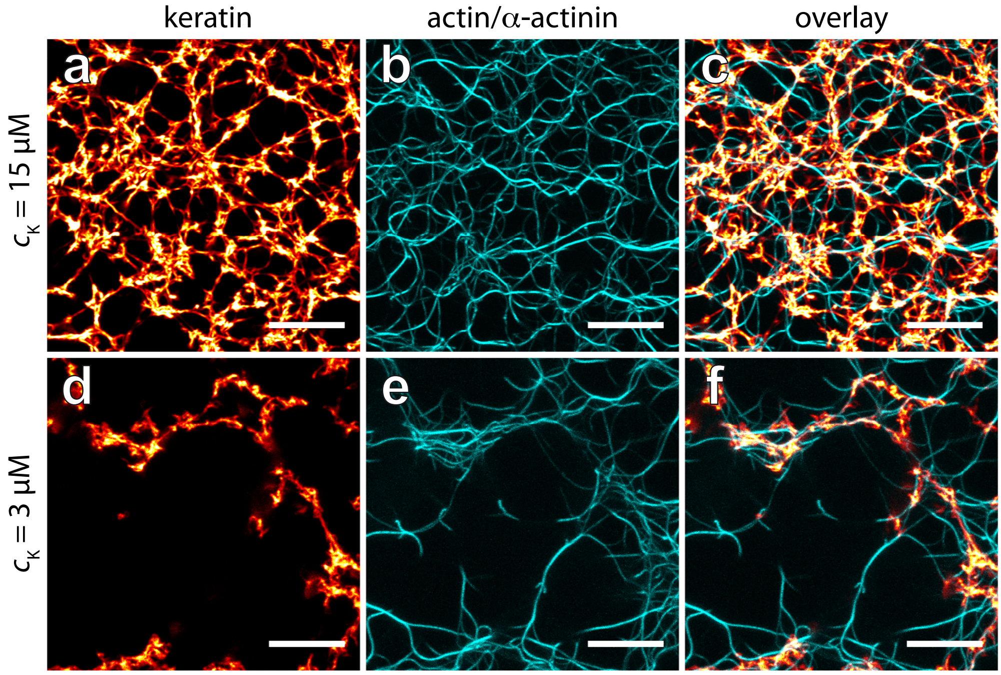

Figure 6.1: A keratin scaffold influences the structure of actin/α-actinin bundle networks. At high keratin concentrations ($c_K = 15$ µM) a dense keratin meshwork is formed (a and c). An ensuing actin bundle network ($c_A = 3$ µM and $R = 1$) exhibits a comparable fineness (b and c). If the keratin concentration is lowered to $c_K = 3$ µM - and hence a much coarser scaffold is produced - the actin network follows this trend, even though the actin and α-actinin concentration are kept constant (d-f). It moreover seems to colocalize with the keratin structures (f). Scale bars denote 10 µm. See Fig. 6.2 for a quantitative analysis.

discussed in chapter 4, reducing the keratin concentration to $c_K = 3$ µM results in a significant increase in the scaffold's mesh size (Fig 6.1d). Interestingly, if such a coarser scaffold is presented to the same actin/ α-actinin composition discussed above ($c_A = 3$ µM and $R = 1$ remain unchanged), the resulting structure of the actin bundle network is drastically altered (Fig. 6.1e). It appears to follow the general structure of the keratin scaffold, leaving keratin free areas also relatively void. Furthermore, a divergence of network substructure can be observed. While scaffold-free regions are dominated by single long filaments of high fluorescence intensity, areas adjacent to keratin structures exhibit a fine meshwork of thin actin bundles.

Evaluating a range of different keratin scaffold mesh sizes ξ_K reveals a continuos trend in the resulting characteristic mesh size ξ_A of the actin bundle network (Fig. 6.2a). Here, increasing the keratin mesh size results in a monotonic coarsening of the actin bundle network with $\xi_A < \xi_K$ at

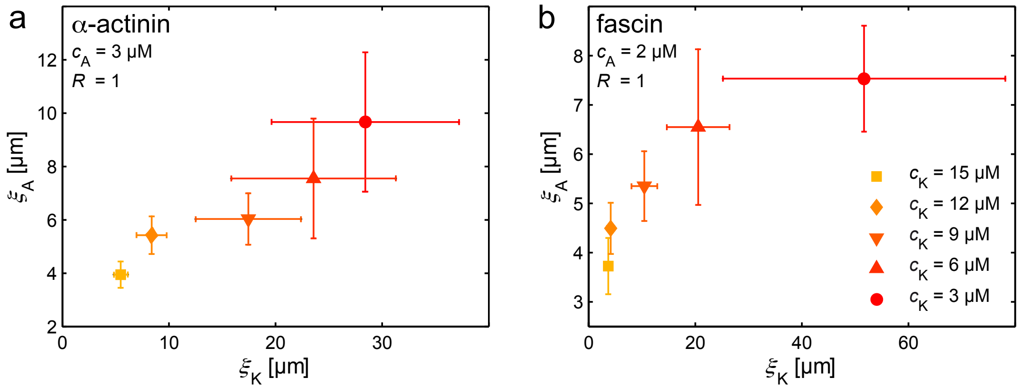

Figure 6.2: Relationship between mesh sizes of keratin and bundled actin networks. The characteristic mesh size ξ_A of an actin/α-actinin (a) and a actin/fascin bundle network (b) are plotted against the characteristic mesh size ξ_K of the corresponding keratin scaffold. The error bars denote the standard deviation of images obtained at different positions throughout the sample, giving a measure of the overall heterogeneity of the networks. Marker color and shape refer to different keratin concentrations as indicated by the legend in (b). Actin concentration was $c_A = 3$ μM and $R = 1$ for all samples.

all times. While the increase in ξ_A appears fairly linear, ξ_A always remains significantly smaller than ξ_K, reflecting the fine actin bundle meshwork close to keratin structures. The larger error bars associated with large mesh sizes indicate the increased degree of heterogeneity in coarse networks.

These results suggest a significant influence of the preexisting keratin network on the formation of biochemically identical actin/α-actinin bundle networks. Again, the concept of kinetic trapping might be the key element to understand the observed behavior. We know that it plays an important role in the formation of actin/α-actinin networks in the absence of keratin(15). One therefore might envision a scenario where the keratin scaffold sterically hinders the lateral diffusion of elongated filaments and therefore their continuos association to bundles. The observed fine actin bundle meshwork in regions with a keratin scaffold supports this notion. In the samples with low keratin concentration there are large areas without a scaffold. Here, nascent actin filaments and small bundles can freely diffuse. Actin structures that are connected to the scaffold, however, are held in place. As a consequence, freely diffusing actin bundles connect to these static structures, causing an accumulation of actin bundles around keratin-rich regions.

Due to the presence of keratin structures a quasi-static, kinetically trapped state of the network is reach before extended actin filament bundling can occur. This is similar to the concept of kinetic trapping on non-composite keratin or actin bundle networks introduced before. However, the microscopic mechanisms altering the onset of kinetic trapping are different. In the described cases of non-composite system it is the change of elongation or bundling propensity that causes the alteration of the network structure. This can, for example in the case of actin/α-actinin networks, be achieved by either varying the amount of polymerization seeds present in the solution or the addition of polymerization-altering associated proteins(15, 88). In chapter 5, the impact of Hsp27 on the keratin network morphology was described, where the small heat shock protein decreases the inherent bundling propensity of keratin filaments. In both cases, the primary effect is an alteration of the ratio of filament elongation to bundling. Only as a secondary effect, when bundle extension leads to a percolating network, is the diffusion of bundles and therefore their lateral growth affected. This is different in the case of composite networks. Here, the keratin scaffold acts as a selective inhibitor of bundle diffusion, holding larger structures in place while allowing for diffusion of monomers and smaller filaments.

Next, the influence of a keratin network on a very different actin bundle network will be investigated. Since actin bundles induced by the bundling protein fascin are not only very stiff but also exhibit an equilibrium bundle thickness of approximately 20 single filaments, they are commonly not associated with kinetic trapping(90). It therefore is surprising that a preformed keratin scaffold, like in the case of the actin/α-actinin system, has a definite effect on the architecture of actin/fascin bundle networks. Fig. 6.3 compares two keratin-actin/fascin composite networks. Each features an actin concentration of $c_A = 2$ µM and a ratio of fascin to actin of $R = 1$. Keratin concentration is varied from 15 µM (a-c) to 3 µM (d-f). The actin/fascin bundles in the sample with a dense keratin scaffold generally appear more homogeneously distributed and thinner. Some of them are even curved or bent (arrows in Fig. 6.3 b). The coarser scaffold results in thicker (brighter) and much more straight bundles, similar to those observed in scaffold-free samples. However, their arrangement is clearly influence by the keratin scaffold, exhibiting an increased density in the neighborhood of keratin structures. Again, evaluating the mesh size ξ_A of the actin bundle network as a function of the keratin mesh size ξ_K reveals a monotonic increase of ξ_A with growing ξ_K (Fig. 6.2b). Yet, here the slope of the curve levels of for very coarse scaffolds. This concurs with the limited growth of actin/fascin bundles. If the characteristic length scale of the keratin network surpasses that of a native actin/fascin bundle network, the latter becomes independent of the keratin scaffold. This is in stark contrast to actin/α-actinin

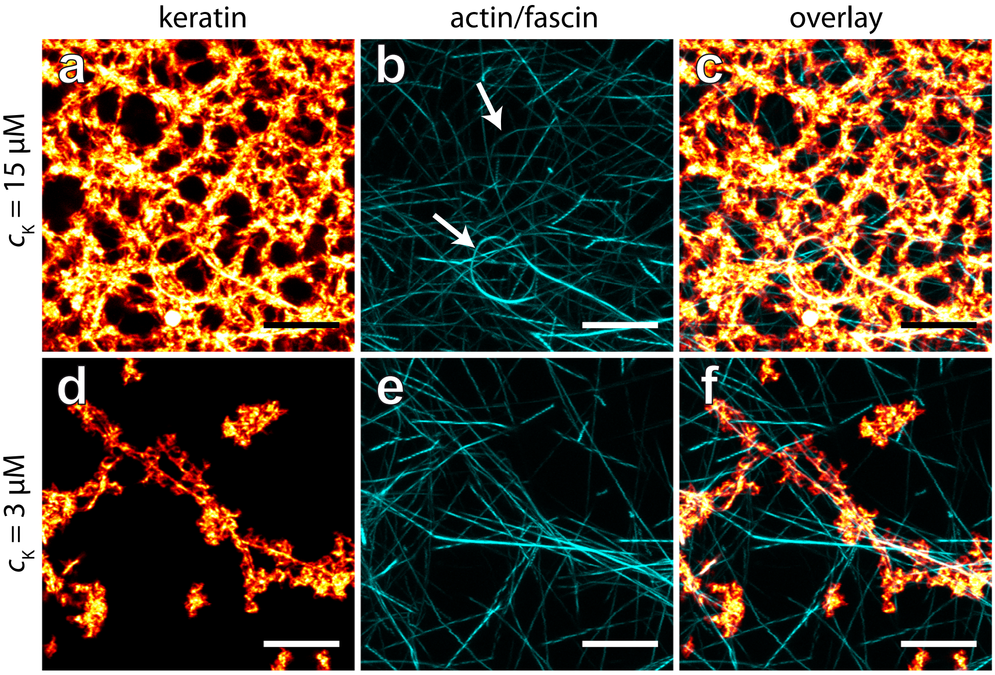

Figure 6.3: A keratin scaffold influences the structure of actin actin/fascin bundle networks. At high keratin concentrations ($c_K = 15$ µM) a dense keratin meshwork is formed (a and c). Similar to the case of α-actinin (Fig. 6.1), the resulting actin bundle network ($c_A = 2$ µM and $R = 1$) exhibits a high fineness (b and c). If the keratin concentration is lowered to $c_K = 3$ µM, the actin network (c_A and R are kept constant) again shows a decrease in fineness (d-f). Interestingly, curved bundles (white arrows in (b)) are observed only in the case of a dense keratin scaffold. Scale bars denote 10 µm. See Fig. 6.2 for a quantitative analysis.

networks, where bundle growth will continue until kinetic trapping sets in, resulting in a much higher native mesh size.

The two examples of α-actinin and fascin bundle networks in combination with a keratin scaffold demonstrate the influence of the composite nature of these systems on their assembly dynamics and structure. The next step will be to investigate the behavior of keratin/actin composite networks under a mechanical load.

6.3 COMPOSITE NETWORKS UNDER SHEAR

The introduced keratin/actin composite networks provides the means to investigate potential emergent properties of such systems under load. However, to apply a shear strain, the relative movement of opposing sides of the network is required. One can easily envision a setup where two cover

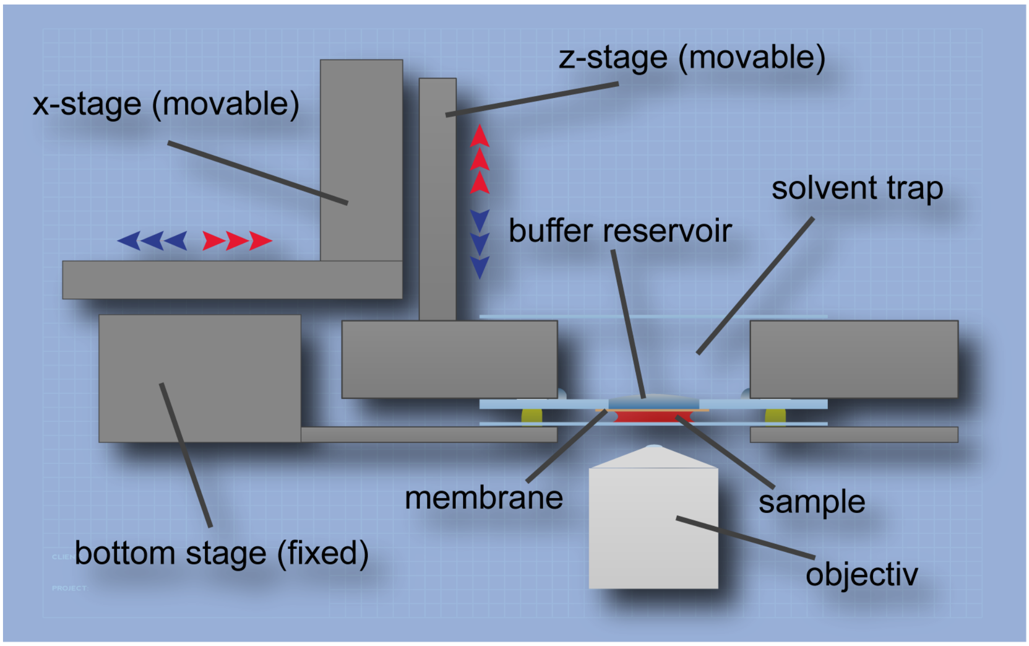

Figure 6.4: Design of a shearable diffusion chamber. The schematic depicts the principle design of the setup, including a diffusion chamber composed of a membrane, buffer reservoir and solvent trap, for the *in situ* assembly of percolating composite networks. The upper stage (x-stage and z-stage) can be moved relative to the static bottom stage by a computer controlled actuator (see chapter 2 for details). The z-stage can be alternatively positioned by either a micrometer screw (coarse) or a piezo (fine). The entire setup can be placed on a conventional confocal microscope for fluorescence imaging.

slips, acting as sample boundaries, are moved relative to each other in a controlled fashion to apply shear to the network. Here, the droplet-fusion method, as useful as it proved to be for studying unloaded networks, however, does not suffice. At the side of salt introduction, a network is formed in the contact region of both droplets before proteins can diffuse through the assembly buffer to the surface. This results in a small gap between surface and network. This lack of total percolation excludes shearing the network by relatively moving the two glass cover slips. Hence, a novel approach has to be pursued to ensure network percolation from one boundary to the other while maintaining the principles of flow inhibition featured in the droplet-fusion technique. Furthermore, compatibility with a confocal microscope has to be ensured for proper imaging. To this end, a shearable diffusion chamber is designed (Fig. 6.4). Here, one cover slip is replaced by a cellulose membrane (0.1 μm pore size), coupling the sample to a buffer reservoir on top. The reservoir can then be filled with assembly buffer before the membrane is carefully lowered onto a droplet of protein solution, placed on an opposing glass cover slip mounted on the bottom stage of the assembly. Ions can then freely diffuse through the membrane into the sample volume while the network is stabilized by the membrane on one side and the cover slip on the other. In this manner, we can produce a composite network, percolating throughout the entire sample volume. The setup can be mounted onto a conventional confocal microscope for imaging. To apply shear, the entire upper stage, including the membrane and the reservoir, can be moved by a computer controlled step motor.

To investigate the performance of different network compositions under load, initial results of pure keratin and keratin/actin composite networks will be discussed in the following. This will also as a verification of the involved experimental techniques and applied methods of analysis. Increasing the shear deformation in a stepwise manner with confocal z-stacks between steps allows for a precise acquisition of the networks response to shear (Fig. 6.5 a,b). In this manner, gradual deformation to a maximum deflection of 200 μm of the movable stage is performed. Subsequently, the deformation is traced back until the initial position is reached. This cycle can then be repeated to evaluate the potential impact of multiple deformation cycles. To quantify the strain field, the y-projection of the recorded stacks is divided into z-bands of equal width at different heights above the bottom surface. The displacement in these bands can then be tracked by digital image analysis (see inset in Fig. 6.5 c and section 2 for details). Fig. 6.5c shows the additional deformation per step of a keratin network for different heights above the static surface. This network exhibits the expected rectangular shaped strain profile. The composite network, however, shows a drastically different behavior: While the first shearing still results in a relatively rectangular profile, the reversed phase already has a much more complex response (Fig. 6.5 d). At a certain strain ($\sim$ 40% of the maximum) further movement of the network is significantly hampered, followed by a series of large deformations. This double-peaked profile is mirrored in the following load cycle, with decreased strain near the relaxed position. Interestingly, the profile of the first cycle is always differs from the subsequent cycles, especially in the case of composite networks, suggesting network rearrangements during initial shearing. Such a complex behavior can only be rationalized with a non-linear deformation profile on the scale of the entire sample. This is unexpected, since a homogeneous sample, even if it exhibits non-linear rheological properties, should follow a linear deformation profile. The behavior observed here is therefore either due to (introduced) inhomogeneities in the sample or the influence of surface coupling. Unfortunately, the current setup does not yet allow for a sample height small enough to image the entire gap. In the imaged region, the total displacement of the network at the maximum deformation scales perfectly linearly

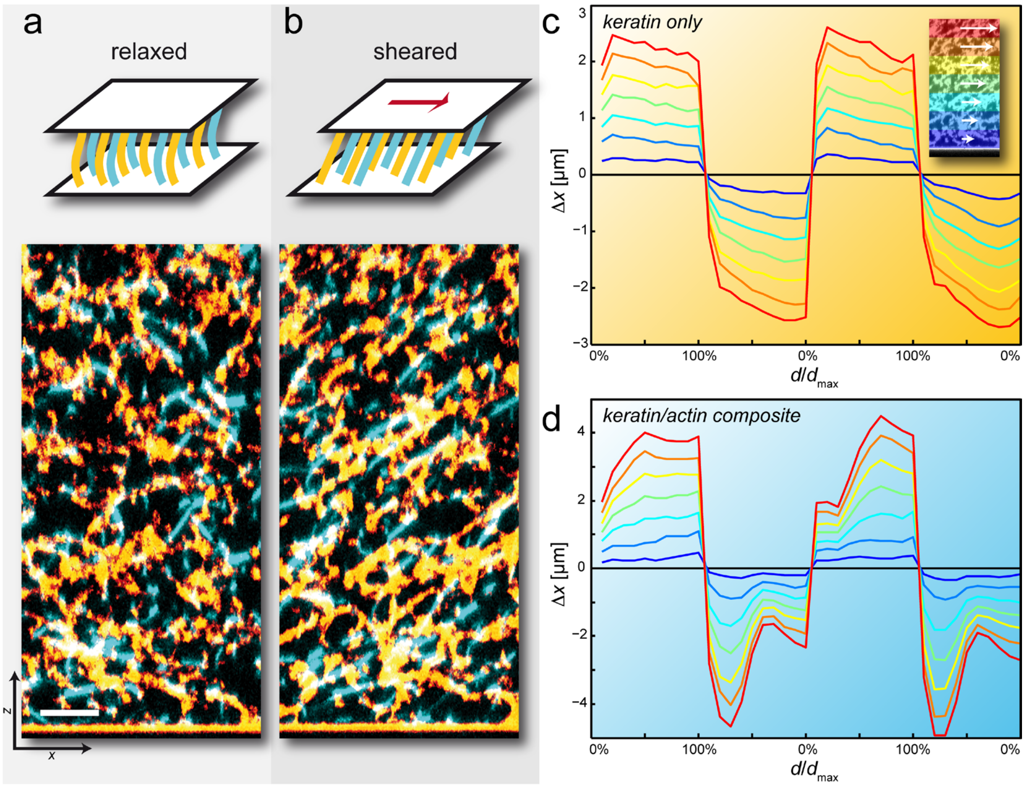

Figure 6.5: Analysis of networks under shear. Confocal stacks of a composite network in the shear chamber are processed and depicted as maximum intensity y-projections in a relaxed (a) and a sheared (b) configuration. The displacement of a keratin (c) and a keratin/actin composite network (d) at different heights above the surface is tracked for. Networks are sheared in a step-wise manner. To quantify the general form of the networks responses, the step-to-step displacement of each network, Δx, is evaluated as a function of normalized displacement of the movable stage, $d/d_{\max}$. Δx is displayed for several z-bands at different heights above the surface (indicated by the colors referring to the inset in (c); width of each band $\approx$ 10 µm). The scale bar represents 10 µm.

with the distance from the surface (Fig.6.6a). We will focus on this region for the following evaluation. Hence it is more adequate to consider the upper boundary of the imaged volume as reference and force conducting plane. By this means, all contributions of non-imaged parts of the network are neglected. Similarly, the lowest z-band is defined as bottom reference to correct for any drift of the cover slip. The applied shear strain can now be defined as $\hat{\gamma} = \hat{x}/\hat{z}$, where $\hat{x}$ is the total displacement of the highest band in the imaged region relative to the lowest band and $\hat{z}$ is the distance between both. Applying this concept allows for a more suitable representation of the network displacement. Fig. 6.6b and c show the displacement x as a function of the cumulative applied strain $|\hat{\gamma}|$ for different z-bands. Here, $|\hat{\gamma}|$ is simply the sign independent sum of all applied strain steps and

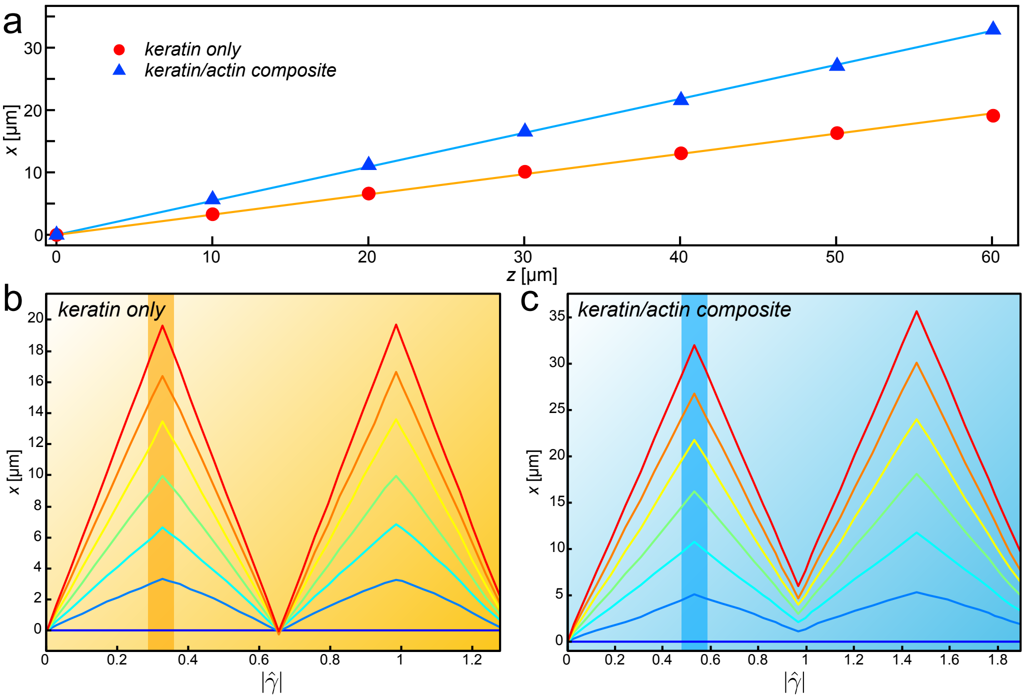

Figure 6.6: Displacement as a function of distance to the surface and strain. (a) The absolute displacement of the network, x, scales linear with the distance from the surface, z. The displacement after N deformation steps is calculated as $x_i = \sum_{n=1}^{N}(\Delta x_{n,i} - \Delta x_{n,1})$, where $\Delta x_{n,i}$ is the frame-to-frame displacements associated with the n-th deformation. i indexes the z-bands, starting with the lowest, and z corresponds to the distance of each band center from the surface. The displacement of the band closest to the surface ($i = 1$) is used as static reference to subtract any potential drift of the surface during data acquisition. For both, pure keratin and composite networks, the displacement of the network in the maximally sheared configuration ($n = 10, d = 200$ µm) is plotted as a function of distance to the lower surface. Both cases reveal a strong linear dependence (solid lines are linear fits to the data). Panels (b) and (c) show the absolute displacement x in relation to the initial position in different z-bands as a function of cumulative strain $|\hat{\gamma}|$ for a keratin and a keratin/actin composite network. The associated cumulative strain is defined as $|\hat{\gamma}| = (\sum_{n=1}^{N} |\Delta\hat{x}_n - \Delta x_{n,1}|)/\hat{z}$, with $\Delta\hat{x}_n$ being the frame-to-frame displacement of the top band and $\hat{z}$ it's height above the lowest band. Different z-bands are indicated by color (blue to red with increasing z; width of bands approx. 10 µm). The highlighted areas in (b) and (c) indicate the data points corresponding to those in (a).

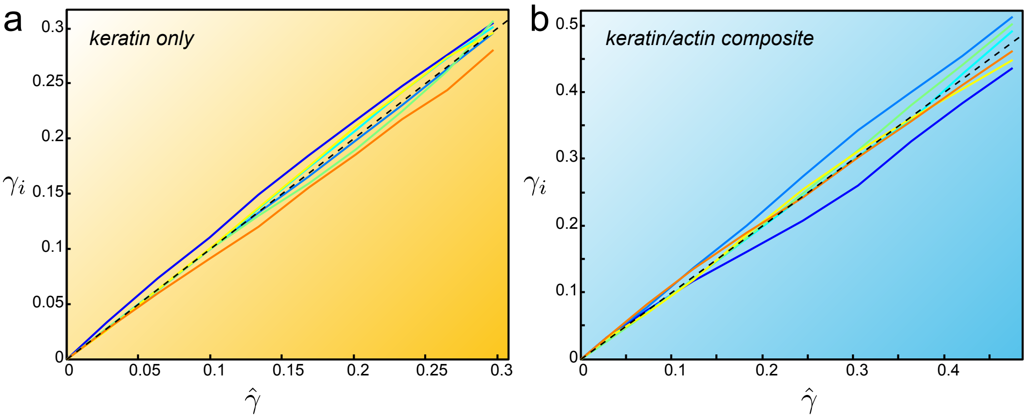

Figure 6.7: Relation between applied and local shear. The local strain γ_i as a function of applied strain $\hat{\gamma}$ of a keratin (a) and a keratin/actin composite networks (b) are depicted for different z-bands, as indicated by color (blue to red for increasing z). The dashed black line represents a slope of unity. Shown is the first shear from the initial position to maximum deformation.

serves as a monotonically increasing coordinate (see figure caption). For all bands, the deformation increases/decreases linearly with $|\hat{\gamma}|$, indicative of uniform deformation throughout the cycle. The slight offset in Fig. 6.6 after the first cycle results from an incomplete return of the upper band to its initial position, due to irreversible contributions outside the observed region. Having established the validity of the applied strain, we can now investigate the local response of the network. Similar to the applied strain, the local strain can be calculated as the the ratio of the relative displacement in two neighboring bands and their distance in z, $\gamma_i = \frac{x_{i+1}-x_i}{z_{i+1}-z_i}$. The relation of applied and local shear can then be used to ascertain the uniformity of the network's response to the deformation. For keratin and keratin/actin composite networks, both networks exhibit relatively uniform behavior in the investigated regime, (Fig. 6.7). Here, the local strain γ_i almost equals the the applied strain $\hat{\gamma}$ for all deformation, as indicated by a slope of unity. The above results show that, while there are non-linear contributions - possibly due to sample inhomogeneities or incomplete surface coupling - on the scale of the entire sample (Fig. 6.5), the actual linear behavior of the sample in the observed region can be recovered by applying appropriate corrections based on the acquired displacement data (Figs. 6.6 and 6.7).

6.4 CONCLUSION

Presenting actin bundling networks with a keratin scaffold during assembly demonstrated how strongly the presence of one network can effect the behavior of the other. This illustrates how important it is to consider the composite nature of the cytoskeleton when employing model systems for its investigation. While one has to be aware of a certain degree of spacial segregation of both systems *in vivo*, it is also clear that there are several situation where the presence of the accompanying network cannot be neglected. Examples are the formation of stress fibers and the actin dependent transportation of nascent keratin filaments from the cell periphery and their incorporation into the keratin cytoskeleton(51). The initial data of sheared networks confirm a linear deformation field for all networks at low strains in the observed region. While these results alone do not yet reveal any emergent behavior of keratin/actin composite networks to shear in the range of the applied magnitudes, they demonstrate that the presented experimental approach is feasible. They furthermore validate the analysis process and the ability to correct for artifacts. The presented data therefore lays the foundation for the continued investigation of such complex networks, including imaging across the entire sample width and larger strain amplitudes up to structural failure of the network. It is here, in the propagation of defects, where the impact of composite aspects is most evident for other composite systems(91, 92). Eventually, only the combination of the introduced experiments with rheological assays will yield a complete picture of the interplay between structure and mechanics of such complex systems.

So far we have focused on the non-equilibrium aspects of network formation. However, the quasi static nature of these system directly entailis potential dynamics on very long timescales as they are frequently observed in soft glassy materials (93).

7

SLOW RELAXATION DYNAMICS

This chapter will discuss the implications of non-equilibrium characteristics of cytoskeletal networks for their behavior on long time scales. Reconstituted actin networks have been extensively studied not only as a model system for the cytoskeleton, but also to understand the interplay between microscopic structure and macroscopic viscoelastic properties of network-forming soft materials. These constitute a broad class of materials with countless applications in science and industry. In this chapter, we show that fully polymerized actin/fascin bundle networks display surprising age-dependent changes in their viscoelastic properties and spontaneous dynamics, a feature strongly reminiscent of out-of-equilibrium, or glassy, soft materials. Using a combination of rheology, confocal microscopy and space-resolved dynamic light scattering, we demonstrate that actin/fascin networks build up stress during their formation and then slowly relax towards equilibrium due to the unbinding dynamics of the crosslinking molecules. This process is closely related, yet not identical to the kinetic trapping discussed before.

7.1 ACTIN NETWORKS AS A MODEL SYSTEM FOR SOFT GLASSY MATERIALS

Actin filaments can be associated with a variety of different crosslinking proteins such as fascin, espin, α-actinin or filamin, each creating a network with specific properties(94). The dynamic build-up and reorganization of these different network types allows cells to adjust their mechanical properties according to their needs. A detailed knowledge of the microscopic processes and dynamic rearrangements occurring in the cytoskeleton is difficult to acquire but of high importance for extending our understanding of cell mechanics. So far, soft glassy rheology (SGR) approaches have been used to describe the complex mechanical behavior of living cells(95–97). In SGR, a system evolves in a complex energy landscape with a high number of local minima, or traps. The typical depth of these traps is much larger than the thermal energy, $k_B T$, so that the temporal evolution in this energy landscape requires a form of activation energy, modeled by introducing a "noise" or "effective temperature". The microscopic origin of this activation energy, however, is still unclear. An appealing candidate is given by internal stresses triggering local rearrangement events. Indeed, internal stress relaxation has been invoked to explain the spontaneous dynamics of a variety of soft glassy and biological materials, although no direct evidence of the role or even the very existence of internal stress fields could be provided(93, 98–101).

For a more detailed understanding of soft glassy materials, model systems are required where the observed dynamics can be related to the network constituents and their rearrangements. Actin/fascin bundle networks represent such a model system with a viscoelastic response that can be rationalized on a microscopic level(1, 2, 102). This is mainly due to the clean and simple microstructure of these networks: above a critical concentration, fascin organizes actin filaments into a network of stiff bundles with well-defined diameters as they are for example found in filopodial structures. Thus, actin networks provide a unique opportunity to shed light on the mechanical properties of cells as well as on the microscopic mechanisms shaping the aging dynamics of soft glassy materials. Here, we show that actin bundle networks formed by fascin show complex behavior in their viscoelastic and dynamic properties, i.e. an alteration of their frequency response and a slow-down in their spontaneous relaxation dynamics with increasing sample age. Our experiments show that internal stress is stored during the formation of actin/fascin bundle networks and that the complex dynamics of the networks is due to unbinding events of transient crosslinks between distinct actin bundles. These unbinding events release stress in the network, which approaches a stationary state over time, i.e. within $\sim$10 hours. Control experiments where the binding kinetics of the actin/fascin bonds is altered confirm this scenario.

7.2 EVOLUTION OF MECHANICAL PROPERTIES ON LONG TIME SCALES

Above a critical concentration ratio of $R = \frac{c_{\text{fascin}}}{c_{\text{actin}}} = 0.01$, fascin organizes actin filaments into a network of crosslinked bundles(102). This organization process can be followed in time by rheology: as soon as polymerization is initiated, the elastic modulus $G'(f)$ of an actin/fascin solution with e.g. $R = 0.1$ fascin starts to increase due to the polymerization of actin filaments as well as the formation of bundles and interconnecting crosslinks. The maximum elasticity is reached within 1 hour and subsequent rheological measurements are commonly completed within the following 30 min-

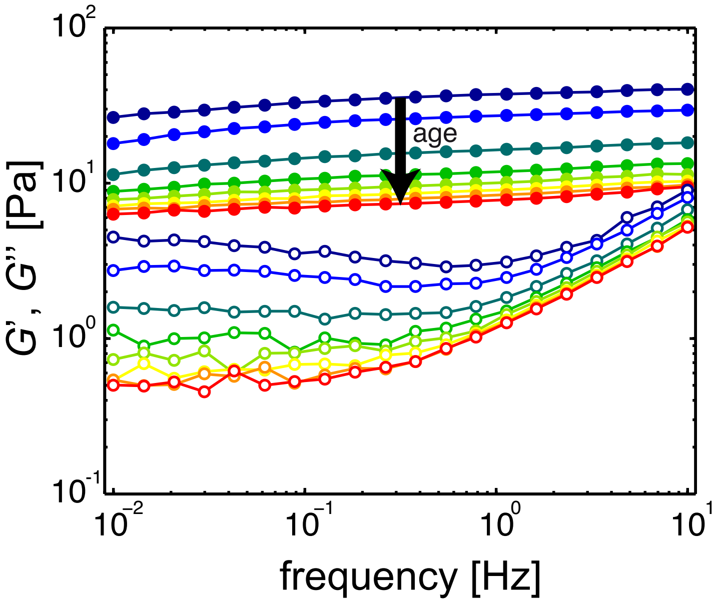

Figure 7.1: The frequency dependent viscoelastic response of an actin/fascin bundle network changes with increasing sample age. Closed symbols denote the storage modulus G', open symbols represent the loss modulus G''. The sample age ranges from 0 h (blue) to 9 h (dark red). Frequency spectra are taken in intervals of 1.3 h. The actin concentration is $c_a = 9.5\ \mu\text{M}$ and the ratio of fascin to actin is $R = 0.1$.

utes. On the typical time scale of these experiments no relevant changes in the viscoelastic moduli are detectable. However, on longer time scales the viscoelastic properties of the network do evolve: Our first observation is that the network elasticity $G_0 := G'(10\ \text{mHz})$ significantly decreases over the course of several hours (Fig. 7.1 and Fig. 7.5d). This is in contrast to the aging process of most glasses or soft glassy materials, where an increase in the material elasticity is observed with increasing sample age, t_w(103–107). Yet, a decrease of G_0 with t_w has been observed in closely packed soft spheres(108, 109), a soft glassy material, where it has been tentatively attributed to internal stress relaxation. For our actin/fascin network, the decrease of elasticity slows down over time and after ~ 10 h G_0 seems to approach a constant value which is approximately five times lower than the initial network elasticity. This asymptotic behavior is at odds with predictions from the original SGR model, where the effective temperature is assumed to be constant in time(95). However, it was already recognized that the effective temperature may change with t_w, leading to a more complex evolution of the viscoelastic moduli.

As a second observation, we also note a significant change in the loss modulus $G''(f)$ with increasing sample age, where $G''(f)$ is a measure for the energy dissipation in the network. At intermediate frequencies, i.e. around 1 Hz, the loss modulus is one order of magnitude lower than $G'(f)$. This is a well-known characteristic for crosslinked and bundled actin networks and for soft glassy materials in general(95). Actin/fascin bundle networks show a distinct minimum in the viscous dissipation(2). As depicted in Fig. 7.1, this minimum in the loss modulus shifts to lower frequencies with increasing sample age. At the same time, the shape of the loss modulus becomes gradually flatter and the minimum eventually completely disappears. The evolution of the sample viscoelasticity is not triggered by a mesoscopic change in the overall network structure or bundle thickness, as confirmed by microscopy. The crosslinks between distinct actin/fascin bundles, however, may play an important role for the relaxation process of the network.

It is important to notice that the age dependence of the viscoelastic properties of crosslinked actin networks crucially depends on the binding protein. For instance, actin bundle networks crosslinked by the protein espin show an age dependent behavior with a trend similar to that of actin/fascin networks, whereas the elasticity of isotropically crosslinked actin/rigor-HMM networks increases over time. However, these actin/HMM networks also exhibit a pronounced minimum in the viscous dissipation. It has been shown that this minimum arises from thermal crosslinker unbinding events(110). The detailed position of this minimum depends on the density and life-time of the crosslinks in the network as well as the amount of internal or external stress(7, 110, 111).

In comparison to these isotropically crosslinked actin networks, the shift and flattening in the minimum of $G''(f)$ observed for actin/fascin bundle networks suggests that for samples of higher age less energy is dissipated by thermal crosslinker unbinding. This decrease in the dissipation might either be due to a loss of crosslinking points over time or due to a continuous decrease of elastic energy that is stored in individual crosslinks. In the first case, crosslinking fascin molecules would have to unbind and diffuse to new binding sites without forming new bundle-bundle interconnections. For energetic reasons, only a position *within* a fascin bundle would be favorable to allow for this reorganization in an efficient enough manner. This hypothesis can be tested by analyzing the viscoelastic properties of actin/fascin bundle networks at a higher fascin concentration such as $R = 0.5$, i.e. where the binding sites within the bundles are saturated(90). However, at this high fascin concentration we observe a similar decrease in the network elasticity with increasing sample age. This indicates that another relaxation mechanism must be responsible for the observed aging process.

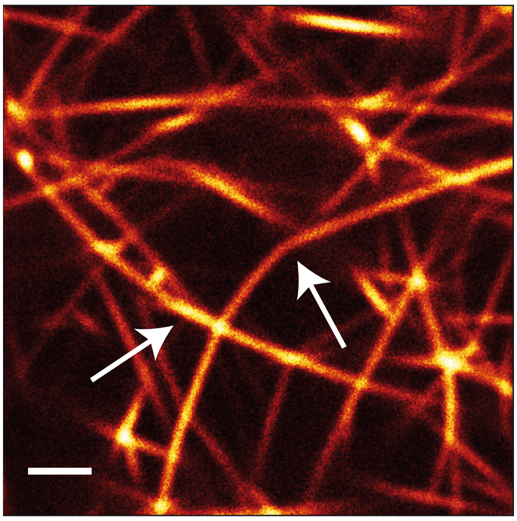

Figure 7.2: Confocal image of a fluorescently labelled actin/fascin bundle network ($c_a = 9.5$ µM, $R = 0.1$) $\sim$ 1 hour after initiation of polymerization. Bending of individual bundles is observed (marked by white arrows), indicating the presence of internal stress fields. The scale bar represents 2 µm.

In the second case, i.e. if the amount of stored energy per crosslink decreases over time, the network has to release internal stress with increasing sample age t_w. If this holds true, then it might be possible to pick up signatures of the existence of internal stresses by microscopy. We use confocal microscopy to monitor the formation of the network and observe a slight bending of individual bundles during the network polymerization (white arrows in Fig. 7.2). This local bundle bending might facilitate the formation of a higher number of crosslinks between distinct bundles compared to a scenario where all bundles are fully relaxed and thus further apart.

7.3 INTERNAL STRESS RELAXATION

Due to the high stiffness of an individual actin/fascin bundle(112), the occurrence of bent bundles is a good indication for the build-up of internal stress fields storing elastic energy in each crosslink. We confirm these findings by measuring mesoscopic displacement maps of the aging network (see chapter 2). Displacement maps are calculated over a time lag $\tau = 330$ s for different sample ages t_w; they cover an area of 1280 µm x 220 µm (Fig. 7.3a). After network formation, we observe locally heterogeneous displacements with patches of correlated motion and an average displacement of $<\delta>= 0.91$ µm (Fig. 7.3b, $t_w \approx 0$ h). At intermediate sample ages (Fig. 7.3c, $t_w \approx 3$ h), these displacements are considerably smaller and appear to be more randomly distributed, until hardly any dis-

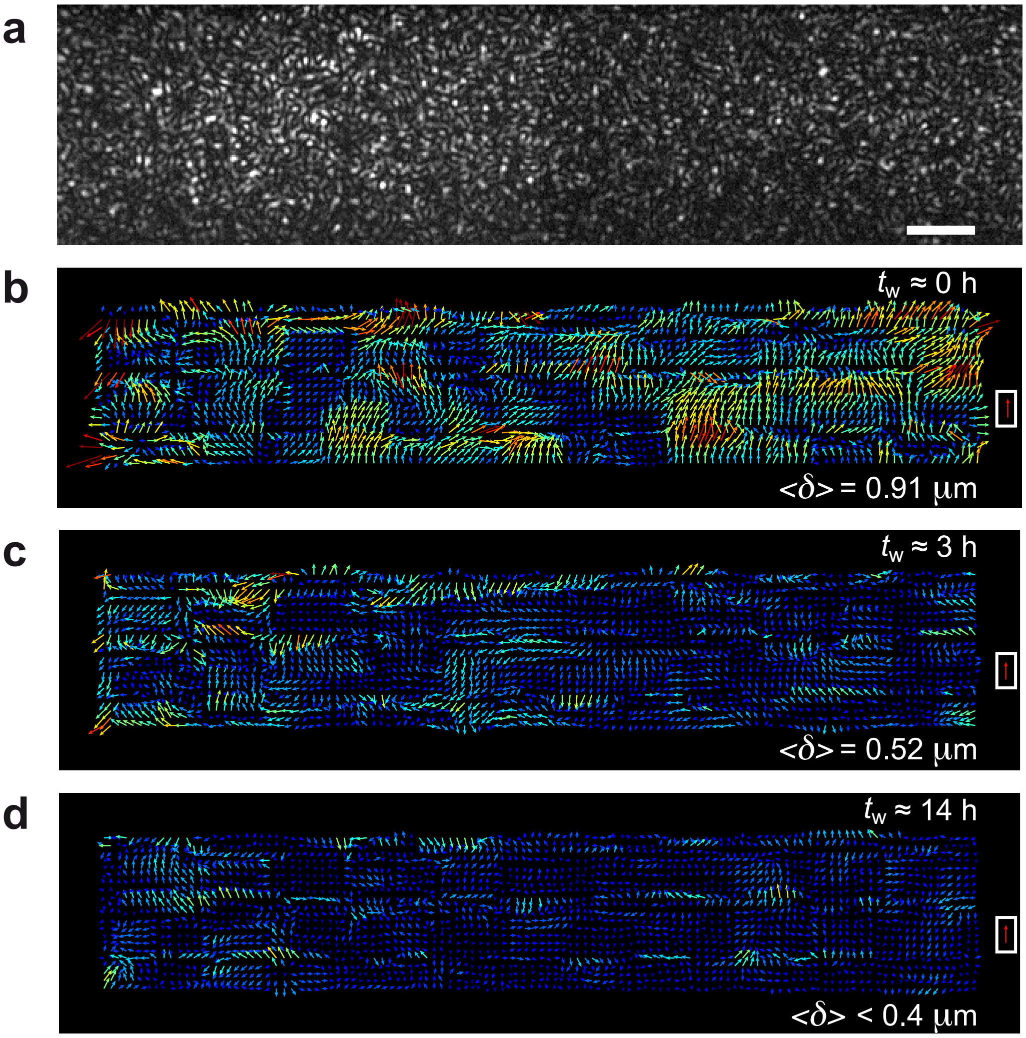

Figure 7.3: Internal stress fields in actin/fascin bundle networks ($c_a = 9.5$ µM, $R = 0.1$) decay with increasing sample age. Displacement maps are obtained from the speckle pattern scattered by the sample and show a decrease in the internal network displacements over time. A typical speckle pattern is depicted in (a). The scale bar represents 100 µm. (b)-(d) Vectors indicate local displacements in the speckle pattern during a time interval of 330 s. The magnitude of displacement is indicated by the vector length and color (small displacements are colored in blue, large displacements in red) and the average displacement per map, $< \delta >$, is denoted in the lower right corner of each map. The reference vector in the white square right of the vector fields corresponds to a 500 nm displacement. Sample ages are denoted in the top right corner. The total size of the displacement maps corresponds to the size of the speckle pattern in (a). Black voids around the vector fields are due to border limitations of the detection algorithm.

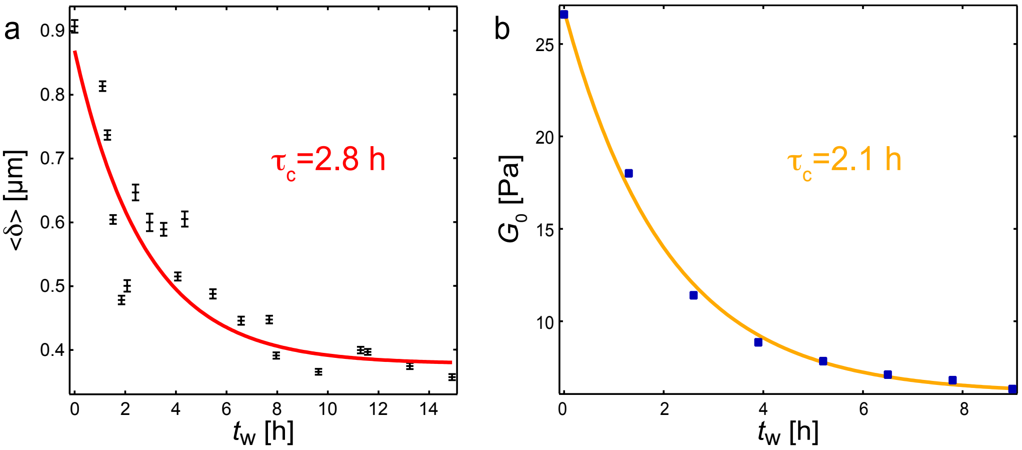

Figure 7.4: The temporal evolution of the microscopic displacements and that of the macroscopic network elasticity follow the same kinetics (see main text for details). (a) $< \delta >$ is the average displacement over 330 s (black markers, see Fig. 7.3; error bars denote the error of the mean) and follows approximately an exponential decay (red line). (b) shows the age dependence of the macroscopic network elasticity G_0 (blue markers), which can also be fitted with an exponential function (orange line), and a decay time comparable to that obtained from the $< \delta >$ data.

placement can be detected anymore for $t_w \approx 14$ h (Fig. 7.3d). This temporal evolution of the local displacement field underlines the existence of internal stresses and their age dependent decrease.

Having established the existence of internal stresses, we now aim to test if internal stress relaxations can explain the observed age dependence of the macroscopic network viscoelasticity. First, we compare the kinetics of the change in the macroscopic network elasticity with the kinetics of microscopic displacements. The temporal evolution of the storage modulus shows an exponential decay $G_0 \sim \exp(-t_w/\tau_c)$ (Fig. 7.4b). To obtain a quantity describing the kinetics of the macroscopic aging process we calculate the time derivative $\mathrm{d}G_0/\mathrm{d}t$, which consequently follows an exponential function with the same characteristic time scale τ_c and find $\tau_c = 2.1$ h. This value can now be compared to the kinetics of the local displacements as obtained from the mesoscopic displacement maps. As shown in Fig. 7.4a, the temporal evolution of the average of these local displacements (black markers) can also be fitted with an exponential decay (red line) and the corresponding time constant $\tau_c = 2.8$ h matches the value obtained from our analysis of the macrorheological data reasonably well. This finding supports the notion that the age dependent alterations in the mesoscopic strain field and the macroscopic network elasticity are linked.

Internal stress fields should facilitate stochastic unbinding of actin/fascin crosslinks. A local relaxation of these internal stresses and consecutive rebinding of the crosslinking proteins would leave the network in a more relaxed state. The off-rate of a single molecular bond depends on the mechanical load on the bond, F, as $k_{\mathrm{off}}(F) = k^0_{\mathrm{off}} \exp(F\Delta x / k_{\mathrm{B}}T)$, where k^0_{off} represents the off-rate of the bond in the absence of mechanical load and Δx denotes the bond length. Accordingly, a continuous decrease in the internal network stress would decrease the unbinding probability with increasing network age as the network keeps relaxing. This picture would be consistent with the macrorheologically observed slow-down in the change in network viscoelasticity.

Similarly, additional external forces would favor the unbinding process by tilting the actin/crosslinker interaction potential(113, 114). Thus, the relaxation process of the network should be enhanced by a short external stress pulse. Indeed, such a behavior is observed if the network is exposed to an external strain beyond the critical point(102), i.e. if the network response is driven into the non-linear regime without inducing rupture. After this short mechanical loading procedure, a slight but significant drop in the network elasticity is observed, i.e. a 2-fold decrease which is comparable to 2 hours of thermal/undriven relaxation (Fig. 7.5a and d). After this enhanced relaxation the decrease of the viscoelastic moduli continues – albeit at a lower rate. This behavior is qualitatively different from the 'rejuvenation' process described for certain soft glassy materials and cells(97, 106) where the application of shear results in a reversal of the aging process. However, rejuvenation has so far only been observed for systems that stiffen with age.

Should transient crosslinker un- and rebinding be indeed responsible for the observed temporal evolution of the network properties, this evolution would be suppressed by locking the actin/fascin bond. This can be achieved by adding glutaraldehyde to the network, a chemical that covalently links neighboring proteins by the formation of a Schiff base. Such a procedure has already been applied successfully to cells and isotropically crosslinked actin networks(110, 115). Here, the careful application of F-buffer containing 0.1%(v/v) glutaraldehyde on the liquid-air interface of a fully polymerized actin/fascin bundle network results in an almost constant elastic modulus over the course of more than 10 hours (Fig. 7.5b and d). At the same time, the distinct minimum in the loss modulus $G''(f)$ at low frequencies becomes less and less pronounced over time and eventually completely disappears whereas the loss modulus at high frequencies remains constant. This agrees with earlier experiments on isotropically crosslinked actin networks where a suppression of the crosslinker unbinding kinetics by glutaraldehyde eliminated the increase of $G''(f)$ at low frequencies as well(110). Applying the same protocol using buffer without

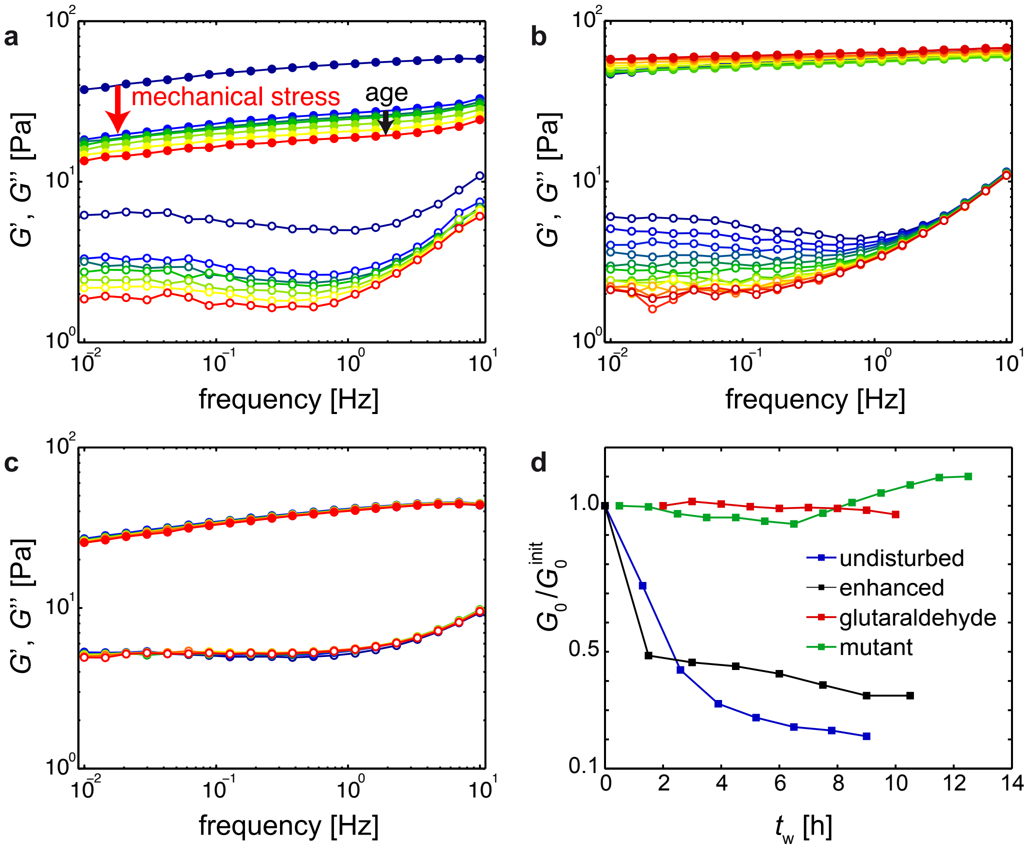

Figure 7.5: The age dependent changes in the viscoelastic network response can be modified by varying external or internal parameters. (a) A short external stress pulse entails a sudden drop in both viscoelastic moduli (red arrow) which is then followed by a continuous relaxation (black arrow). (b) The application of 0.1%(v/v) glutaraldehyde stabilizes the elastic modulus $G'(f)$ by covalently locking the actin/fascin bonds. The loss modulus $G''(f)$ still evolves over time, yet only at low frequencies (see text). (c) A fascin-S39A mutant with altered actin binding affinity forms a bundle network that exhibits no temporal evolution in the viscoelastic moduli. (a)-(c): Closed circles denote the storage modulus $G'(f)$, open circles represent the loss modulus $G''(f)$. (d) Relative change of the plateau modulus $G_0 := G'(10\,\text{mHz})$ with respect to its initial value G_0^{init} for different actin/fascin bundle networks. The actin concentration is $c_a = 9.5\ \mu\text{M}$ for all experiments and the ratio of fascin to actin is $R = 0.1$. Measurement intervals and total experiment durations can be obtained from the graph.

glutaraldehyde results in relaxation dynamics similar to that depicted in Fig. 7.1 (data not shown). These experiments demonstrate that the transient nature of the actin/fascin bond is crucial for the relaxation process of the network.

7.4 ANALYSIS OF MICROSCOPIC RELAXATION DYNAMICS VIA DYNAMIC LIGHT SCATTERING

So far, we have analyzed the age dependence of the actin/fascin system on a macroscopic or mesoscopic length scale. Yet, if the process is indeed dictated by a local stress release due to transient crosslinker unbinding, a qualitatively similar signature of the relaxation process should also be detectable on a microscopic scale. Dynamic Light Scattering (DLS)(116) is a suitable method to probe the microscopic dynamics of a colloidal or polymer-based sample. For this study we choose a setup that allows for probing the dynamics on length scales $1/q \approx 0.2 - 1\ \mu$m, where q is the scattering vector, and time scales ranging from seconds to several hours (see materials and methods). We analyze temporal series of images of the speckle pattern that is formed by the scattered light (Fig. 7.3a) and calculate the temporal autocorrelation function of the scattered intensity, $g_2(t_\mathrm{w}, \tau, q) - 1$, as defined in the materials and methods section. We measure $g_2 - 1$ for an actin/fascin network in the very same conditions as probed with rheology, i.e. in the bundle phase ($R = 0.1$). For short delay times, $2\ \mathrm{s} < \tau < 30\ \mathrm{s}$, the corresponding correlation function exhibits a plateau (Fig. 7.6a) indicating that there are no measurable dynamics on the probed length scale. At larger delay times $\tau > 1$ h, however, we observe a decorrelation of the speckle pattern and a steep decay of the correlation function. This indicates the existence of a slow process which entails significant microscopic rearrangements in the network.

Next, we compare correlation functions for different sample ages t_w (Fig. 7.6a). To quantify the characteristic time scale of the decorrelation process, a stretched exponential is fitted to the final decay of the correlation function, $g_2 - 1 \sim \exp\left(-\frac{\tau}{\tau_0}\right)^{\beta} + c$, with c a base line. Fig. 7.6b shows the evolution of the relaxation time τ_0 extracted from the fit as a function of t_w. A higher relaxation time corresponds to a slower decorrelation process and thus slower microscopic dynamics in the sample. For undisturbed actin/fascin networks the relaxation time increases with sample age by more than one order of magnitude, which agrees with the observed slow-down in the macromechanical experiments and the decrease of the mesoscopic displacement $< \delta >$. The slow down in the relaxation

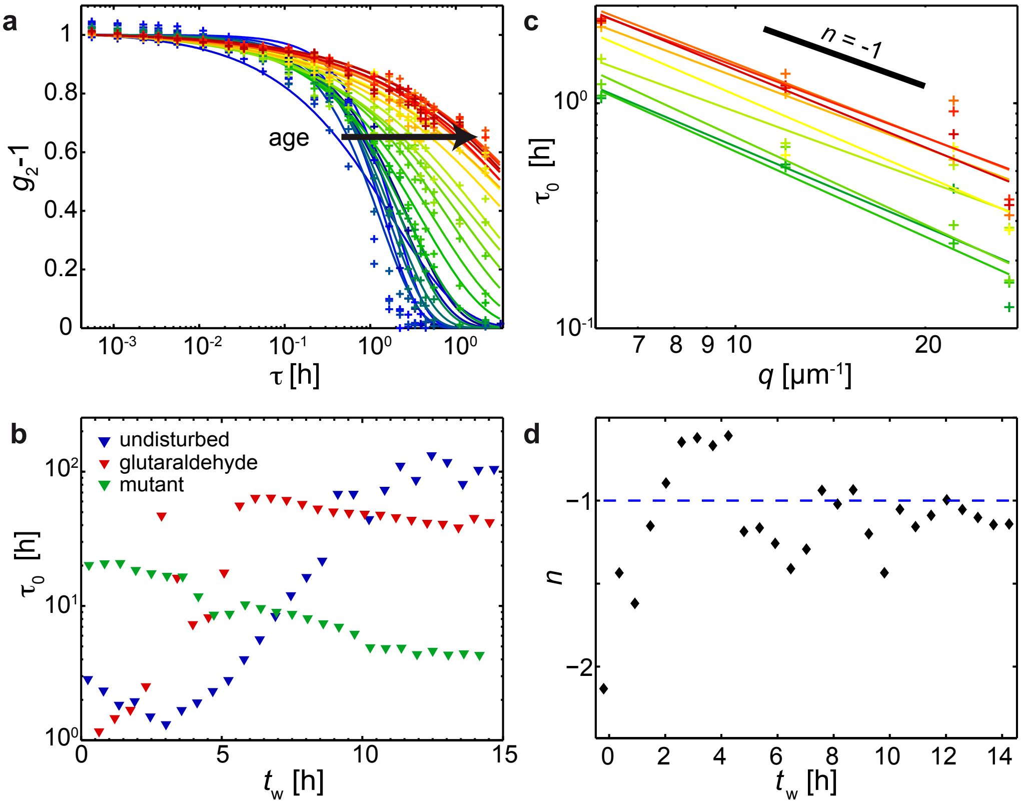

Figure 7.6: Actin/fascin bundle networks exhibit age-dependent internal dynamics. (a) The correlation function $g_2 - 1$ obtained from DLS decreases with increasing τ which denotes the delay time between two correlated speckle images. The time scale of the decorrelation process, τ_0, depends on the sample age which ranges from $t_w \approx 0$ h (blue) to $t_w \approx 15$ h (dark red). Solid lines represent stretched exponential functions that are fitted to the data (crosses). $g_2 - 1$ is normalized with respect to the degree of correlation after 2 s after subtraction of a base line value $c < 0.2$. The data was recorded at a scattering angle of 45° ($q = 12.0\ \mu\text{m}^{-1}$). (b) τ_0 denotes the characteristic decay time of the stretched exponential functions as displayed for the undisturbed sample in (a). An increase in τ_0 is equivalent to a slow-down of internal sample dynamics. The temporal evolution of τ_0 is shown for different actin/fascin bundle networks as indicated by the legend. The actin concentration is $c_a = 9.5$ µM and the ratio of fascin to actin is $R = 0.1$ for all experiments. For the glutaraldehyde sample, the initial fluctuations are due to the diffusion of glutaraldeyhde into the network. (c) In undisturbed actin/fascin bundle networks ($c_a = 9.5$ µM, $R = 0.1$), the relaxation time τ_0 scales with the scattering vector q as $\tau_0 \sim q^n$, $n \approx -1$ (see text for details). Solid lines represent power law fits to the data (crosses). The color code indicates the sample age (green: $t_w \approx 5$ h, red: $t_w \approx 14$ h). The black bar indicates a power law $\tau_0 \sim q^{-1}$ for comparison. (d) shows the scaling exponent n as a function of sample age t_w.

process continues until τ_0 reaches a constant limit value after ~ 10 h. This aging behavior is similar to that reported for many soft glassy materials investigated by DLS. Aging behavior in soft glasses is often associated with anomalous dynamics(93, 98–101), where the relaxation time τ_0 scales with the scattering wave vector as $\tau_0 \sim q^{-1}$, indicative of ultraslow "ballistic" dynamics, as opposed to diffusive motion, for which $\tau_0 \sim q^{-2}$. It has been argued that ballistic motion is the signature of internal stress driven dynamics(98, 99). Here, we find $\tau_0 \sim q^{-1}$, further supporting the notion that the evolution of our actin/fascin bundle networks is ruled by stress relaxation (Fig. 7.6c).

7.5 ALTERATION OF INTERNAL STRESS BY FASCIN MUTANTS

In a last step, we now aim to demonstrate that the time scale of the relaxation process described so far is set by the life time of the crosslinker/actin bond, i.e. the time scale of the unbinding kinetics. Those unbinding kinetics are governed by the microscopic interaction potential between the crosslinker and actin which has already been demonstrated to crucially affect the dynamic viscoelastic response of isotropically crosslinked actin networks(111). Accordingly, changes in the crosslinker binding affinity should also cause a measurable difference in the dynamic viscoelastic behavior of a bundled actin network. Indeed, suppressing the crosslinker unbinding dynamics by the addition of glutaraldehyde – similar to what we have already described in our macrorheological experiments — results in a high and almost constant value of the relaxation time (Fig. 7.6b). A less drastic change in the binding affinity of the crosslinker can be achieved by mutating the actin binding site of the fascin molecule. It has been shown *in vivo* that replacing serin 39 in one of the actin binding domains of the fascin molecule by an alanin residue results in a functional mutant(29, 30). This fascin-S39A mutant is able to bundle actin in a fashion similar to the wild type. We now test to what extent a change in the binding affinity as induced by this mutation affects the relaxation dynamics of actin/fascin bundle networks.

A macrorheological analysis of actin/fascin-S39A bundle networks reveals a subtle but important difference in the viscoelastic network behavior (Fig. 7.5c and d): Whereas the linear moduli of wild type and mutant fascin/actin bundle networks are comparable, the age-dependent decrease of $G'(f)$ is absent in the mutant network. At the same time, the shift and flattening of the minimum in the viscous dissipation $G''(f)$ observed for the wild type fascin network is hardly present in the fascin-S39A mutant network. Consistently, the strong increase of the relaxation time τ_0 obtained from DLS that is observed for wild type fascin does not occur for the fascin-S39A mutant (Fig. 7.6b). For the mutant fascin we observe that at high ages the relaxation time τ_0 exhibits a value that is approximately one order of magnitude lower than the corresponding value of the glutaraldehyde sample and the undisturbed wild type system (Fig. 7.6b). These relaxation time limits are most likely set by thermal crosslinker unbinding events which will persist even if all internal stress has been released. In that case, a smaller relaxation time and thus faster relaxation dynamics suggests a higher off-rate for the fascin-S39A/actin bond compared to the wild type fascin, which would be consistent with previous findings from centrifugation assays(29). As a consequence, this would imply that the internal relaxation processes in the mutant fascin network are considerably sped up and take probably place on the time scales of the polymerization. Thus, the fascin-S39A mutant bundle network would have already reached a mostly relaxed state right after polymerization rendering further relaxation processes negligible and unnecessary.

7.6 CONCLUSION

In summary, we have demonstrated that crosslinked actin/fascin bundle networks undergo a slow relaxation process that takes place on time scales which are much longer than those of the network polymerization and standard rheological experiments. We have shown that the continuous relaxation of internal stress fields, which build up during the network formation, gives rise to the observed behavior. This relaxation mechanism is triggered by stochastic crosslinker unbinding events occuring between distinct bundles. The complex dynamics of actin/fascin bundle networks described here is a striking example of how relatively simple *in vitro* actin networks can display out-of-equilibrium properties as they are also observed by living cells. The structural and mechanical relaxation of freshly assembled actin networks will also contribute to the complex dynamics of the cytoskeleton *in vivo* as the cellular microstructure is constantly remodelled and adapted(117). However, the lack of a detailed microscopic understanding of these slow relaxation processes in the crowded environment of a living cell has so far defied a quantitative correlation of the microscopic processes with the macromechanical cell behavior. The well-defined model system described here allows for elucidating such a correlation and thus provides a benchmark for addressing more complicated systems, such as composite cytoskeletal networks or active networks including molecular motors. At a more general level, the experiments reported here provide the first unambiguous proof that internal stresses may build up during the formation of disordered, soft glassy materials and then can drive their slow evolution, a mechanism often proposed but not yet proved. The binding/unbinding process demonstrated here is likely to be the microscopic origin of the slow dynamics of a large class of network-forming materials, including colloidal gels, for which a similar mechanism has been invoked in the past(98, 99).

8

OUTLOOK

The main goal of this thesis was to establish and characterize a model system for the intermediate filament cytoskeleton. With the unraveling of kinetic trapping in keratin networks and new insights into the role of Hsp27 in the cytoskeletal context, the system has already demonstrated its significance. Moreover, establishing several key principles surrounding network assembly and arrangement has enabled the investigation of systems with added complexity: keratin/actin composite systems. In the following, some future perspectives on the continued study of such cytoskeletal networks will be discussed.

KERATIN BUNDLING

One of the most striking features of the investigated keratin networks is the intrinsic ability of keratin 8/18 filaments to bundle. This behavior is essential for the described non-equilibrium nature of these systems. Studies of other intermediate filaments have demonstrated the tail domain to be a likely candidate for mediating such interactions(48, 63). However, while deleting the tails of both keratin 8 and 18 does influence the general network structure, bundling prevails (see Fig. 5.5 e). Therefore, additional, yet unknown, factors are expected to contribute to lateral filament association. The presented model system is ideally suited to support investigations in this direction, especially when considering the role of controlled ionic conditions and the use of mutant proteins.

LIGHT-INDUCED ASSEMBLY

An interesting experimental avenue to explore will be light-induced changes of ionic conditions. Specially designed, photolabile chelators, such as o-nitrophenyl EGTA, release Ca^{2+} ions upon illumination(118). This enables the controlled *in situ* initiation of network assembly without the necessity and limitations of a diffusion chamber or droplet assembly. A similar approach can be used to locally release protons and study the effect of changes in pH(119).

PHOSPHORYLATION

So far, only the assembly process of the network was considered. In cells, however, the keratin cytoskeleton undergoes a constant cycle of assembly and disassembly mediated by kinases(51, 53, 120). In this context, the p38 MAP kinase induced phosphorylation of serine 73 in K8's head domain seems to be a key aspect(121). Moreover, phosphorylation of serine 431 in the tail domain of K8 has been shown to be the crucial step in SPC induced reorganization of the keratin cytoskeleton(56, 57). It hence will be interesting to incorporate the effect of kinases and aspects of post-formation remodeling in our system. The diffusion chamber discussed in chapter 6 offers the means to introduce active kinases after network formation. This will not only allow us to investigate the influence of such a remodeling on the network, but will also provide the means to verify if single kinase action is sufficient to effect filament disassembly or if additional factors play a role.

ASSOCIATED PROTEINS

The oligomeric state of Hsp27 is also altered by phosphorylation, for example during heat shock(70). It seems probable that such changes feed back on Hsp27's effect on keratin networks. Moreover, the proximal part of the tail domain, where Hsp27 appears to bind, features one of K8's major phosphorylation sites (S431; the same site involved in SPC induced phosphorylation). Future work will therefore investigate how keratin phosphorylation affects Hsp27-keratin interaction. Notably, in many cancer types Hsp27 overexpression correlates with increased metastatic capabilities of malignant tumor cells(122). Additionally, recent studies report an increased tumor cell migration due to SPC-induced reorganization of the keratin cytoskeleton(56, 57, 123). It will therefore be exciting to further explore the role of Hsp27-dependent alterations of the keratin cytoskeleton *in vivo*. Assessing the potential of other small heat shock proteins - αB-crystallin, for example, has been reported to interact with desmin intermediate filaments - to influence keratin assembly, will show if the observed effect can be extended to other systems(75). In principle, other keratin associated proteins, such as the proposed crosslinker epiplakin, should also have the ability to influence the balance between filament elongation and bundling, thereby impacting network formation and structure. Initial experiments in this direction support this notion.

DEEP STED

The networks investigated in this work, even at high Hsp27 concentrations, still exhibit relatively large mesh sizes compared to those found in cells (124). While such fine networks can also be produced *in vitro*, for example by increasing protein concentration, the associated length scales are below the resolution of a standard confocal microscope, requiring for more advanced techniques such as STED microscopy for their imaging. While STED microscopy has been used in the scope this thesis work, the limitations of the setup - confining significant improvement in resolution to a narrow region in the proximity of the surface - have hampered the broader application of this technique. These issues can be addressed by further improvement of the setup, for example by using an index-matched objective with a correction collar optimized for deep imaging.

RHEOLOGY

So far, proper rheological assessment of the examined networks has been, in part, hindered by the complex sample preparation and fast assembly time scales of keratin networks. Yet, only the combined study via confocal microscopy and rheology will yield the details necessary for a thorough investigation and comparison of single component and composite networks. There are several possibilities to gain insight into rheological aspects of such systems. To evaluate their behavior on the macroscopic level of the entire network with great accuracy, torsional macrorheology is the method of choice. Here, a network, placed in a thin gap between one stationary and one rotating plate, is subjected to torsional stress and the ensuing strain response is recorded(125, 126). However, commercially available rheometers are not compatible with the network assembly protocols established in this work, particularly the fast assembly time scales of keratin networks under physiological conditions. The only feasible approach to provide percolating, macroscopically homogeneous networks in cytosol-like ionic conditions is the *in situ* assembly similar to that introduced for the shear chamber setup in chapter 6. Following this strategy, a commercial rheometer will be modified to incorporate a diffusion chamber(Fig. 8.1). In contrast to the shear chamber, where the reservoir could be placed in the mobile upper stage of the setup to allow imaging from below,

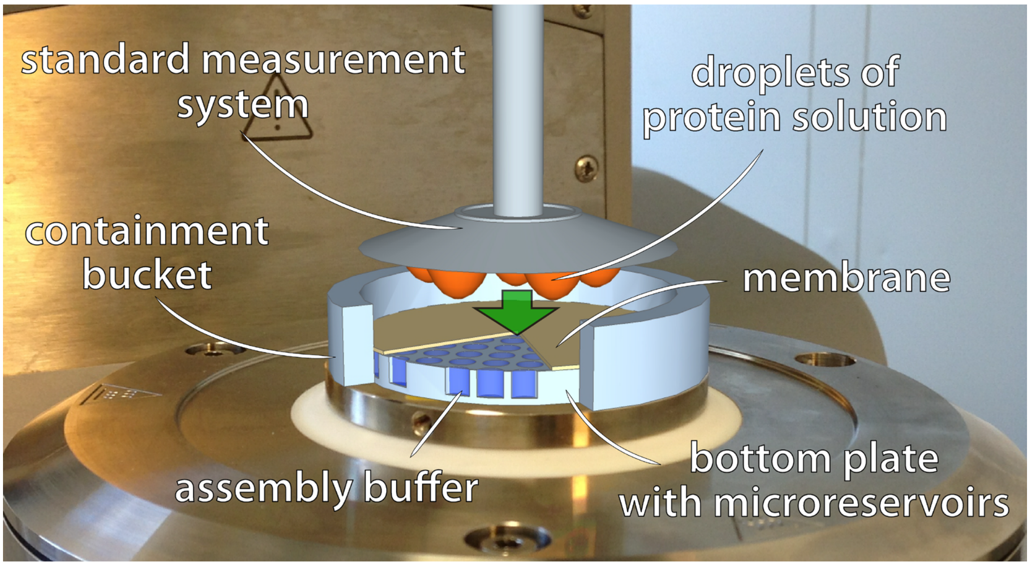
standard measurement system
droplets of protein solution
containment bucket
membrane
assembly buffer
bottom plate with microreservoirs

Figure 8.1: Macrorheometer with diffusion setup for *in situ* assembly. The image shows the conceptual layout of a commercial rheometer modified for *in situ* assembly of keratin networks. The static bottom plate of the rheometer is replaced by a membrane supported by a steel plate. Into this plate small holes are inserted to act as microreservoirs. By this means, both homogeneous diffusion of ions from the reservoir to the sample volume and the necessary structural stability of the bottom plate is ensured. A surrounding containment bucket simultaneously serves as a solvent trap and fixture for the membrane. For assembly, droplets of protein solution can be applied to the upper plate and then lowered onto the membrane in a quick, controlled and reproducible manner.

here, inverting this geometry is more feasible. The first step will therefore be to follow a dual-setup approach, imaging network rearrangements in the shear chamber and measuring the rheological response of similar networks in the modified rheometer. A rigorous quality control of networks assembled in the rheometer is essential for this strategy. To this end, an imaging chamber will be developed that allows for *in situ* assembly in the rheometer, followed by a transfer to a confocal microscope for imaging. On the long run, a direct combination of confocal microscope and rheometer would be ideal. Such a confocal rheometer would allow one to directly relate the measured macromechanical response of a network to the associated microscopic structural rearrangements. This is especially important for experiments where the variation between samples is expected to be significant, such as yielding assays or the examination of naturally inhomogeneous samples. To achieve simultaneous rheological measurements and imaging, the diffusion chamber would have to be integrated into the rotating upper plate of the rheometer, a setup similar but inverted to that depicted in Fig. 8.1. Establishing such a macrorheological assay for keratin and keratin/actin composite networks will also support the investigation of their dynamic properties on very long time scales of several hours, as discussed in chapter 7 for actin/fascin bundle networks. To support any of the above strategies for the combined investigation of network structure and mechanics, an extended analysis of the data will be of great avail. While the extracted deformation field discussed in chapter 6, yields important informations, it would also be vital to evaluate other parameters, such as the increasing alignment of structures to the direction of shear.

COMPOSITE NETWORKS

The cytoskeleton is a composite material by nature. For crosslinked networks formed from different types of synthetic polymers, recent works have demonstrated their impressive potential for enhanced mechanical properties and it is likely that similar emergent behavior is exhibited by keratin/actin composite networks(91, 92, 127). The most prominent hallmark of these systems is their increased resistance to mechanical failure. It is during the loss of their structural integrity where the composite nature of these systems comes into play. The drastic inhibition of crack propagation, for example, has been tentatively attributed to increased energy dissipation during breakage of the first network while the second network remains intact causing a redistribution of stresses over large areas of the network away from the crack tip. While such a scenario is plausible, the investigated synthetic hydrogels do not allow for a direct assessment of the proposed mechanisms, due to the inaccessibility of the microscopic network structure. The introduced cytoskeletal composite networks, in contrast, are well suited for fluorescence microscopy based investigation of their substructure and might therefore represent the ideal model system to identify the origin of the observed synergetic effects. In addition, it will be fascinating to explore if similar emergent behavior can be used by the cell to tailor its mechanical properties. However, while chapter 6 demonstrated the feasibility of composite network assembly and established crucial experimental techniques, the emergent behavior proposed for these system remains to be further investigated. As for their synthetic counter part, it is likely that synergetic properties become most evident during the critical processes during mechanical failure. In addition to the general characterization of their mechanical properties, a special focus will therefore be on experiments investigating defect formation and propagation in composite keratin/actin networks. Here, one of the primary challenges is the trade-off between the resolution and the field of view of a microscope: while spontaneous initiation of mechanical failure in a homogeneous material can occur anywhere in the sample, it is not possible to simultaneously image the entire volume at the necessary resolution. I therefore propose the following strategy: First, networks are assembled in the shear chamber, where they can then be strained close to, but not beyond the point of failure. In this configuration, controlled incision with a UV-laser is used to trigger local failure. A spinning disc confocal microscope then records the evolution of the introduced defect with high temporal and spacial resolution. Replacing the shear chamber with a rheometer setup would even allow the setting of specific stresses and to simultaneously assess the networks rheological response during the deterioration of its structural integrity. By this means, a controlled study of the yielding behavior of these networks can be pursued. In this context, inter-species crosslinking molecules, such as plectin, can be used to modulate keratin-actin interconnectivity, potentially having a profound impact on the investigated material properties.

VESICLES

In addition to the cytoskeleton's network properties, its interaction with the confining cell membrane is an important factor. Mimicking both membrane interaction and confinement can be achieved by incorporating networks into lipid vesicles. Preliminary experiments have already demonstrated that keratin network assembly in vesicles produced via the cDICE method is feasible (Fig. 8.2)(128). To this end, proteins are incorporated into the vesicle during production in a soluble state and α-hemolysin, a calcium specific ionophore, is introduced into the vesicle membrane. Then, network formation is induced by an exchange of the exterior buffer and subsequent diffusion of ions into the vesicle lumen. Interestingly, keratin seems to spontaneously couple to the lipid membrane, yielding a network spanning the entire vesicle. Contractile forces within the network can even be transmitted to the membrane. Furthermore, this proof of principle, in combination with already established actin incorporating vesicles, serves as the first step towards more complex composite networks in vesicles.

ACTIVE SYSTEMS

One crucial aspect of the cytoskeleton, so far not discussed, is the active component induced by molecular motors. While intermediate filaments do not serve as tracks for motor proteins, keratin/actin composite network are well suited for the addition of motor proteins, such as myosin or kinesin. Reconstituted systems of actin, cross-linking molecules and motors exhibit a wealth of intricate dynamics, including active network contraction(5, 6).

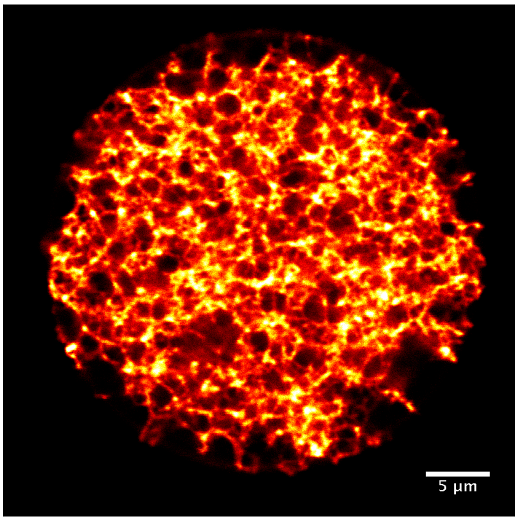

Figure 8.2: Keratin network in a vesicle. The image shows a network of keratin 8/18 assembled in a vesicle produced via the cDICE method. The very dense network spontaneously attaches to the lipid membrane, keeping it from collapsing. The keratin concentration was $c_K = 13$ µM.

It will therefore be interesting to confront such a contractile network with a highly stable keratin scaffold counterpart.

Combining such an active composite network with the confinement of a vesicle will represent the first model system featuring this level of complexity, capturing the intricacy of the cytoskeleton in unprecedented depth.

BIBLIOGRAPHY

1. A. R. Bausch and K. Kroy, *Nat Phys*, 2006, **2**, 231–238.
2. O. Lieleg and A. R. Bausch, *Phys. Rev. Lett.*, 2007, **99**, 158105.
3. K. M. Schmoller, T. Niedermayer, C. Zensen, C. Wurm and A. R. Bausch, *Biophys. J.*, 2011, **101**, 803–808.
4. M. L. Gardel, M. T. Valentine, J. C. Crocker, A. R. Bausch and D. A. Weitz, *Phys. Rev. Lett.*, 2003, **91**, 158302–.
5. S. Köhler and A. R. Bausch, *PLoS ONE*, 2012, **7**, e39869.
6. S. Köhler, V. Schaller and A. R. Bausch, *Nature Materials*, 2011, **10**, 462–468.
7. G. H. Koenderink, Z. Dogic, F. Nakamura, P. M. Bendix, F. C. MacKintosh, J. H. Hartwig, T. P. Stossel and D. A. Weitz, *Proc. Natl. Acad. Sci.*, 2009, **106**, 15192–15197.
8. V. Schaller, C. Weber, C. Semmrich, E. Frey and A. R. Bausch, *Nature*, 2010, **467**, 73–77.
9. V. Schaller, C. A. Weber, B. Hammerich, E. Frey and A. R. Bausch, *Proc. Natl. Acad. Sci.*, 2011, **108**, 19183–19188.
10. H. Herrmann, T. Wedig, R. M. Porter, E. B. Lane and U. Aebi, *J. Struct. Biol.*, 2002, **137**, 82–96.
11. T. Lichtenstern, N. Mücke, U. Aebi, M. Mauermann and H. Herrmann, *J. Struct. Biol.*, 2012, **177**, 54–62.
12. A. L. T. P. O. M. P. W. H. H. M. Beil, T. Paust, O. Marti, P. Walther, H. Herrmann and M. Beil, *Biophys. J.*, 2012, **103**, 195–201.
13. Y.-C. Lin, N. Y. Yao, C. P. Broedersz, H. Herrmann, F. C. MacKintosh and D. A. Weitz, *Phys. Rev. Lett.*, 2010, **104**, 058101.
14. K. M. Schmoller, O. Lieleg and A. R. Bausch, *Soft Matter*, 2008, **4**, 2365–2367.

15. T. T. Falzone, M. Lenz, D. R. Kovar and M. L. Gardel, *Nat. Commun.*, 2012, **3**, 861.
16. H. Herrmann, M. Häner, M. Brettel, N. Ku and U. Aebi, *J. Mol. Biol.*, 1999, **286**, 1403–1420.
17. J. Buchner, M. Ehrnsperger, M. Gaestel and S. Walke, *Meth. Enzymol.*, 1998, **290**, 339–349.
18. N. de Miguel, N. Braun, A. Bepperling and T. Kriehuber, *Biochim. Biophys. Acta*, 2009, **1793**, 1738–1748.
19. M. Hatzfeld and K. Weber, *J. Cell Sci.*, 1990, **97 (Pt 2)**, 317–324.
20. E. Basha, H. O'Neill and E. Vierling, *Trends Biochem. Sci.*, 2012, **37**, 106–117.
21. M. J. Vos, J. Hageman, S. Carra and H. H. Kampinga, *Biochemistry*, 2008, **47**, 7001–7011.
22. D. Wildanger, E. Rittweger, L. Kastrup and S. W. Hell, *Opt Express*, 2008, **16**, 9614–9621.
23. P. Schuck, *Biophys. J.*, 2000, **78**, 1606–1619.
24. T. M. Laue, B. D. Shah, T. M. Ridgeway and S. L. Pelletier, *Analytical Ultracentrifugation in Biochemistry and Polymer Science*, Royal Society of Chemistry, Cambridge, UK, 1992, pp. 90–125.
25. M. P. Bova, *J. Biol. Chem.*, 2002, **277**, 38468–38475.
26. A. P. T. Salmazo, *PhD thesis*, Universität Wien, 2009.
27. J. A. Spudich and S. Watt, *J. Biol. Chem.*, 1971, **246**, 4866–4871.
28. H. Kurokawa, W. Fujii, K. Ohmi and T. Sakurai, *Biochemical and biophysical research communications*, 1990, **168**, 451–457.
29. S. Ono, Y. Yamakita, S. Yamashiro, P. T. Matsudaira, J. R. Gnarra, T. Obinata and F. Matsumura, *J. Biol. Chem.*, 1997, **272**, 2527–2533.
30. D. Vignjevic, D. Yarar, M. D. Welch, J. Peloquin, T. Svitkina and G. G. Borisy, *J. Cell Biol.*, 2003, **160**, 951–962.
31. A. Duri, D. Sessoms, V. Trappe and L. Cipelletti, *Phys. Rev. Lett.*, 2009, **102**, 085702.

32. P. T. Tokumaru and P. E. Dimotakis, *Experiments in Fluids*, 1995, **19**, 1–15.

33. R. C. Arevalo, J. S. Urbach and D. L. Blair, *Biophys. J.*, 2010, **99**, L65–L67.

34. L. J. Kaufman, C. P. Brangwynne, K. E. Kasza, E. Filippidi, V. D. Gordon, T. S. Deisboeck and D. A. Weitz, *Biophys. J.*, 2005, **89**, 635–650.

35. O. Lieleg, *PhD thesis*, Technische Universität München, 2008.

36. C. Wurm, *PhD thesis*, Technische Universität München, 2011.

37. K. M. Schmoller, *PhD thesis*, Technische Universität München, 2012.

38. I. Szeverenyi, A. J. Cassidy, C. W. Chung, B. T. K. Lee, J. E. A. Common, S. C. Ogg, H. Chen, S. Y. Sim, W. L. P. Goh, K. W. Ng, J. A. Simpson, L. L. Chee, G. H. Eng, B. Li, D. P. Lunny, D. Chuon, A. Venkatesh, K. H. Khoo, W. H. I. McLean, Y. P. Lim and E. B. Lane, *Hum. Mutat.*, 2008, **29**, 351–360.

39. H. Herrmann, M. Hesse, M. Reichenzeller, U. Aebi and T. Magin, *Int Rev Cytol*, 2003, **223**, 83–175.

40. H. Herrmann and U. Aebi, *Curr. Opin. Cell Biol.*, 2000, **12**, 79–90.

41. E. Fuchs and K. Weber, *Annu. Rev. Biochem.*, 1994, **63**, 345–382.

42. E. Fuchs and D. W. Cleveland, *Science*, 1998, **279**, 514–519.

43. P. A. Coulombe and P. Wong, *Nat. Cell Biol.*, 2004, **6**, 699–706.

44. Y. Gruenbaum, A. Margalit, R. D. Goldman, D. K. Shumaker and K. L. Wilson, *Nat. Rev. Mol. Cell. Biol.*, 2005, **6**, 21–31.

45. R. Beck, J. Deek, J. B. Jones and C. R. Safinya, *Nature Materials*, 2009, **9**, 40–46.

46. Z. Xu, L. C. Cork, J. W. Griffin and D. W. Cleveland, *Cell*, 1993, **73**, 23–33.

47. H. Herrmann, S. V. Strelkov, P. Burkhard and U. Aebi, *J. Clin. Invest.*, 2009, **119**, 1772–1783.

48. C. H. Lee and P. A. Coulombe, *J. Cell Biol.*, 2009, **186**, 409–421.

49. P. A. Coulombe and M. B. Omary, *Curr. Opin. Cell Biol.*, 2002, **14**, 110–122.

50. I. Hofmann, C. Mertens, M. Brettel, V. Nimmrich, M. Schnölzer and H. Herrmann, *J. Cell Sci.*, 2000, **113 (Pt 13)**, 2471–2483.

51. A. Kölsch, R. Windoffer and R. E. Leube, *Cell Motil. Cytoskeleton*, 2009, **66**, 976–985.

52. A. Kölsch, R. Windoffer, T. Würflinger, T. Aach and R. E. Leube, *J. Cell Sci.*, 2010, **123**, 2266–2272.

53. R. Windoffer, M. Beil, T. M. Magin and R. E. Leube, *J. Cell Biol.*, 2011, **194**, 669–678.

54. K. Yoon, M. Yoon, R. Moir, S. Khuon, F. Flitney and R. Goldman, *J. Cell Biol.*, 2001, **153**, 503–516.

55. S. Woll, R. Windoffer and R. E. Leube, *J. Cell Biol.*, 2007, **177**, 795–807.

56. T. Busch, M. Armacki, T. Eiseler, G. Joodi, C. Temme, J. Jansen, G. von Wichert, M. B. Omary, J. Spatz and T. Seufferlein, *J. Cell Sci.*, 2012, **125**, 2148–2159.

57. M. Beil, A. Micoulet, G. von Wichert, S. Paschke, P. Walther, M. B. Omary, P. P. Van Veldhoven, U. Gern, E. Wolff-Hieber, J. Eggermann, J. Waltenberger, G. Adler, J. Spatz and T. Seufferlein, *Nat. Cell Biol.*, 2003, **5**, 803–811.

58. F. Gittes, B. Mickey, J. Nettleton and J. Howard, *J. Cell Biol.*, 1993, **120**, 923–934.

59. L. Kreplak, H. Bär, J. F. Leterrier, H. Herrmann and U. Aebi, *J. Mol. Biol.*, 2005, **354**, 569–577.

60. I. Hofmann and W. Franke, *Eur. J. Cell Biol.*, 1997, **72**, 122–132.

61. P. A. Coulombe, O. Bousquet, L. Ma, S. Yamada and D. Wirtz, *Trends in Cell Biology*, 2000, **10**, 420–428.

62. J. W. Mack, A. C. Steven and P. M. Steinert, *J. Mol. Biol.*, 1993, **232**, 50–66.

63. J. Deek, P. J. Chung, J. Kayser, A. R. Bausch and C. R. Safinya, *Nat. Commun.*, 2013, **4**, 2224.

64. M. Beil, S. Lueck, F. Fleischer, S. Portet, W. Arendt and V. Schmidt, *J Theor Biol*, 2009, **256**, 518–532.

65. J. Kayser, H. Grabmayr, M. Harasim, H. Herrmann and A. R. Bausch, *Soft Matter*, 2012, **8**, 8873–8879.

66. S. Yamada, *Mol. Biol. Cell*, 2002, **13**, 382–391.

67. J. C. Troncoso, J. L. March, M. Häner and U. Aebi, *J. Struct. Biol.*, 1990, **103**, 2–12.

68. K. Richter, M. Haslbeck and J. Buchner, *Mol. Cell*, 2010, **40**, 253–266.

69. M. Haslbeck, T. Franzmann, D. Weinfurtner and J. Buchner, *Nat. Struct. Mol. Biol.*, 2005, **12**, 842–846.

70. M. Ehrnsperger, H. Lilie, M. Gaestel and J. Buchner, *J. Biol. Chem.*, 1999, **274**, 14867–14874.

71. L. Nover, K. D. Scharf and D. Neumann, *Mol. Cell. Biol.*, 1989, **9**, 1298–1308.

72. K. Schulze-Osthoff, *J. Biol. Chem.*, 1996, **271**, 16510–16514.

73. N. Braun, M. Zacharias, J. Peschek, A. Kastenmüller, J. Zou, M. Hanzlik, M. Haslbeck, J. Rappsilber, J. Buchner and S. Weinkauf, *Proc. Natl. Acad. Sci.*, 2011, **108**, 20491–20496.

74. R. Van Montfort, C. Slingsby and E. Vierling, *Adv. Protein Chem.*, 2001, **59**, 105–156.

75. S. A. Houck, A. Landsbury, J. I. Clark and R. A. Quinlan, *PLoS ONE*, 2011, **6**, e25859.

76. T. Miron, *J. Cell Biol.*, 1991, **114**, 255–261.

77. l. D. Nicholl and R. A. QuinIan, *EMBO J.*, 1994, **13**, 945.

78. M. D. Perng, L. Cairns, P. van den IJssel, A. Prescott, A. M. Hutcheson and R. A. Quinlan, *J. Cell Sci.*, 1999, **112**, 2099–2112.

79. B. M. Doshi, L. E. Hightower and J. Lee, *Ann. N. Y. Acad. Sci.*, 2010, **1197**, 76–84.

80. P. Vicart, A. Caron, P. Guicheney, Z. Li, M.-C. Prévost, A. Faure, D. Chateau, F. Chapon, F. Tomé and J.-M. Dupret, *Nature genetics*, 1998, **20**, 92–95.

81. K. Djabali, B. de Néchaud, F. Landon and M. M. Portier, *J. Cell Sci.*, 1997, **110 (Pt 21)**, 2759–2769.

82. K. E. Kasza, A. C. Rowat, J. Liu, T. E. Angelini, C. P. Brangwynne, G. H. Koenderink and D. A. Weitz, *Curr. Opin. Cell Biol.*, 2007, **19**, 101–107.

83. W. M. Bement, G. I. Gallicano and D. G. Capco, *Microsc. Res. Tech.*, 1992, **22**, 23–48.

84. D. Kedrin, J. Rheenen, L. Hernandez, J. Condeelis and J. E. Segall, *J. Mammary Gland Biol. Neoplasia*, 2007, **12**, 143–152.

85. L. Ramms, G. Fabris, R. Windoffer, N. Schwarz, R. Springer, C. Zhou, J. Lazar, S. Stiefel, N. Hersch, U. Schnakenberg, T. M. Magin, R. E. Leube, R. Merkel and B. Hoffmann, *Proc. Natl. Acad. Sci.*, 2013.

86. K. Seltmann, A. W. Fritsch, J. A. Käs and T. M. Magin, *Proc. Natl. Acad. Sci.*, 2013.

87. M. Ehrnsperger, S. Gräber, M. Gaestel and J. Buchner, *EMBO J.*, 1997, **16**, 221–229.

88. T. T. Falzone, P. W. Oakes, J. Sees, D. R. Kovar and M. L. Gardel, *Biophys. J.*, 2013, **104**, 1709–1719.

89. A. Stürmer, *Bachelor Thesis, Technische Universität München*, 2012.

90. M. M. A. E. Claessens, C. Semmrich, L. Ramos and A. R. Bausch, *Proc. Natl. Acad. Sci.*, 2008, **105**, 8819–8822.

91. J. P. Gong, Y. Katsuyama, T. Kurokawa and Y. Osada, *Adv. Mater.*, 2003, **15**, 1155–1158.

92. J. P. Gong, *Soft Matter*, 2010, **6**, 2583.

93. L. Cipelletti, L. Ramos, S. Manley, E. Pitard, D. A. Weitz, E. E. Pashkovski and M. Johansson, *Faraday Disc.*, 2002, **123**, 237–251.

94. O. Lieleg, M. M. A. E. Claessens and A. R. Bausch, *Soft Matter*, 2010, **6**, 218–225.

95. P. Sollich, *Phys. Rev. E*, 1998, **58**, 738–759.

96. B. Fabry and J. J. Fredberg, *Respir Physiol Neurobiol*, 2003, **137**, 109–124.

97. P. Bursac, G. Lenormand, B. Fabry, M. Oliver, D. A. Weitz, V. Viasnoff, J. P. Butler and J. J. Fredberg, *Nature Materials*, 2005, **4**, 557–561.

98. L. Cipelletti, S. Manley, R. C. Ball and D. A. Weitz, *Phys. Rev. Lett.*, 2000, **84**, 2275–2278.

99. J. P. Bouchaud and E. Pitard, *The European Physical Journal E*, 2001, **6**, 231–236.
100. L. Cipelletti and L. Ramos, *J. Phys.: Condens. Matter*, 2005, **17**, R253–R285.
101. R. Bandyopadhyay, D. Liang and J. L. Harden, *Solid State Communications*, 2006, 589–598.
102. O. Lieleg, M. Claessens, C. Heussinger, E. Frey and A. Bausch, *Phys. Rev. Lett.*, 2007, **99**, 088102.
103. V. Normand, S. Muller, J.-C. Ravey and A. Parker, *Macromolecules*, 2000, **33**, 1063–1071.
104. M. Cloitre, R. Borrega and L. Leibler, *Phys. Rev. Lett.*, 2000, **85**, 4819–4822.
105. S. Romer, F. Scheffold and P. Schurtenberger, *Phys. Rev. Lett.*, 2000, **85**, 4980–4983.
106. V. Viasnoff and F. Lequeux, *Phys. Rev. Lett.*, 2002, 065701.
107. C. Derec, G. Ducouret, A. Ajdari and F. Lequeux, *Phys. Rev. E*, 2003, **67**, 061403.
108. L. Ramos and L. Cipelletti, *Phys. Rev. Lett.*, 2001, **87**, 245503.
109. L. Ramos and L. Cipelletti, *Phys. Rev. Lett.*, 2005, **94**, 158301.
110. O. Lieleg, M. Claessens, Y. Luan and A. Bausch, *Phys. Rev. Lett.*, 2008, **101**, 108101.
111. O. Lieleg, K. M. Schmoller, M. M. A. E. Claessens and A. R. Bausch, *Biophys. J.*, 2009, **96**, 4725–4732.
112. M. M. A. E. Claessens, M. Bathe, E. Frey and A. R. Bausch, *Nature Materials*, 2006, **5**, 748–753.
113. G. Bell, *Science*, 1978, **200**, 618–627.
114. E. Evans, *Faraday Disc.*, 1999, **111**, 1–16.
115. P. Fernández, L. Heymann, A. Ott, N. Aksel and P. A. Pullarkat, *New J. Phys.*, 2007, **9**, 419–419.
116. B. J. Berne and R. Pecora, *Dynamic Light Scattering: With Applications to Chemistry, Biology and Physics*, Wiley, 1976.

117. T. Stossel, *Science*, 1993, **260**, 1086–1094.
118. G. C. Ellis-Davies and J. H. Kaplan, *Proc. Natl. Acad. Sci.*, 1994, **91**, 187–191.
119. M. Irie, *J Am Chem Soc*, 1983, **105**, 2078–2079.
120. S. Woll, R. Windoffer and R. E. Leube, *J. Cell Biol.*, 2007, **177**, 795–807.
121. N. O. Ku, *J. Biol. Chem.*, 2002, **277**, 10775–10782.
122. G. M. Nagaraja, P. Kaur and A. Asea, *Curr. Mol. Med.*, 2012, **12**, 1142–1150.
123. C. G. Rolli, T. Seufferlein, R. Kemkemer and J. P. Spatz, *PLoS ONE*, 2010, **5**, e8726.
124. S. Sivaramakrishnan, J. V. DeGiulio, L. Lorand, R. D. Goldman and K. M. Ridge, *Proc. Natl. Acad. Sci.*, 2008, **105**, 889–894.
125. C. Semmrich, T. Storz, J. Glaser, R. Merkel, A. R. Bausch and K. Kroy, *Proc. Natl. Acad. Sci.*, 2007, **104**, 20199–20203.
126. M. L. Gardel, J. H. Shin, F. C. MacKintosh, L. Mahadevan, P. A. Matsudaira and D. A. Weitz, *Phys. Rev. Lett.*, 2004, **93**, 188102.
127. J.-Y. Sun, X. Zhao, W. R. K. Illeperuma, O. Chaudhuri, K. H. Oh, D. J. Mooney, J. J. Vlassak and Z. Suo, *Nature*, 2012, **489**, 133–136.
128. M. Abkarian, E. Loiseau and G. Massiera, *Soft Matter*, 2011, **7**, 4610–4614.

LIST OF FIGURES

Figure 1.1 Cartoon of the cytoskeleton. 2
Figure 2.1 Temperature control setup for real time measurements of network assembly. 9
Figure 2.2 The network morphology is quantified by the distribution of distances between structures 15
Figure 2.3 Mesh size analyzer interface 16
Figure 2.4 Fourier analysis of network images. 17
Figure 2.5 Displacement analysis of sheared networks. 19
Figure 3.1 Keratin intermediate filament assembly 22
Figure 3.2 TEM image of keratin filaments. 23
Figure 3.3 STED image of a MCF7 cell. 24
Figure 4.1 Keratin forms clustered structures at low protein concentrations. 28
Figure 4.2 Temporal hierarchy of keratin bundle formation. 29
Figure 4.3 At high protein concentrations keratin forms homogeneous networks with a heterogeneous substructure. 30
Figure 4.4 Structural evolution of a keratin network. 32
Figure 4.5 Network structure depends on the course of assembly. 33
Figure 4.6 Fast elongation results in less clustering. 34
Figure 5.1 Hsp27 causes an alteration of keratin network structure. 39
Figure 5.2 Hsp27 inhibits cluster association and network coarsening. 41
Figure 5.3 Hsp27 inhibits bundling. 42
Figure 5.4 Hsp27 interacts with soluble keratin tetramers. 43
Figure 5.5 The K8 tail is crucial for the Hsp27-effect. 44
Figure 5.6 Comparison of the Hsp27-effect for different K8 tail configurations. 45
Figure 5.7 Kinetic trapping and Hsp27 influence on keratin network formation. 46
Figure 6.1 A keratin scaffold influences the structure of actin/α-actinin bundle networks. 51
Figure 6.2 Relationship between mesh sizes of keratin and bundled actin networks. 52

Figure 6.3 A keratin scaffold influences the structure of actin actin/fascin bundle networks. 54
Figure 6.4 Design of a shearable diffusion chamber. 55
Figure 6.5 Analysis of networks under shear. 57
Figure 6.6 Displacement as a function of distance to the surface and strain. 58
Figure 6.7 Relation between applied and local shear. 59
Figure 7.1 The frequency dependent viscoelastic response of an actin/fascin bundle network changes with increasing sample age. 63
Figure 7.2 Confocal image of a fluorescently labelled actin/fascin bundle network. 65
Figure 7.3 Internal stress fields in actin/fascin bundle networks. 66
Figure 7.4 The temporal evolution of the microscopic displacements and that of the macroscopic network elasticity follow the same kinetics. 67
Figure 7.5 The age dependent changes in the viscoelastic network response can be modified by varying external or internal parameters. 69
Figure 7.6 Actin/fascin bundle networks exhibit age-dependent internal dynamics. 71
Figure 8.1 Macrorheometer with diffusion setup for *in situ* assembly. 78
Figure 8.2 Keratin network in a vesicle. 81

LIST OF PUBLICATIONS

1. **J. Kayser**, M. Haslbeck, L. Dempfle, M. Krause, C. Grashoff, J. Buchner, H. Herrmann, and A. R. Bausch:
   The Small Heat Shock Protein Hsp27 Affects Assembly Dynamics and Structure of Keratin Intermediate Filament Networks
   Biophysical Journal, **105** (2013), 1778-1785.

2. J. Deek, P. J. Chung, **J. Kayser**, A. R. Bausch, and C. R. Safinya:
   Neurofilament sidearms modulate parallel and crossed-filament orientations inducing nematic to isotropic and re-entrant birefringent hydrogels.
   Nature Communications, **9** (2013), 2224.

3. S. Lv, T. Bu, **J. Kayser**, A. R. Bausch, and H. Li:
   Towards constructing extracellular matrix-mimetic hydrogels: an elastic hydrogel constructed from tandem modular proteins containing tenascin FnIII domains.
   Acta Biomaterialia, **9** (2013), 6481-6491.

4. **J. Kayser**, H. Grabmayr, M. Harasim, H. Herrmann, and A. R. Bausch:
   Assembly kinetics determine the structure of keratin networks
   Soft Matter, **8** (2012), 8873-8879.

5. O. Lieleg[†], **J. Kayser**[†], G. Brambilla, L. Cipelletti, and A. R. Bausch:
   Slow dynamics and internal stress relaxation in bundled cytoskeletal networks
   Nature Materials, **10** (2011), 236-242.
   [†] These authors contributed equally to this work.

6. T. Naiser, **J. Kayser**, T. Mai, W. Michel, and A. Ott:
   Stability of a Surface-Bound Oligonucleotide Duplex Inferred from Molecular Dynamics: A Study of Single Nucleotide Defects Using DNA Microarrays.
   Physical Review Letters, **102** (2009), 218301.

DANKE...

Zum Abschluss möchte ich mich bei all denen bedanken, die mich während dieser Arbeit auf so wunderbare und konstruktive Weise begleitet und unterstützt haben:

- Andreas für die wirklich großartige Unterstützung, sein Vertrauen in das Projekt und die Freiheit es nach meinen Vorstellungen gestalten zu können.
- Christine für viele wunderbare Gespräche und gemeinsames Lachen.
- Volker für erleuchtende Diskussionen wissenschaftlicher und nichtwissenschaftlicher Art und das Finden von Tackern.
- Simone für ihre unerschöpfliche Geduld bei ignoranten Physiker-Fragen und ihre Lebensfreude.
- Kurt für seine ansteckende Begeisterung für die Wissenschaft im Allgemeinen und die Nichtgleichgewichtsdynamik sphärischer Objekte auf granulärem Untergrund im Speziellen.
- Schuppi für viele wertvolle Einblicke in das Abenteuer Papa-werden.
- Dr. Deek for crossing the big pond and bringing her never ending good mood with her.
- Sig. Rossetti per prendere la balla al balzo.
- Martina für intellektuelle und kulinarische Schaumschlägereien.
- Heinrich für Doughnuts im Dunkeln.
- Uli für vernetztes Wissen.
- Markus für viel Amente.
- Felix für brillante Ideen zum richtigen Zeitpunkt.
- Carina für frische Perspektiven.

- Fabi für den eingehenden Diskurs zur Rattenboot-Navigationsproblematik.
- Oli für einen gelungenen Start.
- Meinen Bachelor- und Werkstudenten, Axel, Lisa und Fritz für die produktive Zusammenarbeit.
- Allen, die direkt an den Projekten dieser Arbeit beteiligt waren, für die erfolgreiche Kooperation.
- Den TAs für die hervorragende Unterstützung im Laboralltag.
- Den Sekretärinnen für die geduldige Führung durch das Labyrinth der Universitätsbürokratie.
- Der gesamten E27/E22/etc.-Crew für eine unvergleichliche Arbeitsatmosphäre.
- Der Studienstiftung des deutschen Volkes und CompInt für die finanzielle und ideelle Unterstützung.
- Sylvia, Roland, Dani, Stefan, Dodo, Droma, Ronja und Ian für ein zweites Zuhause.
- Lucas für einen tollen Gefährten auf einer gemeinsamen Reise.
- Ulla und Alo für eine wunderbare Begleitung von Anfang an.
- Andi für das was war und das was daraus wird.